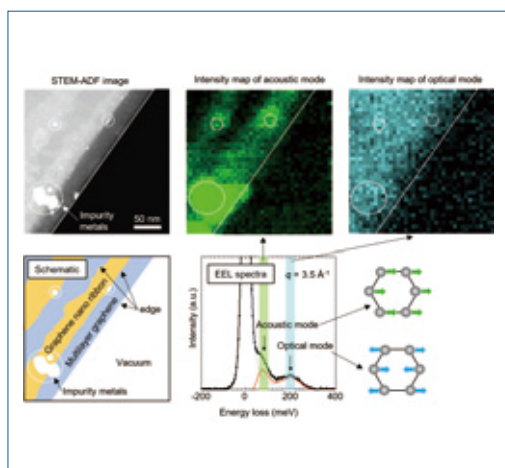


- Progress in Photonic Crystal Lasers and Their Application to LiDAR.....2  
Susumu Noda Department of Electronic Science and Engineering, Kyoto University
- And Yet It Moves: Molecular Rotors and Motors Studied by Solid-State NMR Spectroscopy.....9  
Martin Dračinský, Carina Santos Hurtado, Guillaume Bastien, Jiří Kaleta  
Institute of Organic Chemistry and Biochemistry, Czech Academy of Sciences
- Dioxins Analysis with New GC-MS/MS System and Software "TQ-DioK" .....15  
Imane Senoussaoui<sup>1</sup>, Masahiro Hashimoto<sup>1</sup>,  
Thomas Lehardy<sup>2</sup>, Anais Venisseau<sup>2</sup>, Philippe Marchand<sup>2</sup>  
<sup>1</sup>JEOL (EUROPE) SAS, France <sup>2</sup>LABoratoire d'Etude des Résidus et Contaminants dans les Aliments (LABERCA), Nantes, France
- Characterization of Localized Physical Properties Using High Resolution EELS .....21  
Ryosuke Senga, Kazu Suenaga National Institute of Advanced Industrial Science and Technology, Osaka University
- In-Resin CLEM of Epon-Embedded Cells Using Fluorescent Proteins.....25  
Isei Tanida, Junji Yamaguchi, Soichiro Kakuta, and Yasuo Uchiyama  
Juntendo University Graduate School of Medicine
- Degradation Analysis for Polymer Materials by Spin-Trapping.....31  
Wataru Sakai Faculty of Materials Science and Engineering, Kyoto Institute of Technology
- High-Speed Electron Beam Modulation System Using Electrostatic Deflection and Laser Delivery System to the Specimen in Transmission Electron Microscopy.....37  
Takeshi Kaneko<sup>1</sup>, Norihiro Okoshi<sup>1</sup>, Takeo Sasaki<sup>1</sup>, Kazuki Yagi<sup>1</sup>, Takeshi Sato<sup>1</sup>,  
Hiroki Hashiguchi<sup>1</sup>, Ichiro Ohnishi<sup>1</sup>, Yu Jimbo<sup>1</sup>, Hidetaka Sawada<sup>1</sup>, and Shinsuke Ogiwara<sup>1,2</sup>,  
Ruth Shewmon Bloom<sup>2</sup>, Bryan Reed<sup>2</sup>, Sang Tae Park<sup>2</sup>, Daniel Masiel<sup>2</sup>  
<sup>1</sup>JEOL Ltd. <sup>2</sup>IDES: Integrated Dynamic Electron Solutions, Inc. 5653 Stoneridge Dr. #117 Pleasanton, CA 94588
- The New Detection System of High-End FE-SEM JSM-IT800 Super Hybrid Lens (SHL).....42  
Tatsuro Nagoshi, Yuuki Yamaguchi EP Business Unit, JEOL Ltd.
- Preparation of TEM Specimens Having Specific Crystal Orientations Using FIB-SEM and EBSD ~ Applications to Allende meteorite ~ .....50  
Misumi Kadoi<sup>1</sup>, Masateru Shibata<sup>1</sup> and Ichiro Ohnishi<sup>2</sup> <sup>1</sup>EP Business Unit, JEOL Ltd. <sup>2</sup>EM Business Unit, JEOL Ltd.
- Chemical Bonding State Analysis of Boron and Phosphorus Compounds by Soft X-ray Emission Spectroscopy and Electronic Structure Calculations .....56  
Shogo Koshiya, Takanori Murano, Masaru Takakura and Hideyuki Takahashi SA Business Unit, JEOL Ltd.
- Chemical State Analysis of Fe in the Matrix of the Allende Meteorite Using an FEG EPMA and SXES.....61  
Takaomi D. Yokoyama SA Business Unit, JEOL Ltd.
- MultiAnalyzer – Unknown Compounds Analysis System  
New Gas Chromatograph Time-of-Flight Mass Spectrometer JMS-T2000GC "AccuTOF™ GC-Alpha" .....66  
Masaaki Ubukata MS Business Unit, JEOL Ltd.
- Introduction of JEOL Products .....73



## Cover micrograph

The figure captures the change in local lattice vibration at the graphene edge. Infrared absorption (bottom center) of a graphene nanoribbon grown at the top of a multilayer graphene (top left ADF image and bottom left schematic) acquired by high-energy-resolution EELS. The intensity distributions of the acoustic mode (top center) and optical mode (top right) show significant differences reflecting the structure of the material. The data were taken by "JEOL TripleC#2".

# Progress in Photonic Crystal Lasers and Their Application to LiDAR

Susumu Noda Department of Electronic Science and Engineering, Kyoto University

Recent progress on photonic crystal lasers and their application to light detection and ranging (LiDAR), which will support smart mobility of robots and automobiles, are discussed. Following a brief introduction to the progress on photonic crystal lasers thus far, it is shown that high-power, high-beam-quality (= high-brightness) photonic crystal lasers can be used to construct lens-free, high-resolution LiDAR systems. Further capability of electrical two-dimensional beam scanning by changing the sizes and positions of the photonic-crystal lattice points is also addressed.

## Introduction

LiDAR is undergoing active research and development worldwide as an indispensable optical sensing technology which will support smart mobility of robots, automobiles, and agricultural and construction machinery. A schematic of a typical LiDAR system is shown in Fig. 1. For the light source, which is the central part of this system, a compact, affordable semiconductor laser (particularly, a broad-area semiconductor laser whose emission area has been expanded to increase its output power) is mainly used (Fig. 2). However, this laser inevitably suffers from a deteriorated beam quality due to the excitation of multiple transverse modes over the broad area, and its beam divergence angle is wide and asymmetric. To use this laser as a LiDAR light source, high-precision integration of complicated external lens systems is required to reshape

**Fig. 1 Schematic of a typical LiDAR system (Time-of-Flight (ToF) type)**

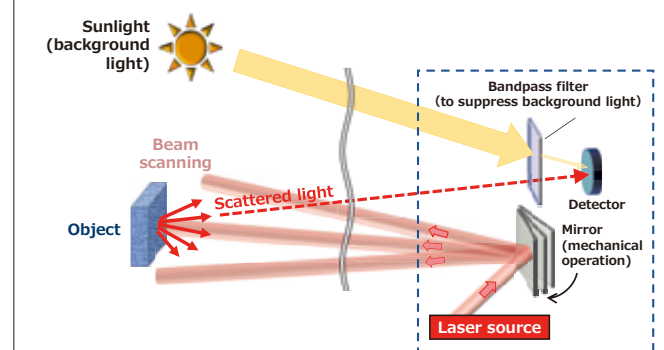
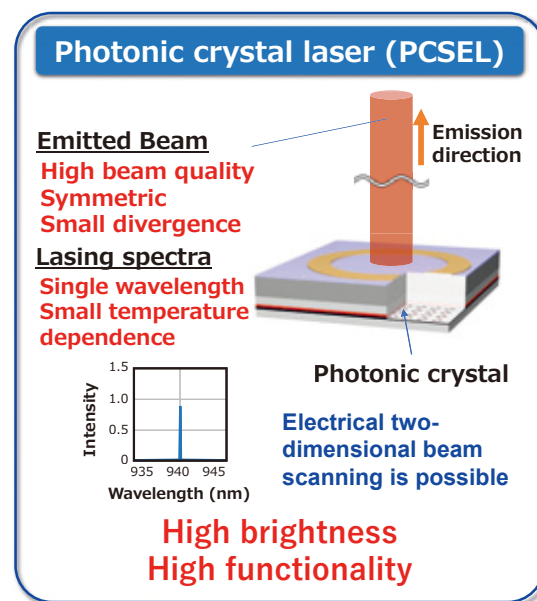
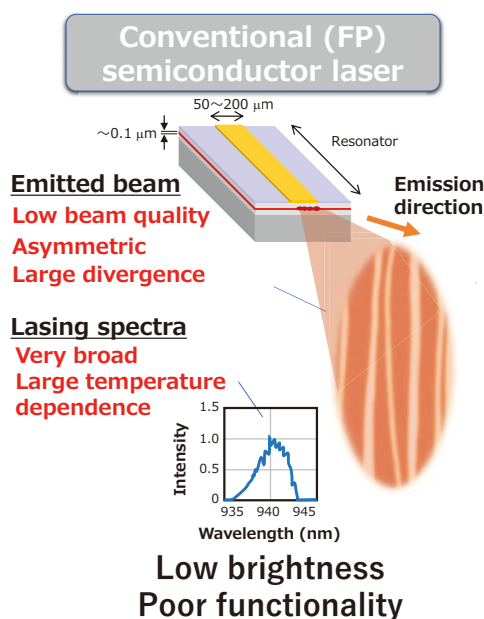


**Fig. 2 Comparison of a conventional semiconductor laser and a PCSE**



the beam, which compromises the compactness, affordability, and functionality of the system. Furthermore, for sensing applications, a bandpass filter is vital for suppressing the influence of background light, such as sunlight, that is incident on the detector. However, the lasing spectrum of a conventional semiconductor laser is both wide and sensitive to changes of temperature, so only wide bandpass filters can be used, which results in a low signal-to-noise (S/N) ratio.

The photonic crystal surface-emitting laser (PCSEL) [1-3], shown on the right-hand side of Fig. 2, is expected to solve these problems of the conventional semiconductor laser and thereby make LiDAR systems smaller, simpler, more affordable, and even more functional. As its resonant cavity, the PCSEL uses a built-in photonic crystal (which is an optical nanostructure consisting of air holes formed at intervals equal to wavelength of light in the semiconductor material), within which the oscillation of a single optical mode over even broad areas is possible in principle. Consequently, even if the lasing area is expanded to increase the optical output power, a beam can be emitted with an extremely narrow divergence angle and with no degradation of its beam quality. Also, lasing occurs at a single wavelength determined by the photonic crystal structure, and thus the lasing spectrum is narrow and its temperature dependence is small. By virtue of these features, high-precision integration of complicated lens systems is no longer required in the LiDAR light source, leading to the realization of a smaller, simpler, and more affordable system with fewer components. In addition, the circular, symmetric, narrow-divergence beam emitted by the PCSEL leads to an improvement of the spatial resolution of the system. The narrow linewidth and small temperature dependence of the lasing spectrum also permits the use of narrow bandpass filters with which background light can be greatly suppressed, thereby improving the S/N ratio. Furthermore, by customizing the photonic crystal structure – specifically, by simultaneously modulating the positions and sizes of its lattice points – it is even possible to scan the laser beam electrically and in two dimensions.

Below, after briefly reviewing the historical developments of

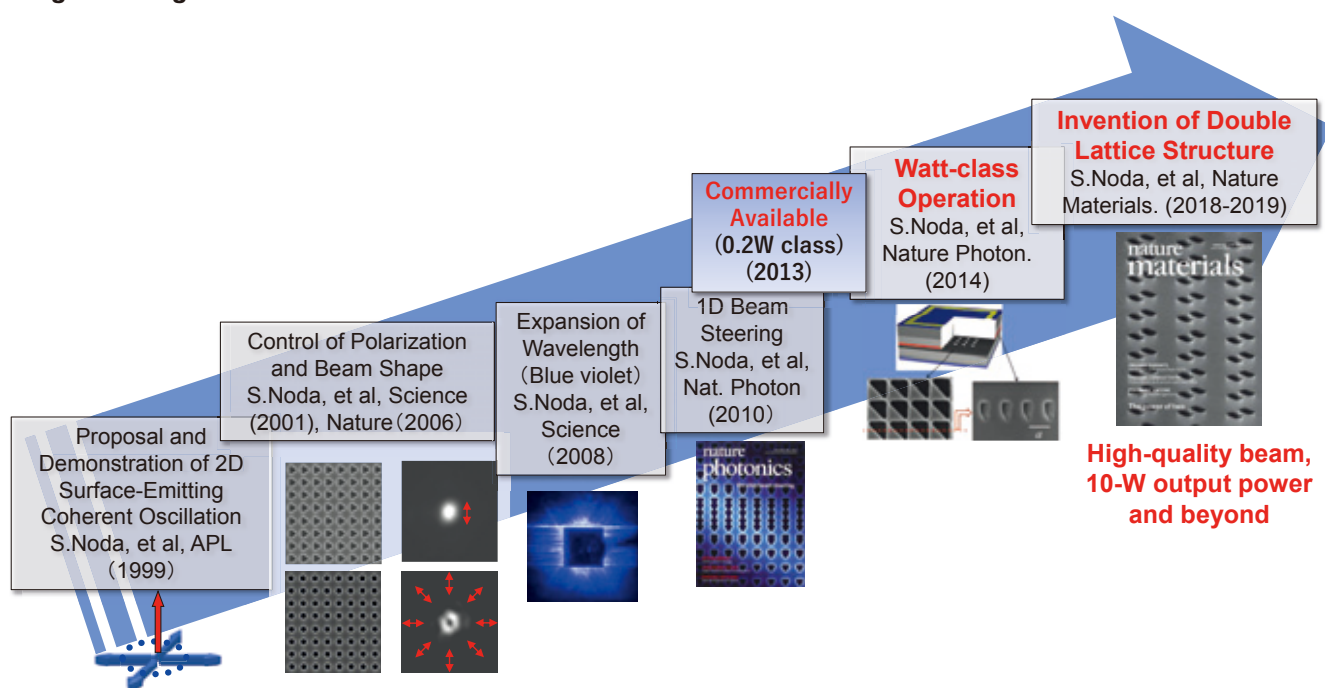
PCSELS, the development of a PCSEL-based LiDAR system is described. Then, the possibility of electrical two-dimensional beam scanning with PCSELS is addressed.

## Historical developments of PCSELS

**Figure 3** briefly summarizes the progress of PCSELS thus far. As shown in this figure, in 1999, the authors proposed and demonstrated the coherent oscillation of a single transverse mode over the broad area of a two-dimensional photonic crystal [1]. In this photonic crystal, various Bloch waves, propagating within the plane of the photonic crystal at a singularity known as the  $\Gamma$  point, are coupled into each other and form a two-dimensional standing wave; it is this standing wave by which the broad-area, two-dimensional oscillation mode is formed [2]. Also, at this  $\Gamma$  point, the oscillating light is emitted in a direction perpendicular to the surface of the photonic crystal.

Early PCSELS were realized using triangular-lattice photonic crystals [1-4], while PCSELS since then have been realized using square-lattice ones. The change from triangular-lattice photonic crystals to square-lattice ones was due to the better suitability of the latter for controlling the polarization state and beam shape, and also for increasing the output power. For example, as shown in the second panel from the left in Fig. 3, by simply changing the shape of the lattice points of a square lattice into triangles or circles, beautiful circular beams or donut-shaped vector beams can be emitted [5], and polarization control can be achieved, as well [6]. However, in order to realize stable broad-area oscillation in a square-lattice photonic crystal, it is necessary to form the photonic crystal using materials with a high refractive-index contrast (for example, air and a semiconductor material). This is because, in a square-lattice photonic crystal, direct two-dimensional coupling between the fundamental Bloch waves (of which there are four, each of which propagates in a direction orthogonal to the others) cannot occur; instead, two-dimensional coupling occurs only via intermediary Bloch waves of higher orders [2, 7], and, to induce these higher-order waves, a high

**Fig. 3 Progress of PCSELS**



contrast of refractive indices is necessary.

Following the above proposal and demonstration of PCSELS and the control of their polarization and beam shape, the operating wavelength of PCSELS was expanded to the blue-violet range [8], and an early demonstration of a new type of PCSEL that can electrically scan a beam (in one dimension) was conducted [9] (see the third and fourth panels from the left in Fig. 3). Initially, when fabricating these PCSELS, a photonic crystal consisting of air holes in a semiconductor background, which is required to achieve the high refractive-index contrast, was formed using a wafer-bonding method. However, it later became possible to form the same photonic crystal using a metal-organic chemical vapor deposition (MOCVD) regrowth technique, which dramatically improved the interfacial characteristics of the devices. As a result, in 2014, the operation of a PCSEL with watt-class output power was achieved [10], as shown in the second panel from the right in Fig. 3. For this PCSEL, a square-lattice photonic crystal consisting of unique air holes in the shape of isosceles right triangles was formed over an area of  $200 \mu\text{m}^2$ . At around the same time as this report, from 2013, PCSELS with output powers of around 0.2 W were made commercially available [11]. Then, in 2019, a PCSEL with ten-watt-class output power and a high beam quality was realized, based on a new concept involving the adoption of a double-lattice photonic crystal structure [7] (see the rightmost panel in Fig. 3). No other semiconductor laser can attain such high power while continuing to operate in a single mode with a high beam quality, and thus it can be said that the advantages of the PCSEL have clearly materialized.

## A new PCSEL-based LiDAR system

### A) Characteristics of a PCSEL developed for LiDAR applications

Figure 4 (left) is a photograph of a PCSEL (mounted on a 5.6-mm-diameter stem package) developed for installment in a LiDAR system. This PCSEL contains a double-lattice photonic crystal, which enables it to emit a high-power, high-quality beam from its broad 500- $\mu\text{m}$ -diameter oscillation area. As shown in its light-current characteristic under room-temperature (RT), pulsed operation in Fig. 4 (center), a peak output power of over 10 W

and a high slope efficiency of 0.8 W/A were achieved [3]. By connecting several of these PCSELS in series, it is possible to increase the slope efficiency even further (e.g., to 2.4 W/A and beyond, if three PCSELS are connected in series). Furthermore, as shown in Fig. 4 (right), even at this high peak power, a symmetric, circular beam with an extremely narrow divergence angle of around  $0.1^\circ$  was realized.

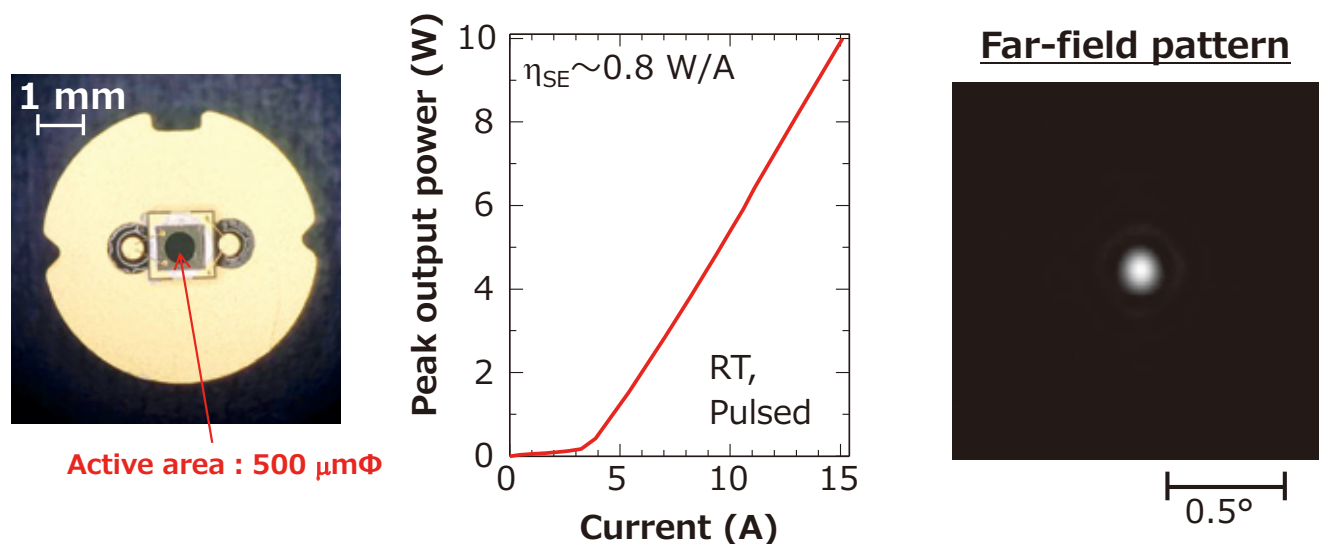
Figure 5 shows the far-field propagation of the PCSEL beam without the assistance of any lens [3]. The same propagation of a conventional broad-area semiconductor laser is also shown for comparison. It is seen that the beam of the conventional laser has a low quality, is asymmetric, and quickly diverges, especially in the vertical direction. It is for this reason that, when applying the conventional laser to LiDAR, a complicated system of lenses is required to reshape the beam. In contrast, the beam of the PCSEL propagates almost without diverging, even though no lens is used. Even at a far distance of 30 m, a symmetric, circular beam with a small, 5-cm-radius spot size is observed from the PCSEL. (Note that, at distances of under 1 m, the beam spot size is too small to be easily observed.)

### B) PCSEL installed in a LiDAR system

Figure 6 shows a comparison of a LiDAR system with a conventional semiconductor laser light source and a LiDAR system with the PCSEL light source described above [3]. Here, the laser beams are scanned in one dimension by mechanically rotating a mirror. As described above, for the conventional semiconductor laser, a complicated system of lenses must be integrated into the light source to reshape the beam, and, even after doing so, the beam spot size is large and distorted; consequently, the beam spots overlap during beam scanning, which lowers the spatial resolution of the system (see the bottom-left panel of Fig. 6). In contrast, for the PCSEL, the beam spot has an extremely narrow divergence angle and is circular, so it can be utilized without the assistance of any lens. Furthermore, as shown in the bottom-right panel of Fig. 6, the beam spots are clearly separated during beam scanning, which allows the system to have a high spatial resolution.

Next, Fig. 7 shows a demonstration of distance measurements performed in real time using the PCSEL-based LiDAR system, which can be miniaturized and simplified by virtue of its light

Fig. 4 940 nm-wavelength PCSEL developed for LiDAR applications



source being lens-free, and which can also have an improved spatial resolution. It can be seen how the fine details of the motion of Persons A and B, such as the movement of their hands, are captured by the system. These results indicate that a PCSEL-based LiDAR system has been successfully developed, and they also demonstrate the superiority of the PCSEL as a LiDAR light source.

### Electrical two-dimensional beam-scanning PCSEL

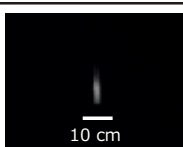
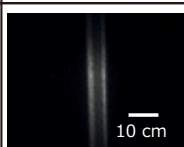
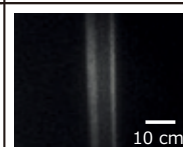
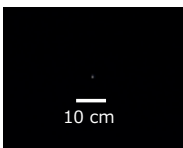
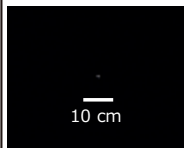
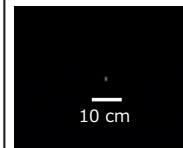
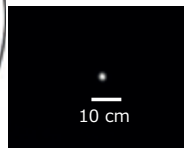
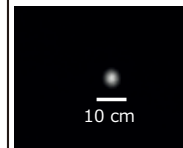
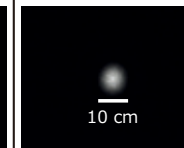
The aforementioned PCSEL emits a laser beam in a direction normal to the surface of the photonic crystal, and beam scanning with the constructed LiDAR system is done by mechanically rotating a mirror, as shown in Fig. 1. If this beam scanning can be performed not by the mechanical motion of a mirror, but rather by electrical means, then the reliability, stability, and compactness of the system is expected to remarkably improve.

Below is an introduction to a recently developed PCSEL that is capable of such electrical beam scanning in two dimensions [12].

As was shown in the fourth column from the left in Fig. 3, a PCSEL with an electrically scannable beam in one dimension has already been successfully proposed and demonstrated. Very recently, further innovations to the photonic crystal structure has led to the adoption of the “dually modulated photonic crystal” shown in Fig. 8, with which the emission of a high-power, high-quality beam in an arbitrary direction in two dimensions has been successfully demonstrated.

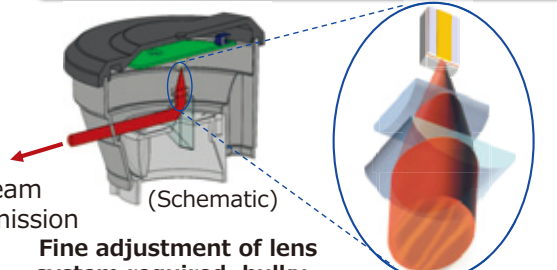
The positions and sizes of the lattice points of the photonic crystal shown in Fig. 8 are simultaneously modulated, and information pertaining to the beam emission direction are encoded at the time of this modulation. The PCSELS discussed up to the previous section operated at the  $\Gamma$  point, at which emission in the surface-normal direction is possible, but, with these dually modulated photonic crystals, a different singularity known as the M point is used in order to inhibit the emission

**Fig. 5 Comparison of far-field beam propagation of a conventional semiconductor laser and a PCSEL**

	15 cm	50 cm	1 m	10 m	20 m	30 m
Conventional broad-area laser				N/A	N/A	N/A
PCSEL (500 $\mu\text{m}\Phi$ )						

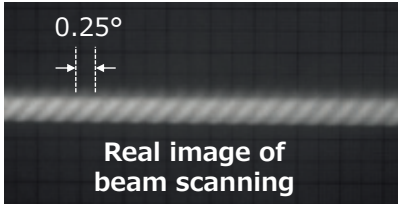
**Fig. 6 Comparison of conventional semiconductor laser and PCSEL light sources for LiDAR**

**LiDAR with a conventional semiconductor laser light source**



Beam emission (Schematic)

Fine adjustment of lens system required, bulky

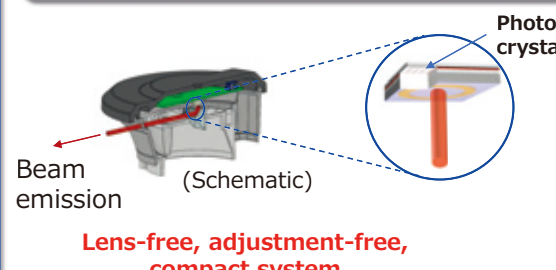


0.25°

Real image of beam scanning

Large beam divergence, low resolution

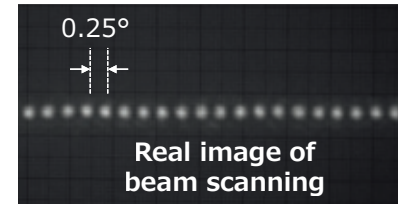
**LiDAR with a PCSEL light source**



Beam emission (Schematic)

Photonic crystal

Lens-free, adjustment-free, compact system



0.25°

Real image of beam scanning

Small beam divergence, high resolution

of light prior to the modulations. Then, dual modulation is introduced in order to have a beam be emitted in solely the direction of one's choosing.

**Figure 9** shows a schematic diagram of an on-chip array of dually modulated PCSELS based on the above concept for beam emission in multiple directions in two dimensions, as well as a microscope image of the bottom of a fabricated chip. Each PCSEL has a footprint area of  $150 \mu\text{m}^2$  (and a circular current injection area of  $100\text{-}\mu\text{m}$ -diameter), and the PCSELS are

arrayed in a  $10 \times 10$  matrix. All electrodes are integrated onto the back of the chip so that the laser beams can be emitted from the front of the chip without obstruction, and the PCSELS are electrically isolated from each other so that only the PCSEL(s) at the intersections of p- and n-line electrodes across which a voltage is applied are driven. Into each PCSEL is encoded its own unique beam emission direction. Also, from each PCSEL, two beams are simultaneously emitted at oblique angles which are mutual reflections of each other about the surface normal.

**Fig. 7 Demonstration of LiDAR with a PCSEL light source**

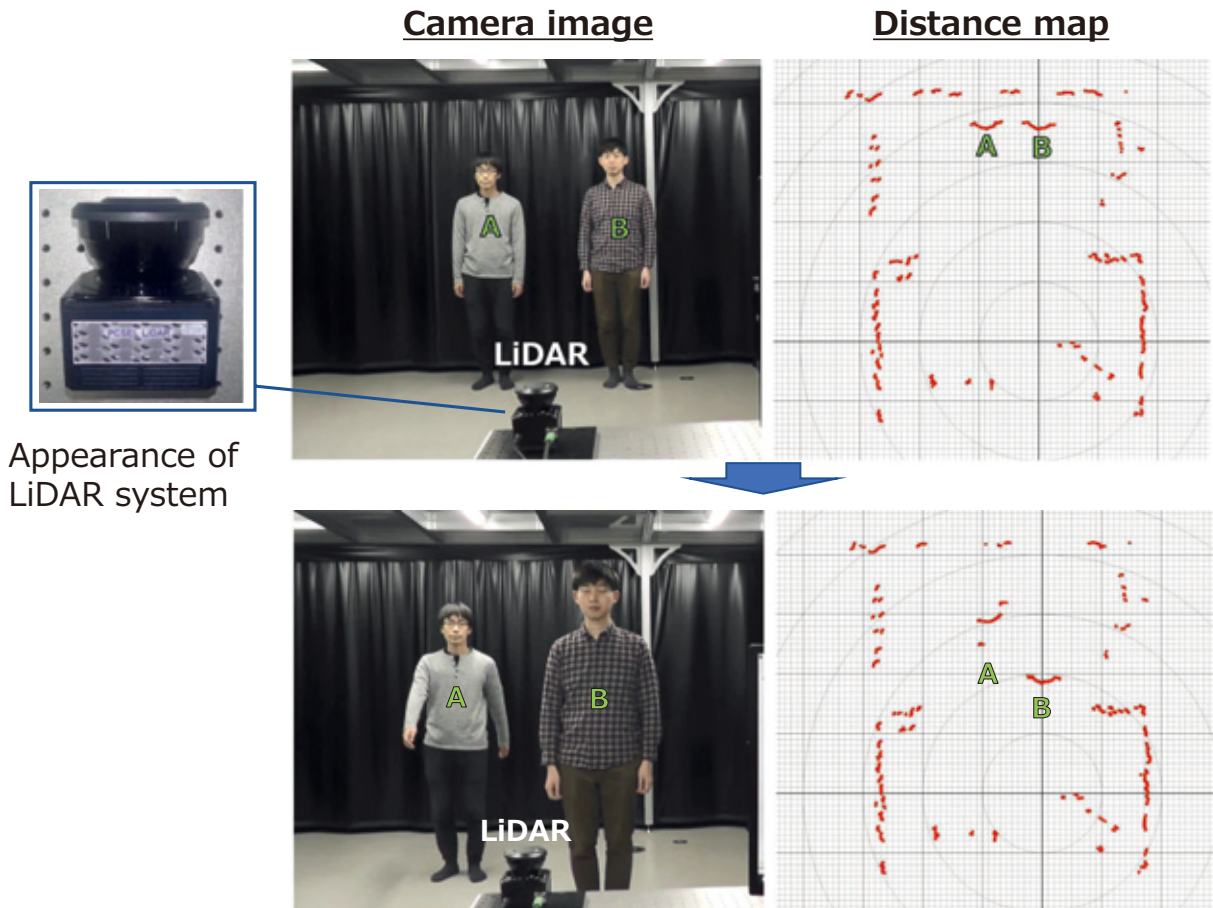
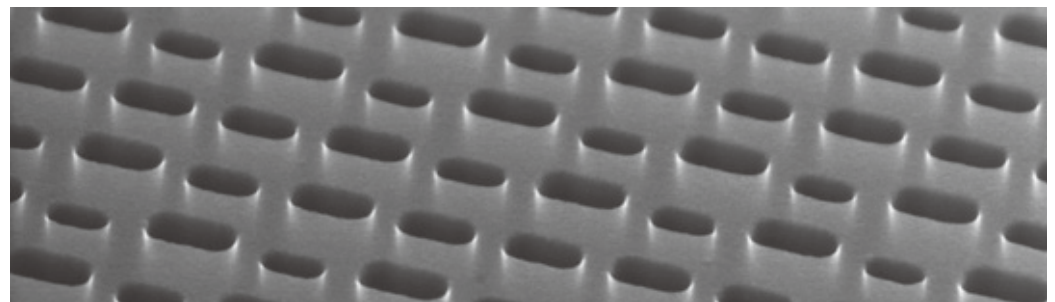


**Fig. 8 Scanning-electron-microscope image of a dually modulated photonic crystal (birds'-eye view).**



Scanning electron microscope image (taken at an oblique angle from the surface normal)

Lattice-point positions and sizes are simultaneously modulated. In these modulations are encoded information about the beam emission direction. Also, the lattice constant (= spacing between the lattice points) is set to  $1/\sqrt{2}$  times the wavelength in the material ( $\approx 195 \text{ nm}$ ). An electron beam lithography system used is a JEOL JBX-9400FS.

Using the arrayed chip described above, it is possible to drive 100 PCSELS in any order and at any speed. **Figure 10** shows snapshots of beam scanning. The top row of snapshots in this figure show beam scanning when the n-line electrodes are driven in sequence from n-1 to n-10 while the p-line electrode is fixed to p-5. For this sequence of PCSELS, a fixed polar emission angle  $\theta$  (from the surface normal) of  $20^\circ$  has been encoded, while azimuthal emission angles  $\phi$  (from the positive x axis) have been encoded to vary from  $0^\circ/180^\circ$  to  $45^\circ/225^\circ$ ; these emission angles are precisely those observed in the snapshots. Next, the middle row of snapshots shows beam scanning when the same sequence of n-line electrodes are driven, but the p-line electrode is fixed to p-6. In this case, it is the azimuthal angles  $\phi$  that have been designed to remain fixed to  $90^\circ/270^\circ$ , while the polar angle  $\theta$  has been designed to vary from  $0^\circ$  to  $45^\circ$ ; again, these emission angles are precisely those observed in the snapshots. Finally, the bottom row of snapshots shows beam scanning when the electrodes in the top and middle rows are driven at the same time to scan four beams simultaneously. These snapshots are just one example of beam scanning; in general, various beams can be scanned in any order at any timing. Furthermore, although details are omitted due to space restrictions, the number of resolvable points is not limited to 100, and can in fact be increased to over 90,000 without considerably increasing the chip area. It is also possible to

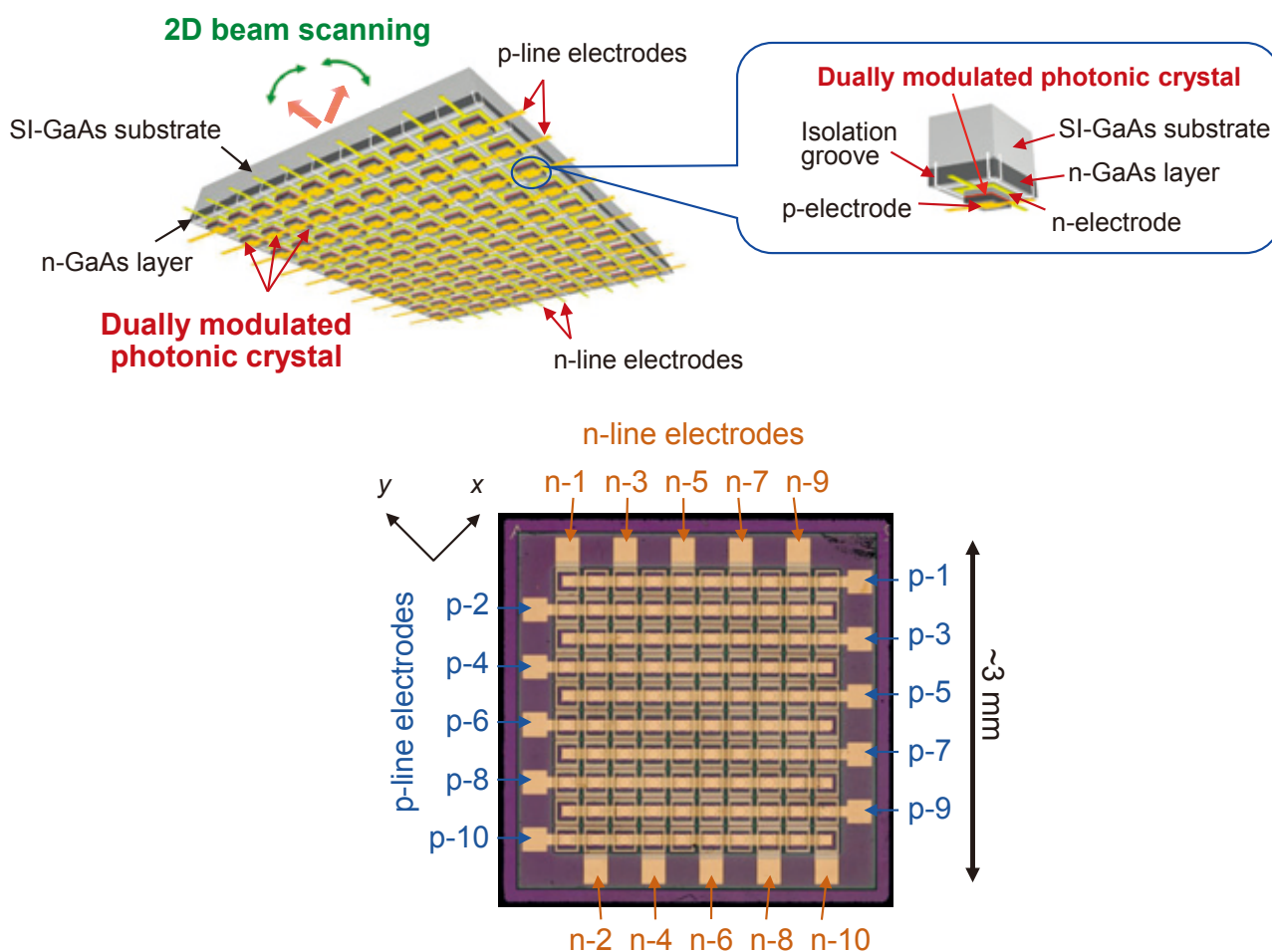
construct a new type of LiDAR system that leverages this beam-scanning technology. For more details, the reader is referred to Reference 12.

## Conclusions

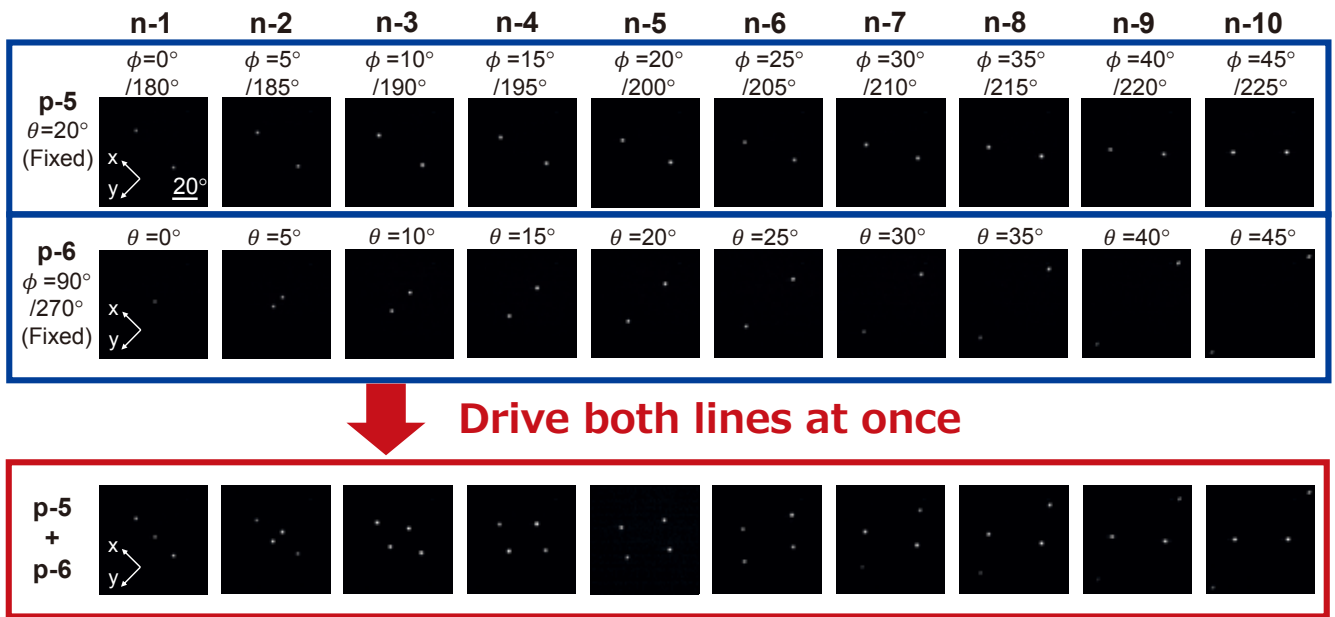
The recent developments of PCSELS and their application to LiDAR, which will support smart mobility of robots and automobiles, have been discussed. First, following a brief introduction to the progress of PCSEL development thus far, the possibility of leveraging the high output power and high beam quality (= high brightness) of the PCSEL in the construction of a lens-free, high-resolution LiDAR system has been shown. Next, the possibility of electrically scanning a beam in two dimensions by changing the lattice-point positions and sizes of a photonic crystal has been addressed. Also, while the PCSELS introduced here have a lasing wavelength of around 940 nm, expansion of this wavelength into the telecommunications wavelength bands ( $1.3 \mu\text{m}$  to  $1.5 \mu\text{m}$ ), where improved eye safety is expected, is under development.

In addition to sensing, PCSELS can be applied to material processing (including high-precision machining and the machining of metals) and biomedical fields, where their compactness, affordability, low power consumption, and high functionality will lead to their supplanting of bulky high-

**Fig. 9 On-chip array of dually modulated PCSELS for beam emission in various directions in two dimensions.**



(Top) Schematic of the entire device. (Bottom) Microscope image of the bottom of the chip.

**Fig. 10 Example of multi-beam scanning.**


The lasing wavelength is 940 nm.

brightness lasers (e.g., gas lasers and fiber lasers) currently in use. With these advantages, PCSELS can be said to be a key to unlock the door to a super smart society (Society 5.0).

## Acknowledgements

This work constitutes a portion of the research performed by Noda's Quantum Optoelectronics Laboratory in conjunction with the Nano-processing Lab at Kyoto University. The authors are deeply grateful to the faculty members, researchers, and students of both laboratories. Some of the results of this work have been obtained through collaborative research with ROHM Semiconductor and Hokuyo Automatic Co., Ltd, to whom the authors are also deeply grateful. This work was carried out under the project of Council for Science, Technology, and Innovation (CSTI), Cross-ministerial Strategic Innovation Promotion Program (SIP), "Photonics and Quantum Technology for Society 5.0" (Funding agency: QST), and under the CREST program "Next-generation Photonics" commissioned by the Japan Science and Technology Agency (JST).

## References

- [ 1 ] M. Imada, S. Noda, A. Chutinan, T. Tokuda, M. Murata, and G. Sasaki: "Coherent two-dimensional lasing action in surface-emitting laser with triangular-lattice photonic crystal structure," *Appl. Phys. Lett.*, vol. **75**, pp.316-318 (1999).
- [ 2 ] S. Noda, K. Kitamura, T. Okino, D. Yasuda, and Y. Tanaka: "Photonic-Crystal Surface-Emitting Lasers: Review and Introduction of Modulated-Photonic Crystals", *IEEE J. Sel. Top. Quantum Electron.*, vol. **23**, pp. 4900107 (2017).
- [ 3 ] M. Yoshida, M. DeZoysa, K. Ishizaki, W. Kunishi, T. Inoue, K. Izumi, R. Hatsuda and S. Noda, "Photonic-crystal lasers with high-quality narrow-divergence symmetric beams and their application to LiDAR", *J. Phys. Photonics*, (2021) (in press). (<https://iopscience.iop.org/article/10.1088/2515-7647/abea06>).
- [ 4 ] M. Imada, A. Chutinan, S. Noda, and M. Mochizuki, "Multidirectionally distributed feedback photonic crystal lasers", *Phys. Rev. B*, Vol. **65**, No.19, pp.195306 (2002).
- [ 5 ] E. Miyai, K. Sakai, T. Okano, W. Kunishi, D. Ohnishi, and S. Noda, "Lasers producing tailored beams", *Nature*, vol. **441**, no.7096, pp.946-946 (2006).
- [ 6 ] S. Noda, M. Yokoyama, M. Imada, A. Chutinan, M. Mochizuki, "Polarization Mode Control of Two-Dimensional Photonic Crystal Laser by Unit Cell Structure Design," *Science*, vol. **293**, pp. 1123-1125 (2001).
- [ 7 ] M. Yoshida, M. DeZoysa, K. Ishizaki, Y. Tanaka, M. Kawasaki, R. Hatsuda, B. Song, J. Gellela and S. Noda, "Double-lattice photonic-crystal resonators enabling high-brightness semiconductor lasers with symmetric narrow-divergence beams". *Nat. Mater.*, vol. **18**, pp.121-128 (2019).
- [ 8 ] H. Matsubara, S. Yoshimoto, H. Saito, Y. Jianglin, Y. Tanaka, and S. Noda, "GaN photonic-crystal surface-emitting laser at blue-violet wavelengths", *Science*, vol. **319**, no.5862, pp.445-447 (2008).
- [ 9 ] Y. Kurosaka, S. Iwahashi, Y. Liang, K. Sakai, E. Miyai, W. Kunishi, D. Ohnishi, and S. Noda, "On-chip beam-steering photonic-crystal lasers", *Nat. Photonics*, vol. **4**, no.7, pp. 447-450 (2010).
- [ 10 ] K. Hirose, Y. Liang, Y. Kurosaka, A. Watanabe, T. Sugiyama, and S. Noda, "Watt-class high-power, high-beam-quality photonic-crystal lasers", *Nat. Photonics*, vol. **8**, pp.406-411 (2014).
- [ 11 ] [https://www.kyoto-u.ac.jp/static/ja/news\\_data/h/h1/news6/2013/130926\\_1.htm](https://www.kyoto-u.ac.jp/static/ja/news_data/h/h1/news6/2013/130926_1.htm)
- [ 12 ] R. Sakata, K. Ishizaki, M. DeZoysa, S. Fukuhara, T. Inoue, Y. Tanaka, K. Iwata, R. Hatsuda, M. Yoshida, J. Gellela and S. Noda, "Dually modulated photonic crystals enabling high-power high-beam-quality two-dimensional beam scanning lasers", *Nat. Commun.*, vol. **11**, Article number: 3487 (2020). DOI: s41467-020-17092-w.

# And Yet It Moves: Molecular Rotors and Motors Studied by Solid-State NMR Spectroscopy

Martin Dračinský, Carina Santos Hurtado, Guillaume Bastien, Jiří Kaleta

Institute of Organic Chemistry and Biochemistry, Czech Academy of Sciences

Artificial molecular machines promise applications in many fields, including physics, information technologies, chemistry as well as medicine. The deposition of functional molecules in 2D or 3D assemblies in order to control their collective behavior and the structural characterization of these assemblies are important tasks. This paper summarizes our recent solid-state NMR (SS-NMR) studies of functional molecules deposited in a rigid matrix or on a surface (spectrometer: JEOL JNM-ECZ600R). It is demonstrated that SS-NMR experiments provide unequivocal evidence of the formation of these assemblies and can also be used for the observation of such a molecular function as the photoisomerization of a molecular switch.

## Introduction

Molecular machines play many important roles in nature. These fascinating molecules or supramolecular complexes are responsible, for example, for muscle contraction, for moving cargo inside cells, for the motion of cilia and flagella, and for energy production [1].

Like in many other fields, researchers have been inspired by nature and designed and synthesized artificial molecular machines and nanodevices [2-6]. Their structures include biaryls [7], metal complexes [8], rotaxanes [9], catenanes [10], and light- [11] or chemically-driven [12-14] molecular motors. Artificial molecular nanodevices promise applications as transporters [15-17], autonomous molecular machines [18, 19], synthesizers [20], materials for information storage [21], and responsive materials [22-24]. The importance of the field has also been recognized by the Nobel Committee, which awarded Jean-Pierre Sauvage, Sir J. Fraser Stoddart and Bernard L. Feringa for “the design and synthesis of molecular machines” in 2016.

An important task for the development of functional materials based on molecular machines is a precise control of their positioning in two- or three-dimensional arrays in order to synchronize and amplify their function. The approaches toward this goal include surface mounting [25-29], the use of metallo-organic frameworks [30, 31] or other porous materials [32], gels [33], polymers [34] and liquid crystals [35-37].

The structural characterization of the 2D and 3D assemblies of functional molecules is a crucial task for the success of the control of their collective behavior. Single-crystal X-ray diffraction (XRD) has been called the “gold standard” for solid-state structure determination [38], but there are limitations to this technique. A well-known limitation of XRD is that it

typically requires a highly-ordered crystalline sample and is thus inherently limited in the structural characterization of disordered or amorphous samples. Unfortunately, supramolecular assemblies of functional molecules are often heavily disordered. The lack of periodicity in disordered materials leads to a dramatic loss of information from diffraction experiments.

An alternative experimental technique for the atomic-level characterization of solids is solid-state NMR spectroscopy (SS-NMR). For example,  $^{13}\text{C}$  SS-NMR is commonly used as a structural probe of polymorphs in crystalline solids [39, 40]. In contrast to X-ray diffraction, SS-NMR does not require a long-range order in the materials studied and is, therefore, suitable for the characterization of disordered and amorphous samples [41-43].

In this paper, we summarize our recent progress in the SS-NMR studies of the supramolecular complexes of molecular rotors and motors. We have investigated the formation of the supramolecular assemblies and the function of the molecular devices in the solid assemblies. As the hosts for these supramolecular complexes, we have used hexagonal tris(*o*-phenylenedioxy)cyclotriphosphazene (TPP) or cucurbit[7]uril (CB[7]). The host-guest complexes were prepared mechanochemically by ball milling. The layered structure of hexagonal TPP contains an array of parallel hollow channels that can accommodate suitable guest molecules. Similarly, suitable guests can be inserted into the CB[7] cavity.

The results will be discussed in four subchapters, dealing with: 1) 3D assemblies of pyridazine rotors in TPP, 2) surface inclusions of molecular motors in TPP, 3) surface inclusions of an azo-switch in TPP, and 4) the mechanochemical preparation of CB[7] inclusion complexes. The structures of the compounds discussed are shown in **Figure 1**.

## Results and Discussion

### 1) 3D Assemblies of Pyridazine Rotors in TPP

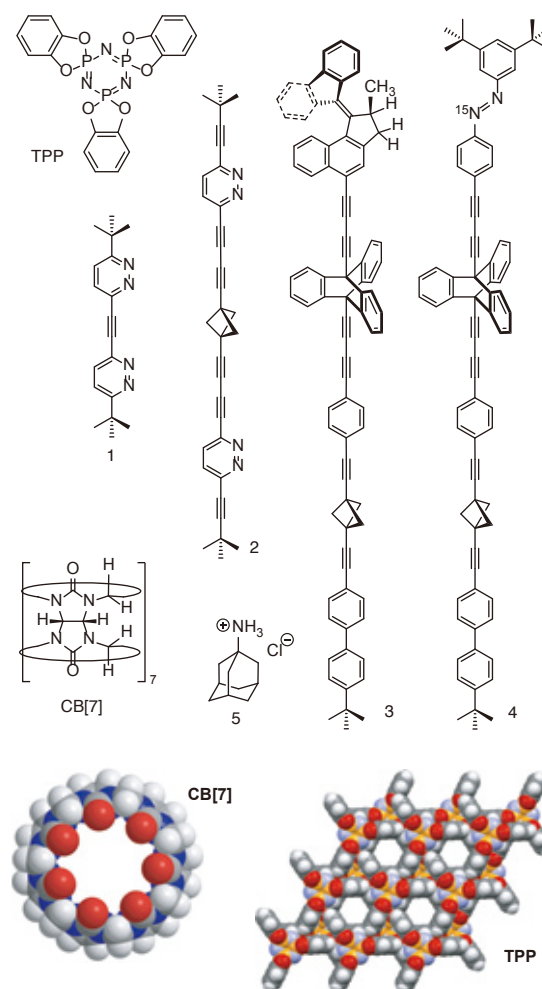
Pyridazine derivatives, such as compounds **1** and **2**, have a large dipole moment. We prepared these compounds with the aim of controlling their rotary motion (rotation along the long axis of the molecule) by a fluctuating electric field. We synthesized several other pyridazine derivatives similar to compounds **1** and **2**; these derivatives differ in the length of the linker that connects the pyridazine fragments with each other and with the terminal *tert*-butyl group. These variable-length linkers were used to fine-tune the distance between individual pyridazine moieties in the TPP channels and thus enabled a thorough investigation of the collective behavior of these rotors. All the studied molecular rotors had a rod-like shape, which fits well in the TPP channels [32].

In order to confirm the formation of the host-guest complexes prepared by ball-milling, we employed SS-NMR. To have a reliable indicator of the host-guest complex formation of the molecular rotors inserted into the TPP channels, we prepared a fully deuterated TPP (TPP- $d_{12}$ ) host. Cross-polarization (CP) SS-NMR experiments are based on a polarization transfer from hydrogen ( $^1\text{H}$ ) nuclei to the nuclei of interest ( $^{13}\text{C}$  or  $^{31}\text{P}$  in our case). Consequently, only the atoms that are close in space to hydrogen atoms are observable by this technique. On the other hand, experiments with direct excitation lead to the observation of all nuclei of a given isotope. For this reason, fully deuterated TPP has no signal in the  $^{13}\text{C}$  CP experiment, while three signals corresponding to the three non-equivalent carbon atoms in the hexagonal TPP polymorph are clearly observable in the  $^{13}\text{C}$  experiment with direct excitation. These three signals are also well visible in the  $^{13}\text{C}$  CP magic-angle-spinning (MAS) spectrum of the inclusion complexes of the studied pyridazines in deuterated TPP (**Figure 2**). The observation of the TPP carbon signals thus confirms that the fully protiated rotor molecules are immersed in the TPP- $d_{12}$  matrix. The same observation was also done in  $^{31}\text{P}$  SS-NMR spectra: no signal appeared in the CP-MAS spectrum of deuterated TPP, whereas a singlet at 33.0 ppm was observed in the phosphorus spectra with direct excitation and in the CP-MAS spectrum of the inclusion complex [32].

The immersion of molecular rotors into the TPP matrix also leads to significant chemical-shift changes. The ring current induced in the aromatic rings of TPP causes an upfield shift (to lower chemical shifts) of the signals of atoms in the TPP cavities (**Figure 2**).

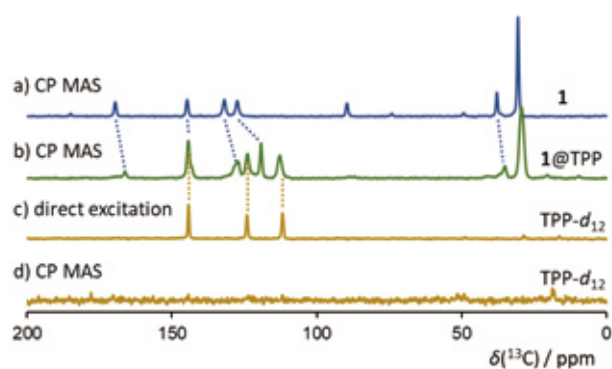
We have also studied the cross-polarization dynamics in the pure crystalline rotors and in the inclusion complexes. We have observed that the dependence of the intensity of carbon signals on the contact time (the length of CP) correlates with the distance to the nearest hydrogen atom. The signals of triple-bond carbon atoms, which are separated from the nearest hydrogen atoms by three or more bonds, grow slowly with increasing contact time. This is the result of inefficient CP given by longer C-H distances. In the pure crystalline rotors, the intermolecular distances of the triple-bond carbons to the hydrogen atoms of a neighboring molecule are shorter than or comparable with intramolecular C-H distances. The most remarkable difference in the  $^{13}\text{C}$  CP-MAS spectra of the host-guest complexes (apart from the presence of the TPP signals) is the very low intensity of the signals of the triple bonds; furthermore, this intensity increases only very slowly with increasing contact time. This observation may be attributed to insufficient intramolecular CP from the closest hydrogen nuclei

**Fig. 1**



The structures of the compounds studied and a view of the cavity/channels in CB[7] and TPP, respectively.

**Fig. 2**



The  $^{13}\text{C}$  CP-MAS spectra of a) crystalline compound **1** and of b) the inclusion complex of compound **1** in TPP- $d_{12}$ , the  $^{13}\text{C}$  spectra of TPP- $d_{12}$  measured with c) the direct excitation of carbon nuclei and with d) CP.

and the absence of intermolecular interactions with hydrogen atoms. The attenuated signals of the triple bonds may thus serve as another evidence of the formation of the inclusion complex. The triple-bond carbon signals can be observed in the  $^{13}\text{C}$  NMR spectra of the inclusion complexes acquired with direct carbon excitation without CP.

SS-NMR experiments can also be used to determine the dynamics of the guest molecules in the TPP matrix. MAS at high frequencies leaves only the isotropic line in the spectrum accompanied by a few low-intensity spinning sidebands (SSBs). Since any molecular mobility in the studied solid material leads to a further suppression of the SSBs, the number and intensity of SSBs may be used to diagnose internal motion in solid materials. In the  $^{13}\text{C}$  NMR spectrum of compound **2** acquired with 13-kHz MAS (**Figure 3**), the dominant lines correspond to the isotropic chemical shifts and the few observed SSBs belong mostly to the signals of triple bonds, which have very large chemical-shift anisotropy. However, when the same spectrum is acquired with 4.3-kHz MAS, there are many SSBs belonging to all isotropic signals. Many SSBs belong to the signals of the pyridazine carbon atoms, which indicates that these aromatic rings do not undergo  $\pi$  jumps or any kind of free rotation.

The spectrum of the inclusion complex of compound **2** in TPP (**2@TPP**) acquired with 13-kHz MAS shows only very few SSBs, which belong to the signals of TPP. In the spectrum of **2@TPP** acquired with the slower spinning of 4.3 kHz, there are many SSBs, but most of them belong to the signals of TPP. The SSBs belonging to the signals of compound **2** have very low intensity or are completely missing in the spectrum. This observation can be understood as a confirmation of the formation of the inclusion complex; the TPP matrix is rigid and provides signals with many SSBs in slow MAS spectra. Nevertheless, the guest molecule is relatively mobile with fast re-orientation of all its parts, which leads to a suppression of chemical-shift anisotropy and hence to the reduction of the number of SSBs in the spectrum. The suppression of SSBs indicates that the speed of the molecular re-orientation is in the order of the chemical-shift anisotropy (expressed in Hz) or faster, thus setting the lower limit of pyridazine rotation to ca 10 kHz [44, 45].

## 2) The Surface Inclusion of Unidirectional Molecular Motor **3** on TPP

In order to prepare a 2D array of molecular motors on the TPP surface, we prepared compound **3**, which contains the molecular motor designed by Feringa. The “passive” part of the molecule comprises a long shaft that fits into TPP channels and a triptycene stopper, which prevents the immersion of the whole molecule into the channel. The stopper ensures that the molecular motors are deposited on the TPP surface. Two NMR probes with distinct chemical shifts, namely the *tert*-butyl group and the bicyclo[1.1.1]pentyl cage, were intentionally installed into the shaft.

Like in the case of pyridazine rotors, we worked with a fully deuterated TPP matrix. The observation of TPP carbon signals in CP-MAS experiments then confirms that compound **3** is immersed in the TPP matrix (**Figure 4**). The same observation was also made in  $^{31}\text{P}$  SS-NMR spectra: there was no signal in the CP-MAS spectrum of deuterated TPP, whereas a singlet at 33.0 ppm appeared in the phosphorus spectra with direct excitation and in the CP-MAS spectrum of the inclusion complex [29].

A close inspection of the spectra reveals that the signals of the long shaft immersed in the matrix **3** have moved to higher chemical shifts (downfield), whereas the signals of the triptycene stopper and of the molecular motor have moved in the opposite

direction (upfield, **Figure 5**). This observation confirms the inclusion on the TPP surface. The ring-current effects of the aromatic rings of TPP cause an upfield shift of the signals of atoms in the TPP cavities (the shaft), whereas the stopper and the motor deposited on the TPP surface are less shielded than in crystalline **3**.

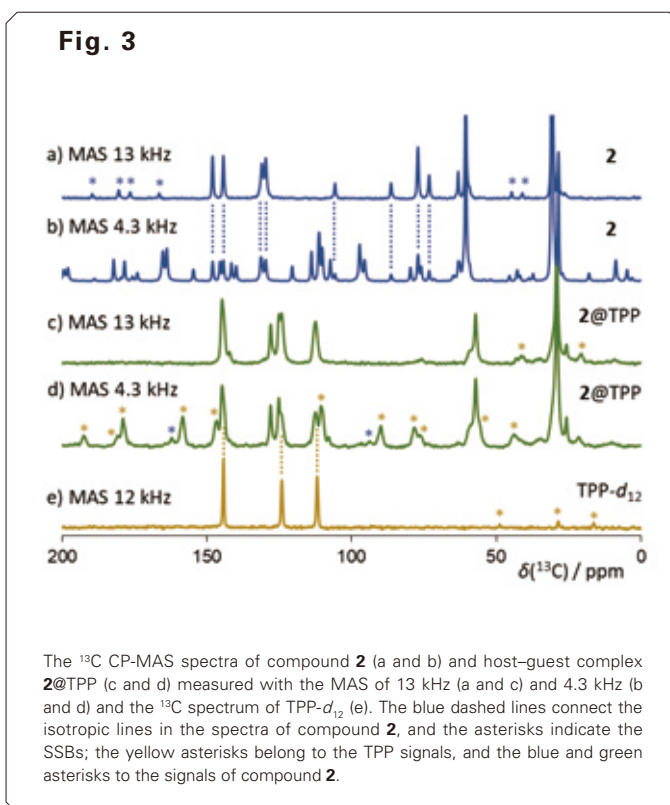
## 3) The Surface Inclusion of an Azobenzene Molecular Switch on TPP

Another functional molecule that we prepared and whose surface inclusion complexes on TPP we studied contained a molecular switch based on azobenzene (compound **4**, **Figure 1**). The “passive” part of the molecule is the same as in compound **3** – it contains the same long shaft and the triptycene stopper [46].

Azobenzenes contain the azo group ( $-\text{N}=\text{N}-$ ), which makes the compounds colorful. Apart from their use as colorants, azo compounds have found many applications in the fields of molecular devices and artificial molecular machines [3, 47–50], where the easy *E/Z* photoisomerization of the azo group is exploited. In most cases, the *E* arrangement is more stable than the *Z* arrangement. However, irradiation with UV or visible light can lead to *E/Z* isomerization. The resulting metastable *Z* isomer then rearranges back to the *E* isomer either thermally or by another UV/vis irradiation.

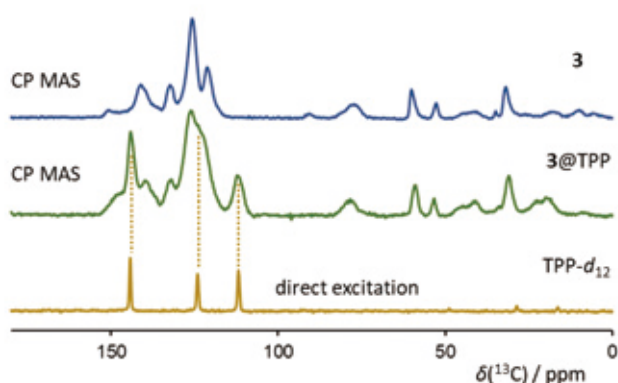
The *E/Z* photoisomerization can be followed by  $^{15}\text{N}$  NMR spectroscopy, because the signals of azo nitrogens are substantially different for the two isomers. In order to facilitate these measurements, compound **4** was prepared as  $^{15}\text{N}$ -labelled in one of the azogroup nitrogen atoms (**Figure 1**). **Figure 6a** and **6b** depicts the solution-state  $^{15}\text{N}$  spectra of compound **4** before and after UV irradiation. The nitrogen chemical shift increases by 23 ppm upon the formation of the *Z* isomer.

The *E/Z* photoisomerization of the surface inclusion complexes of compound **4** in TPP has been investigated by SS-NMR. The SS-NMR nitrogen signal of the surface inclusion is in the same position as the signal of the *E* isomer in solution, but



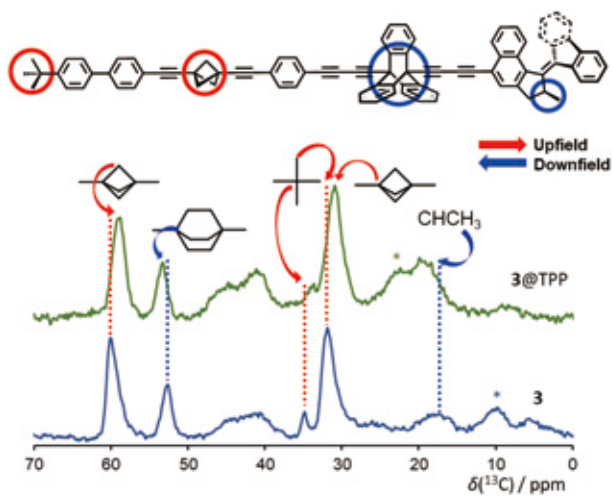
the SS-NMR signal is significantly broader (Figure 6c). After irradiation, new  $^{15}\text{N}$  signal appears in the spectrum close to the position of the signal of the *Z* isomer in solution (Figure 6d). The preparation and observation of the *Z* isomer was challenging for two reasons: First, the inclusion compound is optically dense and cannot be irradiated through the entire volume of the sample. Therefore, we irradiated the sample for four hours and regularly mixed the powder sample under the irradiation device. Second, the thermal back isomerization could destroy the *Z* isomer before it was measured. Therefore, the irradiation was performed at low temperature of 8 °C, the SS-NMR experiments at -20 °C, and the MAS speed was reduced to 12 kHz. Note that MAS leads to frictional heating of the sample and the decrease in the spinning speed significantly reduces the frictional heating.

Fig. 4



The solid-state  $^{13}\text{C}$  NMR spectra of TPP- $d_{12}$ , compound **3** and the inclusion complex of **3** in TPP- $d_{12}$ .

Fig. 5



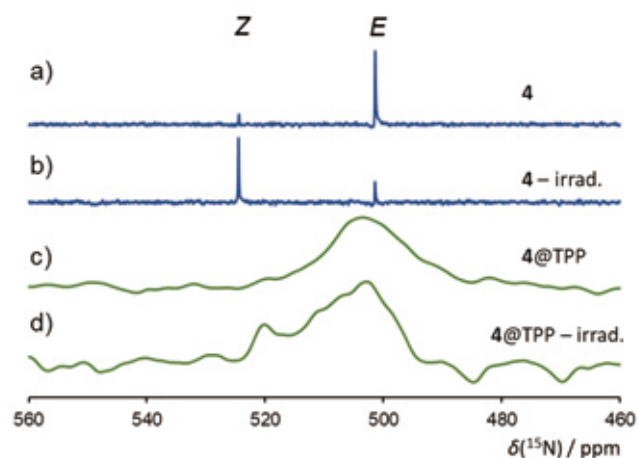
A part of the  $^{13}\text{C}$  CP-MAS spectra of compound **3** and the inclusion complex **3@TPP- $d_{12}$**  with partial signal assignment. The red dashed lines indicate the signals of compound **3** that are shifted upfield upon complexation, while the blue dashed lines mark downfield-shifted signals. The asterisks indicate spinning sidebands. Note that the spectrum of **3** has been acquired at a higher MAS speed (14.5 kHz) than the spectrum of **3@TPP** (13 kHz).

#### 4) Host-Guest Complexes of Cucurbit[7]urils

Apart from TPP, we have also investigated another type of inclusion hosts – cucurbiturils. The host-guest complexes were also prepared by ball-milling. Cucurbit[*n*]uril macrocycles (CB[*n*]) are well-established hosts for the encapsulation of guests in water solutions [51-53], often with extreme binding affinities (up to  $7.2 \times 10^{17} \text{ M}^{-1}$ ) [54-56]. However, many of the potential guests are insoluble in water. To overcome this complication, we have demonstrated that mechanochemistry can be used for the preparation of host-guest complexes with CB[7] by simple solvent-free ball-milling of both substrates [57].

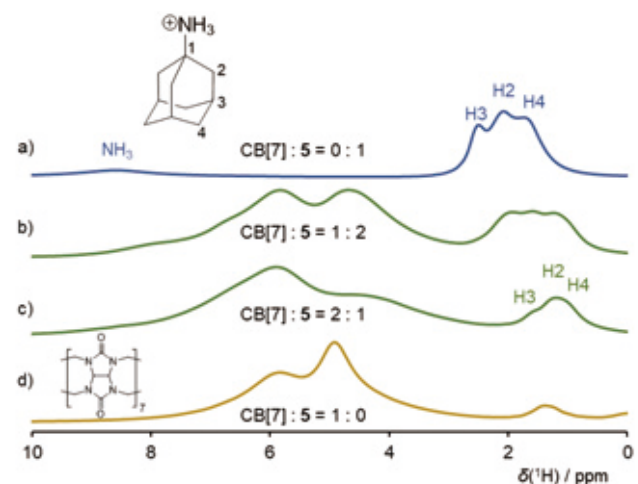
As an example, **Figure 7** depicts the proton SS-NMR spectra of a selected guest (1-adamantylammonium hydrochloride,

Fig. 6



The nitrogen NMR spectra of compound **4** in THF- $d_6$  solution a) before and b) after UV irradiation. The  $^{15}\text{N}$  CP-MAS spectra of the surface inclusion of compound **4** on TPP c) before and d) after UV irradiation.

Fig. 7



The  $^1\text{H}$  SS-NMR spectra of ball-milled (a) compound **5**, (b) a 1:2 mixture of CB[7] and **5**, (c) a 2:1 mixture of CB[7] and **5**, and (d) pure CB[7].

compound **5**), of pure CB[7] and of their host–guest complexes. The encapsulation of compound **5** leads to significant chemical-shift changes of the guest. The proton signals were assigned by means of a proton-detected 2D INEPT spectrum, showing C–H correlations via heteronuclear *J*-coupling (Figure 8). The spatial proximity of the host and guest was confirmed by a proton double-quantum (DQ) – single-quantum (SQ) experiment, which shows through-space interactions of the compounds (Figure 9).

## Conclusions

SS-NMR experiments provide a unique opportunity for the investigation of 2D and 3D assemblies of functional molecules, such as molecular rotors, motors and switches. The formation of the host–guest complexes has been confirmed by CP experiments with a deuterated host, by chemical-shift changes of the guest, by changes of the signal intensities of triple-bond carbon atoms, and by 2D proton-detected NMR experiments. Furthermore, SS-NMR experiments have confirmed the photoisomerization of the molecular switches deposited on the TPP surface.

## Experimental Notes

**Ball milling.** A pure host (TPP or CB[7], ~0.025 mmol) was ball-milled at 25 °C for 5 min using a stainless-steel ball mill. Subsequently, pure guest **1–4** was added and the mixture was ball-milled four consecutive times for 5 min. After each cycle, the milling chamber was opened and the glassy solid material was thoroughly scratched from the mill walls.

**Solid-state NMR experiments.** High-resolution <sup>1</sup>H, <sup>13</sup>C, <sup>15</sup>N and <sup>31</sup>P solid-state NMR spectra were obtained using a JEOL ECZ600R spectrometer, operating at 150.9 MHz for <sup>13</sup>C, at 60.8 MHz for <sup>15</sup>N, at 243.0 MHz for <sup>31</sup>P and at 600.2 MHz for <sup>1</sup>H, and a Bruker Avance II spectrometer, operating at 125.7 MHz for <sup>13</sup>C, at 202.4 MHz for <sup>31</sup>P, and at 499.9 MHz for <sup>1</sup>H. Samples were packed into 1- and 3.2-mm (MAS) rotors and

measurements were taken at the MAS rates of 70 and 12–18 kHz, respectively. The <sup>13</sup>C, <sup>15</sup>N and <sup>31</sup>P spectra were measured using either CP or direct excitation. The ramped-amplitude shape pulse was used during the cross-polarization. The contact time for the CP was 5 ms for <sup>13</sup>C and <sup>31</sup>P and 10 ms for <sup>15</sup>N. The signals were assigned by means of a 2D double-CP experiment and 2D CP-INEPT experiment, showing C–H correlations via dipolar coupling or *J*-coupling, respectively. These 2D experiments were performed at the MAS rates of 70 kHz. The <sup>1</sup>H–<sup>1</sup>H DQ–SQ MAS spectra were recorded using the rotor-synchronized back-to-back (BABA) recoupling pulse sequence at the MAS rates of 70 kHz [58].

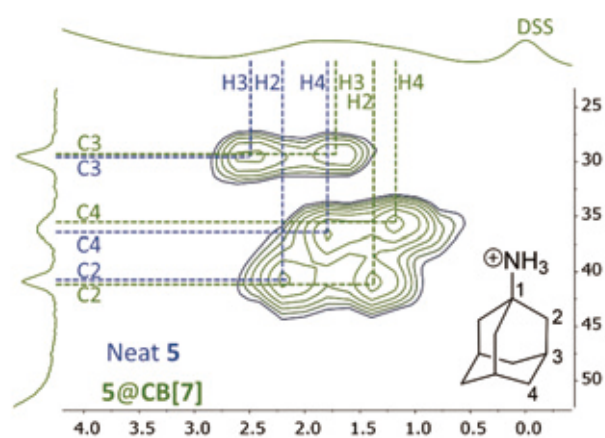
## Acknowledgments

This work was supported by the Czech Science Foundation (grants no. 20-01472S and 20-13745S).

## References

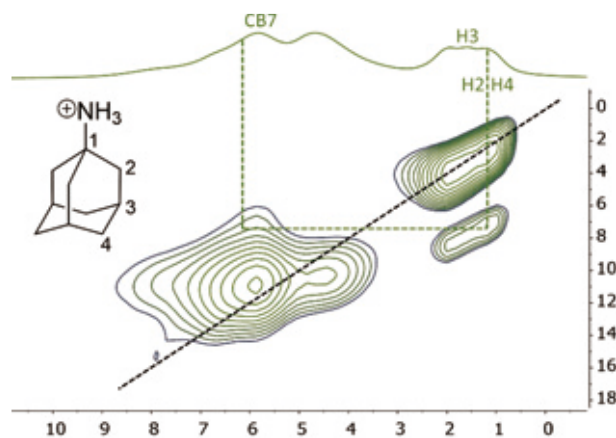
- [ 1 ] K. Kinbara and T. Aida, *Chem. Rev.*, 2005, **105**, 1377–1400.
- [ 2 ] W. R. Browne and B. L. Feringa, *Nat. Nanotechnol.*, 2006, **1**, 25–35.
- [ 3 ] S. Erbas-Cakmak, D. A. Leigh, C. T. McTernan and A. L. Nussbaumer, *Chem. Rev.*, 2015, **115**, 10081–10206.
- [ 4 ] A. Coskun, M. Banaszak, R. D. Astumian, J. F. Stoddart and B. A. Grzybowski, *Chem. Soc. Rev.*, 2012, **41**, 19–30.

Fig. 8



A 2D CP-INEPT SS-NMR spectrum of a ball-milled mixture of CB[7] and **5** in 1:2 ratio, showing C–H correlations via heteronuclear *J*-coupling, measured at the MAS speed of 70 kHz.

Fig. 9



The <sup>1</sup>H–<sup>1</sup>H DQ–SQ MAS spectrum of a mixture of compound **5** and CB[7] (2:1 ratio) obtained using a rotor-synchronized back-to-back (BABA) recoupling at the MAS rate of 70 kHz.

- [ 5 ] G. S. Kottas, L. I. Clarke, D. Horinek and J. Michl, *Chem. Rev.*, 2005, **105**, 1281-1376.
- [ 6 ] S. Kassem, T. van Leeuwen, A. S. Lubbe, M. R. Wilson, B. L. Feringa and D. A. Leigh, *Chem. Soc. Rev.*, 2017, **46**, 2592-2621.
- [ 7 ] A. M. Schoevaars, W. Kruizinga, R. W. J. Zijlstra, N. Veldman, A. L. Spek and B. L. Feringa, *J. Org. Chem.*, 1997, **62**, 4943-4948.
- [ 8 ] S. Hiraoka, Y. Hisanaga, M. Shiro and M. Shionoya, *Angew. Chem. Int. Ed.*, 2010, **49**, 1669-1673.
- [ 9 ] R. A. Bissell, E. Cordova, A. E. Kaifer and J. F. Stoddart, *Nature*, 1994, **369**, 133-137.
- [10] J. V. Hernandez, E. R. Kay and D. A. Leigh, *Science*, 2004, **306**, 1532-1537.
- [11] N. Koumura, R. W. J. Zijlstra, R. A. van Delden, N. Harada and B. L. Feringa, *Nature*, 1999, **401**, 152-155.
- [12] D. A. Leigh, J. K. Y. Wong, F. Dehez and F. Zerbetto, *Nature*, 2003, **424**, 174-179.
- [13] S. P. Fletcher, F. Dumur, M. M. Pollard and B. L. Feringa, *Science*, 2005, **310**, 80-82.
- [14] J. D. Badjić, V. Balzani, A. Credi, S. Silvi and J. F. Stoddart, *Science*, 2004, **303**, 1845-1849.
- [15] S. Kassem, A. T. L. Lee, D. A. Leigh, A. Markevicius and J. Sola, *Nat. Chem.*, 2016, **8**, 138-143.
- [16] J. W. Chen, S. J. Wezenberg and B. L. Feringa, *Chem. Commun.*, 2016, **52**, 6765-6768.
- [17] T. Kudernac, N. Ruangsapapichat, M. Parschau, B. Macia, N. Katsonis, S. R. Harutyunyan, K. H. Ernst and B. L. Feringa, *Nature*, 2011, **479**, 208-211.
- [18] M. von Delius, E. M. Geertsema and D. A. Leigh, *Nat. Chem.*, 2010, **2**, 96-101.
- [19] G. Ragazzon, M. Baroncini, S. Silvi, M. Venturi and A. Credi, *Nat. Nanotechnol.*, 2015, **10**, 70-75.
- [20] B. Lewandowski, G. De Bo, J. W. Ward, M. Pappmeyer, S. Kuschel, M. J. Aldegunde, P. M. E. Gramlich, D. Heckmann, S. M. Goldup, D. M. D'Souza, A. E. Fernandes and D. A. Leigh, *Science*, 2013, **339**, 189-193.
- [21] A. R. Pease, J. O. Jeppesen, J. F. Stoddart, Y. Luo, C. P. Collier and J. R. Heath, *Acc. Chem. Res.*, 2001, **34**, 433-444.
- [22] D. H. Qu, Q. C. Wang, Q. W. Zhang, X. Ma and H. Tian, *Chem. Rev.*, 2015, **115**, 7543-7588.
- [23] R. Klajn, *Chem. Soc. Rev.*, 2014, **43**, 148-184.
- [24] M. M. Russew and S. Hecht, *Adv. Mater.*, 2010, **22**, 3348-3360.
- [25] V. Balzani, A. Credi and M. Venturi, *ChemPhysChem*, 2008, **9**, 202-220.
- [26] R. A. van Delden, M. K. J. ter Wiel, M. M. Pollard, J. Vicario, N. Koumura and B. L. Feringa, *Nature*, 2005, **437**, 1337-1340.
- [27] J. Berná, D. A. Leigh, M. Lubomska, S. M. Mendoza, E. M. Perez, P. Rudolf, G. Teobaldi and F. Zerbetto, *Nat. Mater.*, 2005, **4**, 704-710.
- [28] H. L. Tierney, C. J. Murphy, A. D. Jewell, A. E. Baber, E. V. Iski, H. Y. Khodaverdian, A. F. McGuire, N. Klebanov and E. C. H. Sykes, *Nat. Nanotechnol.*, 2011, **6**, 625-629.
- [29] J. Kaleta, J. W. Chen, G. Bastien, M. Dračinský, M. Mašát, C. T. Rogers, B. L. Feringa and J. Michl, *J. Am. Chem. Soc.*, 2017, **139**, 10486-10498.
- [30] K. L. Zhu, C. A. O'Keefe, V. N. Vukotic, R. W. Schurko and S. J. Loeb, *Nat. Chem.*, 2015, **7**, 514-519.
- [31] H. X. Deng, M. A. Olson, J. F. Stoddart and O. M. Yaghi, *Nat. Chem.*, 2010, **2**, 439-443.
- [32] J. Kaleta, G. Bastien, J. Wen, M. Dračinský, E. Tortorici, I. Cisařová, P. D. Beale, C. T. Rogers and J. Michl, *J. Org. Chem.*, 2019, **84**, 8449-8467.
- [33] Q. Li, G. Fuks, E. Moulin, M. Maaloum, M. Rawiso, I. Kulic, J. T. Foy and N. Giuseppone, *Nat. Nanotechnol.*, 2015, **10**, 161-165.
- [34] A. Natansohn and P. Rochon, *Chem. Rev.*, 2002, **102**, 4139-4175.
- [35] C. L. van Oosten, C. W. M. Bastiaansen and D. J. Broer, *Nat. Mater.*, 2009, **8**, 677-682.
- [36] S. Iamsaard, S. J. Asshoff, B. Matt, T. Kudernac, J. J. L. M. Cornelissen, S. P. Fletcher and N. Katsonis, *Nat. Chem.*, 2014, **6**, 229-235.
- [37] R. Eelkema, M. M. Pollard, J. Vicario, N. Katsonis, B. S. Ramon, C. W. M. Bastiaansen, D. J. Broer and B. L. Feringa, *Nature*, 2006, **440**, 163-163.
- [38] A. D. Bond, *CrystEngComm*, 2012, **14**, 2363-2366.
- [39] R. K. Harris, *Analyst*, 2006, **131**, 351-373.
- [40] M. Dračinský, M. Buděšinský, B. Warzajtis and U. Rychlewska, *J. Phys. Chem. A*, 2012, **116**, 680-688.
- [41] M. Dračinský and P. Hodgkinson, *RSC Adv.*, 2015, **5**, 12300-12310.
- [42] P. Florian and D. Massiot, *CrystEngComm*, 2013, **15**, 8623-8626.
- [43] H. E. Kerr, H. E. Mason, H. A. Sparkes and P. Hodgkinson, *CrystEngComm*, 2016, **18**, 6700-6707.
- [44] C. M. Gall, T. A. Cross, J. A. Diverdi and S. J. Opella, *Proc. Nat. Acad. Sci. USA*, 1982, **79**, 101-105.
- [45] P. Paluch, T. Pawlak, A. Jeziorna, J. Trebosc, G. J. Hou, A. J. Vega, J. P. Amoureux, M. Dračinský, T. Polenova and M. J. Potrzebowski, *Phys. Chem. Chem. Phys.*, 2015, **17**, 28789-28801.
- [46] C. S. Hurtado, G. Bastien, M. Mašát, J. R. Štoček, M. Dračinský, I. Rončević, I. Cisařová, C. T. Rogers and J. Kaleta, *J. Am. Chem. Soc.*, 2020, **142**, 9337-9351.
- [47] F. Lancia, A. Ryabchun and N. Katsonis, *Nat. Rev. Chem.*, 2019, **3**, 536-551.
- [48] W. A. Velema, W. Szymanski and B. L. Feringa, *J. Am. Chem. Soc.*, 2014, **136**, 2178-2191.
- [49] R. Göstl, A. Senf and S. Hecht, *Chem. Soc. Rev.*, 2014, **43**, 1982-1996.
- [50] S. Steinwand, Z. L. Yu, S. Hecht and J. Wachtveitl, *J. Am. Chem. Soc.*, 2016, **138**, 12997-13005.
- [51] E. Masson, X. X. Ling, R. Joseph, L. Kyeremeh-Mensah and X. Y. Lu, *RSC Adv.*, 2012, **2**, 1213-1247.
- [52] K. I. Assaf and W. M. Nau, *Chem. Soc. Rev.*, 2015, **44**, 394-418.
- [53] S. J. Barrow, S. Kaser, M. J. Rowland, J. del Barrio and O. A. Scherman, *Chem. Rev.*, 2015, **115**, 12320-12406.
- [54] L. P. Cao, M. Sekutor, P. Y. Zavalij, K. Mlinaric-Majerski, R. Glaser and L. Isaacs, *Angew. Chem. Int. Ed.*, 2014, **53**, 988-993.
- [55] M. V. Rekharsky, T. Mori, C. Yang, Y. H. Ko, N. Selvapalam, H. Kim, D. Sobransingh, A. E. Kaifer, S. M. Liu, L. Isaacs, W. Chen, S. Moghaddam, M. K. Gilson, K. M. Kim and Y. Inoue, *Proc. Natl. Acad. Sci. USA*, 2007, **104**, 20737-20742.
- [56] S. Moghaddam, C. Yang, M. Rekharsky, Y. H. Ko, K. Kim, Y. Inoue and M. K. Gilson, *J. Am. Chem. Soc.*, 2011, **133**, 3570-3581.
- [57] M. Dračinský, C. Santos-Hurtado, E. Masson and J. Kaleta, *Chem. Commun.*, 2021, **57**, 2132-2135.
- [58] W. Sommer, J. Gottwald, D. E. Demco and H. W. Spiess, *J. Magn. Reson. A*, 1995, **113**, 131-134.

# Dioxins Analysis with New GC-MS/MS System and Software "TQ-DioK"

Imane Senoussaoui<sup>1</sup>, Masahiro Hashimoto<sup>1</sup>,  
Thomas Lehardy<sup>2</sup>, Anais Venisseau<sup>2</sup>, Philippe Marchand<sup>2</sup>

<sup>1</sup> JEOL (EUROPE) SAS, France

<sup>2</sup> Laboratoire d'Etude des Résidus et Contaminants dans les Aliments (LABERCA), Nantes, France

The Sector Mass spectrometer (MS) combined with gas-chromatograph (GC-HRMS) was the official method used for polychlorinated dibenzo-p-dioxins (PCDDs) and dibenzofurans (PCDFs) analysis due to its high selectivity and high sensitivity for those compounds. It is still mainly used in expert laboratories. The European commission regulation has been amended in 2014 (EU589/2014) and now allows the use of the GC-triple quadrupole MS system for PCDDs and PCDFs (PCDD/Fs) analysis to check the compliance of samples [1]. In this study, we have quantified PCDD/Fs using the new JEOL GC-triple quadrupole MS called JMS-TQ4000GC. The software TQ-DioK which is dedicated to dioxins analysis was used to process the data.

## Introduction

Dioxins are a general term for PCDD/Fs. Their structures consist of two chlorinated rings. Many congeners differ in term of number of chlorine atoms and binding sites (**Fig. 1**).

These substances are considered as persistent organic pollutants (POPs) due to their presence in the environment and the health risks associated. A World Health Organization (WHO) study has demonstrated the health risks (carcinogenic and immunotoxic) when population are exposed to them [2]. In addition, PCDD/Fs have been regulated by the Stockholm convention on POPs in May 2001 [3].

In particular, 17 substances have to be monitored because they are regulated (7 PCDDs and 10 PCDFs). The highest toxic compound is the 2378-TeCDD (**Fig. 2**).

Currently, dioxins analysis can be done not only using GC-HRMS but also with GC-MS/MS according to European commission regulation (2014). GC-triple quadrupole MS is interesting in terms of handling, instrument size and operating costs.

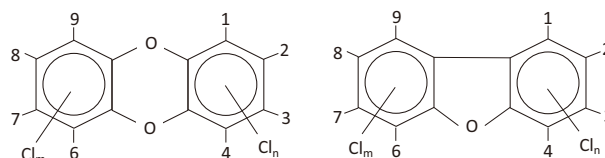
Recently, JEOL has developed a new GC-triple quadrupole MS (JMS-TQ4000GC) and a new dedicated dioxins analysis software called TQ-DioK. In this study, we evaluated JMS-TQ4000GC with TQ-DioK using dioxins standard samples and several real samples.

## Instrument JMS-TQ4000GC

The collision cell of JMS-TQ4000GC is a unique technology called short collision cell (Patent No.: US8692191, EP2469578,

US8604420) [4]. It allows to carry out high speed and high sensitivity quantitative measurements. The switch between "high speed" and "high sensitivity" modes is easy to do, by changing accumulation time for ions in the short collision cell. Besides, new compounds can be added on the SRM data file using the SRM optimization tool. Therefore, dioxins data obtained can be analyzed smoothly.

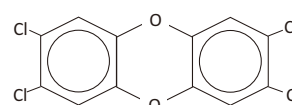
**Fig. 1 The structures of PCDDs(A) and PCDFs(B)**



(A) PCDDs

(B) PCDFs

**Fig. 2 The structure of 2378-TeCDD**



## TQ-DioK

JEOL has introduced a dedicated GC-triple quadrupole MS software specialized in MS/MS data analysis: TQ-DioK. It is a quantitative analysis software dedicated to dioxins analysis. The data processing is very special, because dioxins compounds consist of many isomers with the same basic composition and an isotopic dilution technique is required for their determination. JEOL already provides a quantitative analysis software for dioxins analysis (DioK) dedicated to the GC-Sector MS. Its features were ported to TQ-DioK. Therefore, dioxins data obtained can be analyzed smoothly.

The TQ-DioK analysis window is a “three-layer chromatogram window”. On the upper part, the chromatogram of native compounds is represented, and on the lower part of the window we can find the chromatogram of internal standard (IS) compounds and between the 2 chromatograms the calculated retention time (RT).

As a result, the peak can be identified and assigned to a specified isomer by comparing the peak position between the chromatogram of native compounds, the chromatogram of IS compounds and calculated RT of compounds. Since the RT axis always synchronizes with each isomer, it is easy to check the chromatogram of each isomer, and identify the peak status by an associated coloring system (Fig. 3).

## Experimental Standard sample measurement Samples

The standard PCDD/Fs solutions (DF-IS-A, DF-ST-A and DF-LCS-C from WELLINGTON Laboratories (CANADA)) were used for the measurement. Then, the range of concentrations for calibration curve was prepared from 0.025 to 1 pg/μL (OCDD and OCDF: 0.05 - 2 pg/μL) (Table 1).

## GC-MS/MS measurement conditions

Table 2 shows the GC-MS/MS measurement conditions. A split/splitless inlet was used, and nitrogen gas was applied as collision gas. Table 3 shows the precursor ion, product ion and collision energy (CE). Two specific precursor ions from each non-labeled compound and labeled compound were set.

## Results for standard samples

The GC-MS/MS method was validated in term of chromatographic separation, sensitivity and RRF. Some criteria, especially separation and RRF have to comply with EU commission regulation.

Fig. 3 Analysis view of TQ-DioK

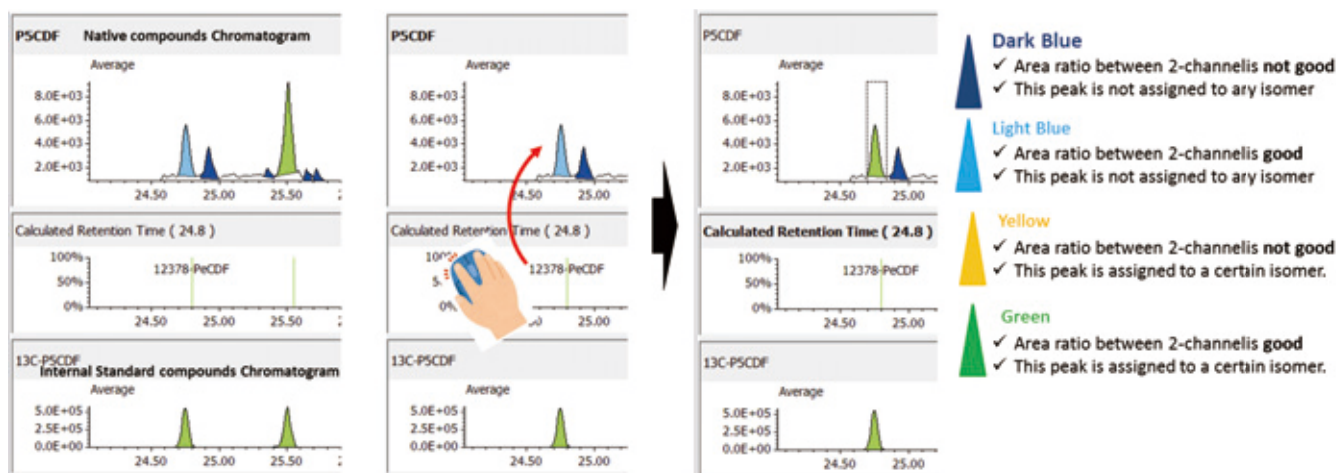


Table 1 Concentrations of each calibration point

PCDD/Fs	Concentration <sup>12</sup> C (pg/μL)	Concentration <sup>13</sup> C (pg/μL)
Cal. 1	0.025(OCDD and OCDF 0.05)	1.25(OCDD and OCDF 2.5)
Cal. 2	0.05(OCDD and OCDF 0.1)	1.25(OCDD and OCDF 2.5)
Cal. 3	0.1(OCDD and OCDF 0.2)	1.25(OCDD and OCDF 2.5)
Cal. 4	0.25(OCDD and OCDF 0.5)	1.25(OCDD and OCDF 2.5)
Cal. 5	0.5(OCDD and OCDF 1.0)	1.25(OCDD and OCDF 2.5)
Cal. 6	1.0(OCDD and OCDF 2.0)	1.25(OCDD and OCDF 2.5)

**Table 2 Measurement conditions**

[GC]

Inj. volume:	2 µL
Inlet type:	Split/Splitless
Inj. mode:	Splitless (Purge time 1 min, Purge flow 20 mL/min)
Inlet temp.:	280 °C
Column flow:	1 mL/min (Constant flow)
GC column:	DB- 5 MS (60 m × 0.25 mm, 0.25 µm)
Oven temp.:	120 °C (3 min) → 50 °C/min → 200 °C (0 min) → 4 °C/min → 300 °C (5 min) → 40 °C/min → 325 °C (5 min)

[MS]

MS:	JMS-TQ4000GC
Ionization:	EI+
Acquisition mode:	High sensitivity mode
IS temp.:	280 °C
ITF temp:	280 °C

**Table 3 Precursor ion, product ion and CE**

No.	Compound name	Group name	Precursor ion	Product ion	Precursor ion	Product ion	CE(V)
1	13C-2378-TeCDF	13C-T4CDF	315.9	252	317.9	254	25
2	2378-TeCDF	T4CDF	303.9	240.9	305.9	242.9	
3	13C-1234-TeCDD	13C-T4CDD	333.9	270	331.9	268	25
4	13C-2378-TeCDD	13C-T4CDD	331.9	268	333.9	270	
5	2378-TeCDD	T4CDD	321.9	258.9	319.9	256.9	30
6	13C-12378-PeCDF	13C-P5CDF	351.9	287.9	353.9	289.9	
7	12378-PeCDF	P5CDF	339.9	276.9	341.9	278.9	30
8	13C-23478-PeCDF	13C-P5CDF	351.9	287.9	353.9	289.9	
9	23478-PeCDF	P5CDF	339.9	276.9	341.9	278.9	25
10	13C-12378-PeCDD	13C-P5CDD	367.9	303.9	369.9	305.9	
11	12378-PeCDD	P5CDD	355.9	292.9	357.9	294.9	30
12	13C-123478-HxCDF	13C-H6CDF	385.9	321.9	387.9	323.9	
13	123478-HxCDF	H6CDF	373.8	310.9	375.8	312.9	30
14	13C-123678-HxCDF	13C-H6CDF	385.9	321.9	387.9	323.9	
15	123678-HxCDF	H6CDF	373.8	310.9	375.8	312.9	25
16	13C-234678-HxCDF	13C-H6CDF	385.9	321.9	387.9	323.9	
17	234678-HxCDF	H6CDF	373.8	310.9	375.8	312.9	30
18	13C-123478-HxCDD	13C-H6CDD	401.9	337.9	403.9	339.9	
19	123478-HxCDD	H6CDD	389.8	326.9	391.8	328.9	25
20	13C-123678-HxCDD	13C-H6CDD	401.9	337.9	403.9	339.9	
21	123678-HxCDD	H6CDD	389.8	326.9	391.8	328.9	30
22	13C-123789-HxCDD	13C-H6CDD	401.9	337.9	403.9	339.9	
23	123789-HxCDD	H6CDD	389.8	326.9	391.8	328.9	30
24	13C-123789-HxCDF	13C-H6CDF	385.9	321.9	387.9	323.9	
25	123789-HxCDF	H6CDF	373.8	310.9	375.8	312.9	30
26	13C-1234678-HpCDF	13C-H7CDF	419.8	355.9	421.8	357.9	
27	1234678-HeCDF	H7CDF	407.8	344.8	409.8	346.8	30
28	13C-1234678-HpCDD	13C-H7CDD	435.8	371.9	437.8	373.9	
29	1234678-HpCDD	H7CDD	423.8	360.8	425.8	362.8	30
30	13C-1234789-HpCDF	13C-H7CDF	419.8	355.9	421.8	357.9	
31	1234789-HpCDF	H7CDF	407.8	344.8	409.8	346.8	30
32	13C-12346789-OCDD	13C-O8CDD	471.8	407.8	469.8	405.8	
33	12346789-OCDD	O8CDD	459.7	396.8	457.7	394.8	30
34	13C-12346789-OCDF	13C-OCDF	455.8	391.8	453.8	389.8	
35	12346789-OCDF	OCDF	443.8	380.8	441.8	378.8	30

## Separation

123478-HxCDF and 123678-HxCDF peaks were separated perfectly by using GC-MS/MS method (Fig. 4). Indeed EU commission regulation in force, allows a 25% valley between these 2 peaks.

## Sensitivity

All target compounds in the lowest calibration point were detected (Fig. 5). In addition, the lowest calibration point was measured 8 times for the instrument detection limit (IDL) determination. Then, IDL was calculated using 2378-TeCDD. As a result, IDL value was equal to 4 fg (Fig. 6).

## RRF

Fig. 7 shows calibration curves of 2378-TeCDD and 2378-TeCDF. Indeed Table 4 shows the result of relative standard deviation (RSD) of relative response factor (RRF) for the lowest calibration point, average of RRF, RSD of RRF and limit of quantification (LOQ). RSD of RRF obtained with the lowest calibration point was between 2.2 and 12.9%. Average of RRF value was between 0.94 and 1.14.

According to EU regulation, RSD for RRF has to be under 15%. Here, RSD of RRF from the average of all calibration points was within 9.1%. Regarding LOQ, its value was calculated by signal-to-noise (S/N = 3) of the lowest calibration point. As a result, obtained LOQ value was between 0.08 and 1.69 fg/μL.

## Food samples Measurement Extraction and purification

The collected samples were freeze-dried or only dried and then grinded to make a homogenous powder. Subsequently, dioxins were extracted from the powder sample using the Büchi “SpeedExtractor E-914” automated instrument. The extracted samples were purified using the “MIURA GO-4 HT” system. Finally, the purified samples were measured by both GC-HRMS and GC-MS/MS instruments and the results were compared.

## Result Ratio of selected two transition product ions

The tolerance of ratio of the selected two transitions product ions for average value or calculated value should be <math>\pm 15\%</math> according EU regulation.

Average value of each compound was calculated using all calibration points. Those ratios for each compound were within  $\pm 15\%$  of average value (Fig. 8).

## Comparison of GC-HRMS and GC-MS/MS systems

Grass, Egg and Pork fat were measured by both GC-HRMS and GC-MS/MS systems. Toxic Equivalent Quantity (TEQ) was calculated using Toxic Equivalency Factors (TEF) based on WHO 2005 [5]. Fig. 9 shows the comparison data of Grass, Egg and Pork fat. The TEQ calculated for each compound by GC-MS/MS was similar to GC-HRMS result. By consequence the difference between the Dioxin OMS-TEQ in ng/kg of matrix calculated by GC-HRMS and the GC-MS/MS TEQ(dioxins) was within 20%.

**Fig. 4 Separation of 123478-HxCDF and 123678 HxCDF**

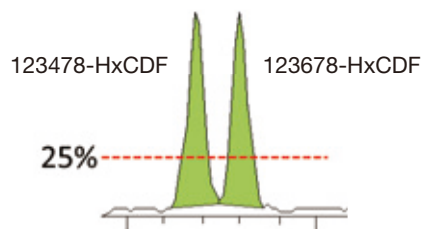


**Fig. 5 Average SRM chromatograms of PCDDs(A) and PCDFs(B) in calibration point 1 (0.05 pg injected)**

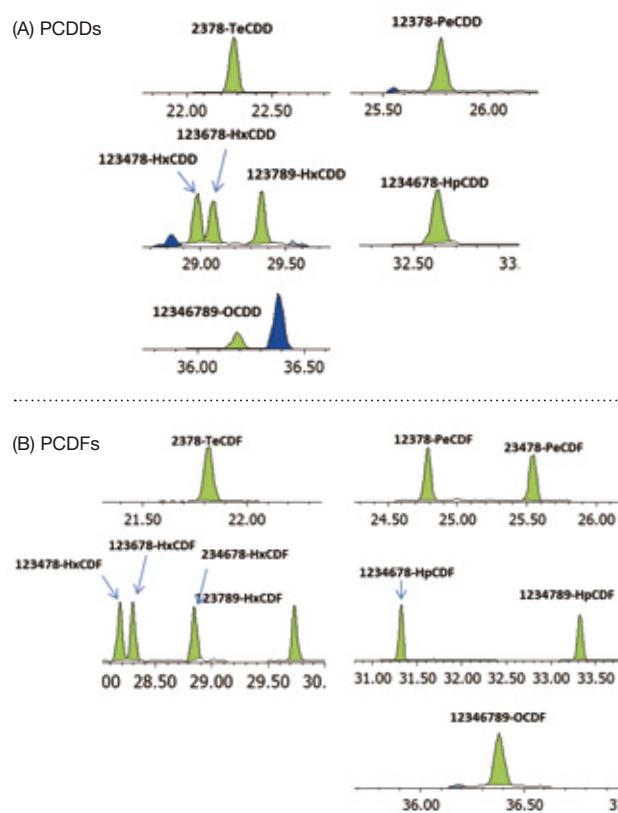


**Fig. 6 IDL data by 2378-TeCDD**

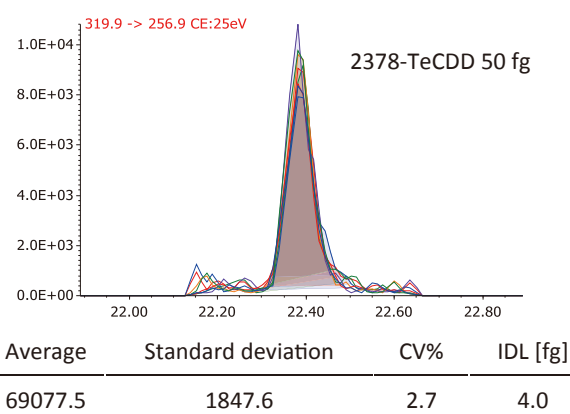
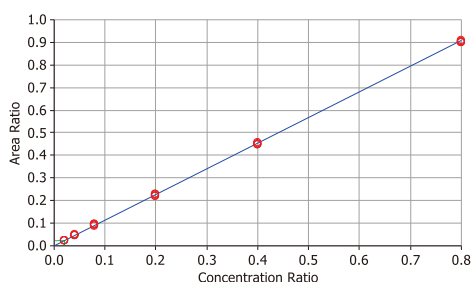


**Fig. 7 Calibration curve of 2378-TeCDD(Left) and 2378-TeCDF(Right)**

**2378-TeCDD**

Calibration curve:RRF  
RRF Average:1.1352  
RRF CV:3.09 %



**2378-TeCDF**

Calibration curve:RRF  
RRF Average:1.048785  
RRF CV:1.90 %

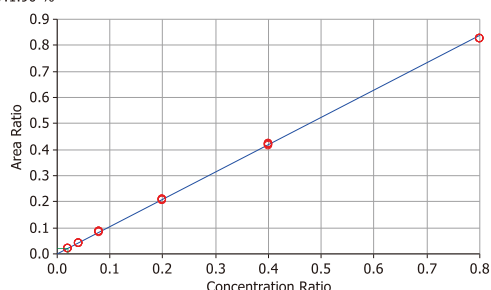


**Table 4 Results of RSD of RRF for the lowest calibration point, average of RRF, RSD of RRF and LOQ**

Compound	Lowest calibration point (pg/μL)	RSD of RRF by the lowest calibration point (%)	Average of RRF	RSD of RRF (%)	LOQ (fg/μL)
<b>PCDFs</b>					
2378-TeCDF	0.025	2.2	1.04	1.8	0.13
12378-PeCDF	0.025	2.3	1.04	2.4	0.45
23478-PeCDF	0.025	4.0	1.05	3.9	0.68
123478-HxCDF	0.025	3.7	1.00	2.9	0.40
123678-HxCDF	0.025	12.9	1.00	6.1	0.36
234678-HxCDF	0.025	8.7	1.03	5.6	0.42
123789-HxCDF	0.025	5.3	1.01	3.5	0.35
1234678-HeCDF	0.025	4.2	1.07	4	0.08
1234789-HpCDF	0.025	5.5	1.04	4	0.08
12346789-OCDF	0.050	4.1	0.95	9.1	1.19
<b>PCDDs</b>					
2378-TeCDD	0.025	3.6	1.14	3.1	0.41
12378-PeCDD	0.025	5.4	1.00	4.1	0.21
123478-HxCDD	0.025	12.5	1.00	6.4	1.46
123678-HxCDD	0.025	12.5	0.94	8.6	1.69
123789-HxCDD	0.025	5.9	1.03	4.5	1.11
1234678-HpCDD	0.025	8.9	1.10	5.8	0.22
12346789-OCDD	0.050	8.3	1.03	9	0.90

**Fig. 8 Ratios of selected two transition product ions**

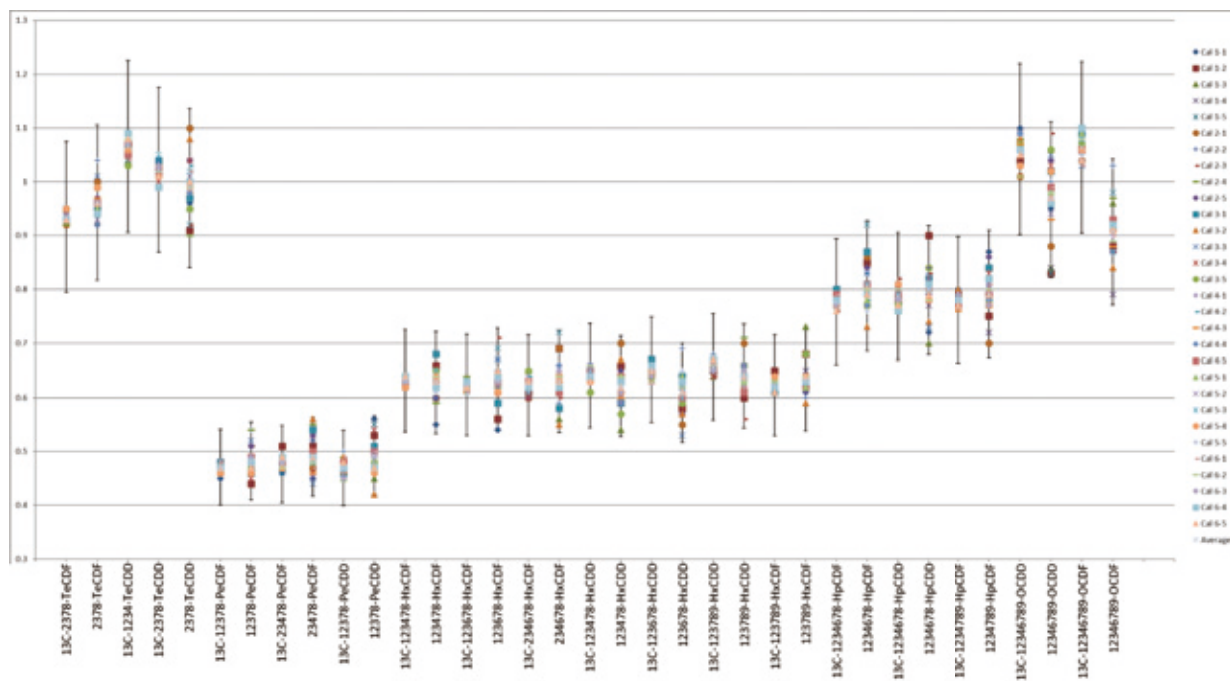
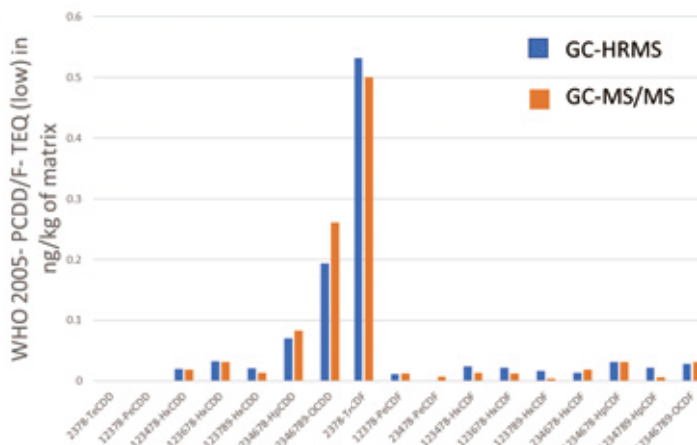


**Fig. 9 Comparison data of GC-HRMS and GC-MS/MS**

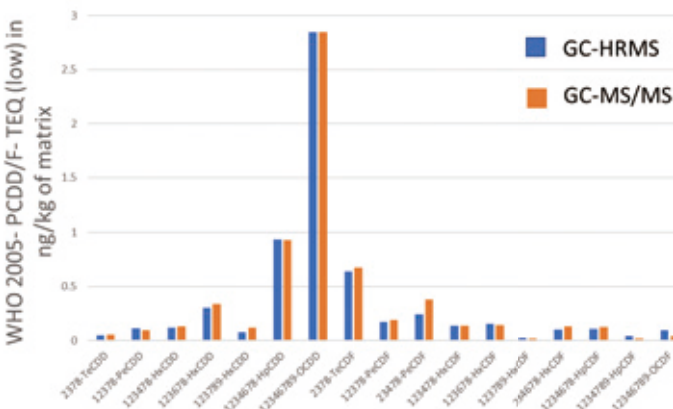
(A) Grass

	GC-HRMS	GC-MS/MS
2378-TeCDD	-	-
12378-PeCDD	-	-
123478-HxCDD	0.020	0.019
123678-HxCDD	0.033	0.032
123789-HxCDD	0.021	0.013
1234678-HpCDD	0.070	0.083
12346789-OCDD	0.193	0.262
2378-TeCDF	0.532	0.500
12378-PeCDF	0.012	0.012
23478-PeCDF	-	0.008
123478-HxCDF	0.025	0.013
123678-HxCDF	0.022	0.013
123789-HxCDF	0.017	0.004
234678-HxCDF	0.014	0.019
1234678-HpCDF	0.031	0.032
1234789-HpCDF	0.022	0.007
12346789-OCDF	0.028	0.032
OMS2005-Dioxin- TEQ (low) in ng/kg of matrix	0.070	0.065



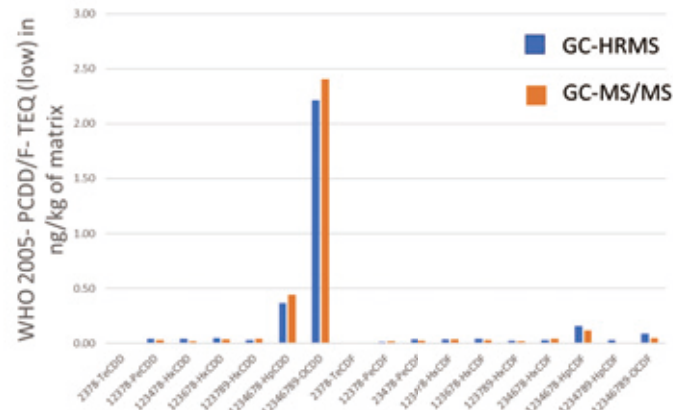
(B) Egg

	GC-HRMS	GC-MS/MS
2378-TeCDD	0.045	0.051
12378-PeCDD	0.112	0.097
123478-HxCDD	0.121	0.133
123678-HxCDD	0.300	0.340
123789-HxCDD	0.079	0.117
1234678-HpCDD	0.936	0.931
12346789-OCDD	2.845	2.848
2378-TeCDF	0.641	0.673
12378-PeCDF	0.173	0.191
23478-PeCDF	0.245	0.381
123478-HxCDF	0.135	0.135
123678-HxCDF	0.156	0.141
123789-HxCDF	0.026	0.021
234678-HxCDF	0.103	0.131
1234678-HpCDF	0.108	0.125
1234789-HpCDF	0.045	0.019
12346789-OCDF	0.093	0.040
OMS2005-Dioxin- TEQ (low) in ng/kg of matrix	0.404	0.449



(C) Pork fat

	GC-HRMS	GC-MS/MS
2378-TeCDD	-	0.001
12378-PeCDD	0.042	0.032
123478-HxCDD	0.041	0.020
123678-HxCDD	0.048	0.038
123789-HxCDD	0.030	0.040
1234678-HpCDD	0.368	0.442
12346789-OCDD	2.216	2.406
2378-TeCDF	0.000	0.009
12378-PeCDF	0.014	0.016
23478-PeCDF	0.036	0.022
123478-HxCDF	0.037	0.036
123678-HxCDF	0.042	0.028
123789-HxCDF	0.026	0.019
234678-HxCDF	0.031	0.042
1234678-HpCDF	0.157	0.119
1234789-HpCDF	0.033	0.004
12346789-OCDF	0.091	0.050
OMS2005-Dioxin- TEQ (low) in ng/kg of matrix	0.084	0.069



## Conclusion

The JMS-TQ4000GC was evaluated for dioxins quantification. The results have shown that the JMS-TQ4000GC instrument complies with the EU commission regulation. In addition, it is easy to identify the chromatogram of each isomer and to confirm the peak status using TQ-DioK software. These results show that the JMS-TQ4000GC system associated with TQ-DioK software are a powerful tool for dioxins analysis.

## Acknowledgement

All measurements and evaluation about the basic performances of JMS-TQ4000GC were organized and tested by

the Laboratoire d'Etude des Résidus et Contaminants dans les Aliments (LABERCA), Nantes, France.

## References

- [ 1 ] COMMISSION REGULATION (EU) 2017/644 of 5 April 2017.
- [ 2 ] World Health Organization, EXPOSURE TO DIOXINS AND DIOXIN-LIKE SUBSTANCES.
- [ 3 ] 15. Stockholm Convention on Persistent Organic Pollutants, Stockholm, 22 May 2001.
- [ 4 ] JEOL News vol.54 No.1, p53 (2019).
- [ 5 ] The 2005 World Health Organization Re-evaluation of Human and Mammalian Toxic Equivalency Factors for Dioxins and Dioxin-like Compounds.

# Characterization of Localized Physical Properties Using High Resolution EELS

Ryosuke Senga, Kazu Suenaga

National Institute of Advanced Industrial Science and Technology, Osaka University

Scanning transmission electron microscopy coupled with electron energy loss spectroscopy (STEM-EELS) is an extremely powerful tool for material characterization that enables simultaneous atomic-level structural and elemental analysis, and it has contributed significantly to the current development of nanomaterials science. Furthermore, the recent development of monochromators for electron microscopy has significantly improved the energy resolution of EELS. This has enabled the measurement of optical and vibrational properties of materials at the nanoscale using electron beams, whereas previously only macroscopic properties could be accessed using light or X-ray probes. In this paper, our research results are reviewed using a monochromatized low-voltage electron microscope (TripleC#2), which was developed in collaboration with JEOL, as an example of the application of high-energy resolution EELS.

## Introduction

Non-periodic structures, such as vacancies and edges in low-dimensional materials, including graphene and carbon nanotubes (CNTs), are closely related to their physical properties. Therefore, it is necessary to investigate the behavior of quasiparticles, such as excitons and phonons, in relation to the structure at the atomic level, to understand their physical properties. However, because of diffraction limits, conventional spectroscopic methods using light or X-rays as probes cannot focus on local structures, such as defects, and the information obtained is averaged over the entire or a wide range of materials.

The monochromatized electron microscope introduced in this paper outperforms the conventional methods in terms of spatial resolution and enables the characterization of the physical properties of individual defects. The energy resolution of the electron beam in a typical transmission electron microscope (TEM) is approximately 400 to 600 meV, and measuring absorption in the infrared and visible light ranges (several tens of meV to several eV) by EELS has been difficult. However, the development of a monochromator has resulted in an energy resolution of approximately 30 meV, which is an order of magnitude higher than that of conventional methods, and even visible [1-5] and infrared [6-9] absorption of materials is now measurable. In addition, by adjusting the electron beam conditions and improving the angular resolution, dispersion relations that extract each momentum component of quasiparticles [10-12] can be obtained. Thus, by maintaining all three elements of spatial, energy, and angular resolution at a high level of efficiency, one can directly access the electronic, optical, and vibrational properties of single atoms, molecules, and individual defects, which have been the focus of

computational science. In the next section, the monochromator is briefly discussed, and experimental studies on the local properties of CNTs and graphene are described.

## Monochromator

TripleC#2 (Fig. 1) was equipped with a double Wien filter type monochromator [13]. The first Wien filter creates an energy-

Fig.1 External view of TripleC#2



dispersive plane, and a slit inserted therein monochromatizes the electron beam. The second Wien filter returns the dispersed electron beam to the point source. The electron beam is then accelerated to the required energy, as in a normal TEM. Because there is a monochromator before the acceleration tube, the energy resolution can be easily changed with little effect on the aberration in the image plane. Therefore, it is relatively easy to obtain multiple spectra that require different energy resolutions (e.g., core-electron and valence excitation loss spectra) from the same sample.

The use of a monochromator has two advantages. One is the improvement in the energy resolution of EELS, which is the subject of this study. The energy resolution of incident electrons in a conventional TEM without a monochromator is approximately 400-600 meV at full width at half maximum. Therefore, low-energy excitations, such as phonons and excitons are buried in the tail of inelastically scattered electron peaks known as zero-loss peaks and cannot be distinguished. However, the monochromator has improved the energy resolution to several tens of meV, which enables the detection of the absorption peaks of quasiparticles with low excitation energy. In addition, the core-electron excitation loss spectra described in the next section provide detailed information on the band structure and electronic state.

The second advantage is the reduction in chromatic aberration, which improves the spatial resolution of the TEM images. Chromatic aberration is a significant limiting factor in the spatial resolution of low-voltage TEMs, whereas a monochromator can suppress it to achieve high spatial resolution even at low accelerations. This topic will not be discussed further in this article, however details can be found in [14-16].

### Core-loss spectroscopy (X-ray region)

In the high-energy range (50 eV-1000 meV) of STEM-EELS, core-electron excitation loss spectra (hereafter referred to as core-loss spectra) can be obtained and used for elemental and chemical state analysis at the single-atom level [17-19]. For example, from the fine structure of core-loss spectra obtained from single atoms using STEM-EELS, the bonding and electronic state of a single carbon atom at the edge of graphene have been measured [18] and the spin state of a single transition metal atom doped in the graphene surface has also been identified [19].

The monochromator provides the highly resolved core-loss spectra and allows us to access richer information of materials. **Figure 2** shows the excitation loss spectrum of a 1s electron (K-edge) obtained from a single CNT. While the conventional energy resolution shows only a single peak at the  $\pi^*$  edge reflecting  $\pi$ -bonding, the monochromator shows multiple subpeaks reflecting the structure of the CNT (Fig. 2(a)). These subpeaks are caused by the excitation of 1s electrons to the singular states in the conduction band (van Hove singularity), which originates from the one-dimensionality of CNTs and reflects their geometric structure (chirality). This highly resolved  $\pi^*$  edges have only been available from bulk samples using X-ray absorption spectra [20], whereas STEM-EELS using monochromatized electron beams can now provide spectra with the same energy resolution from a single CNT. Thus, the  $\pi^*$  fine structure obtained here can be used as a fingerprint to identify the chirality of CNTs. Furthermore, this method can also characterize the modulation of the electronic state in each defect in a CNT [3].

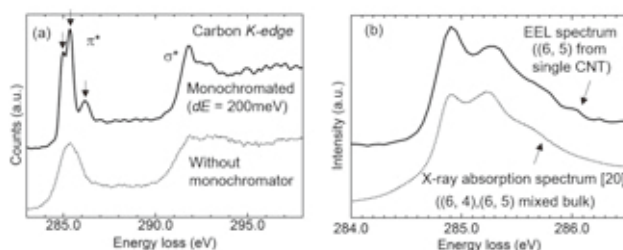
### Valence-loss spectroscopy (visible light region)

In contrast to the core-loss spectrum, the valence excitation loss spectrum captures the relatively low-energy excitation phenomenon when electrons in the valence band are excited to the empty level. With the conventional energy resolution, the main role of EELS is to measure plasmons in the range of several to several tens of eV, however with the improvement of energy resolution, it is now possible to capture absorption in the infrared to near-ultraviolet region from several tens of meV to several eV. In this section, the optical characterization using EELS is discussed.

Optical absorption spectra are generally obtained by irradiating a bulk sample with an incandescent lamp. For example, to obtain the optical absorption spectrum of CNTs, a CNT dispersion solution of deuterium oxide can be used with a surfactant or a solid sample of CNTs in sheet form. These samples usually contain an uncountable number of CNTs, and the resulting spectra are an average of all of them. On the contrary, STEM-EELS can obtain the same or even richer information from a single CNT.

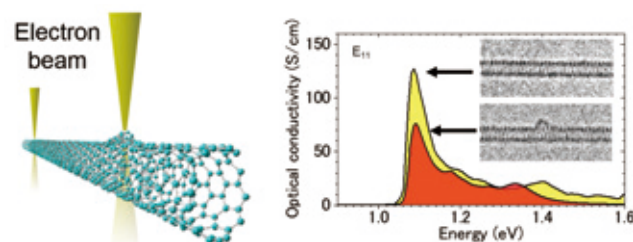
**Figure 3** shows the actual spectrum obtained from a single isolated CNT, which shows strong excitation between the van Hove singularity in the valence and conduction bands and

**Fig. 2 High-resolution core-loss spectra of a single CNT.**



(a) Core-loss spectrum of 1s electrons obtained from a single CNT. (a) Core-loss spectrum of 1s electrons from a single CNT, acquired with the monochromator turned on (solid line) and with the monochromator turned off (dashed line). (b) Comparison of EELS spectrum and X-ray absorption spectrum (XAS), where the XAS (dashed line) is obtained from a bulk sample of CNTs with the same chirality, whereas the EELS spectrum (solid line) is obtained from a single CNT with the same energy resolution as the XAS.

**Fig. 3 Optical characterization of a single CNT using an electron beam.**



By scanning the CNT with a focused beam (left), the  $E_{11}$  peaks of the defective and defect-free areas can be directly compared (right). The Kramers-Kronig transformation is applied to convert the EELS spectrum to optical conductivity for quantitative comparison.

several sharp peaks in the visible light region. Here, we focus on the absorption peak at the highest wavelength ( $E_{11}$ ), which determines the optical properties of the CNTs.  $E_{11}$  contains peaks owing to three factors (exciton, exciton-phonon coupling, and interband transitions), which can be separated from the spectral line shape analysis. Furthermore, the probe size of the electron beam is sufficiently small to directly compare the defective part and the perfectly crystalline part in the same CNT, as shown in Fig. 3, although the signal detectable area of this method is larger than the probe size because of the delocalization of the low-energy excitation. This allows to capture the modulation of the electronic state, band structure, and exciton lifetime at the defects, and to discuss the optical properties of CNT defects in detail. Reference [4] describes the analysis method and a detailed discussion of each peak.

### Measurement of phonon dispersion relation (infrared region)

In the last section, absorption spectra in the infrared region using STEM-EELS is discussed, where pioneering studies have recently been reported consecutively [6-11]. Here, we describe our phonon dispersion relation measurements of graphene [11]. Phonons, which propagate atomic vibrational waves, are involved in all transport properties of materials, including thermal, optical, electrical, and magnetic properties. Therefore, the relationship between vibrational energy and momentum transfer ( $q$ ), that is, the phonon dispersion relation, is one of the most important factors for understanding and optimizing the properties of materials. However, owing to experimental difficulties, it has been hardly possible to measure the phonon dispersion relation from monatomic films of two-dimensional materials, such as graphene. For example, existing inelastic X-ray (neutron) scattering spectroscopy and reflection EELS measurements have a spatial resolution of a few to tens of micrometers and require bulk crystals with sufficient thickness.

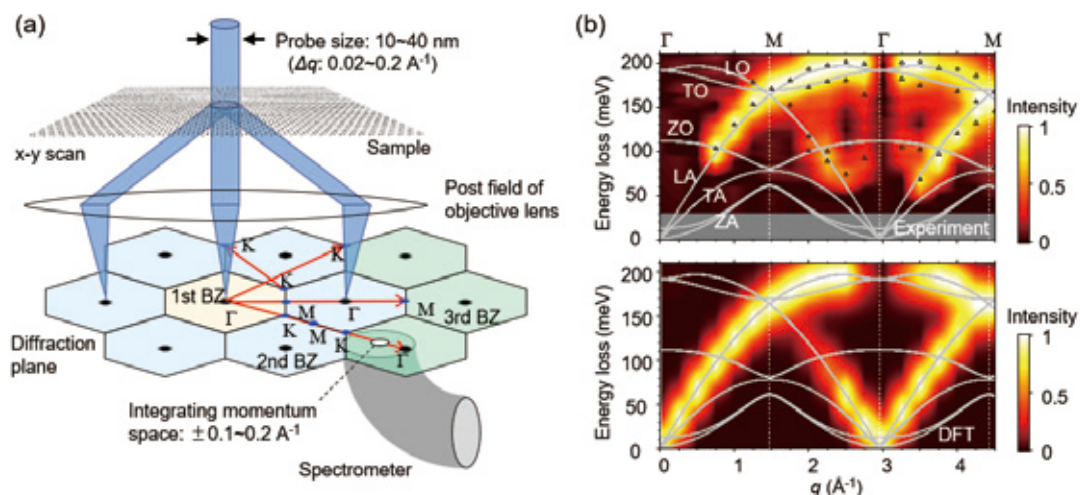
In this study, an angular-resolved EELS is used with a parallel beam that can scan the samples (Fig. 4(a)). The phonon dispersion relation shown in Fig. 4(b) can be obtained by acquiring the vibrational spectrum at each  $q$  with a pinhole-type EELS aperture inserted in the diffraction plane. In this

method, the spectra are obtained from a wide  $q$  range, including the second and third Brillouin zone (BZ) as well as the first one. In fact, it is not sufficient to draw a complete phonon dispersion relation from the first BZ alone. In the case of non-polar materials, such as graphene, the dipole moment between neighboring atoms is small in the lower  $q$  region, and a sufficient signal cannot be obtained. On the contrary, as  $q$  increases, the intensity of the loss peak decreases inversely proportional to  $q^2$  regardless of the polarity of the material; therefore, a sufficient signal cannot be expected.

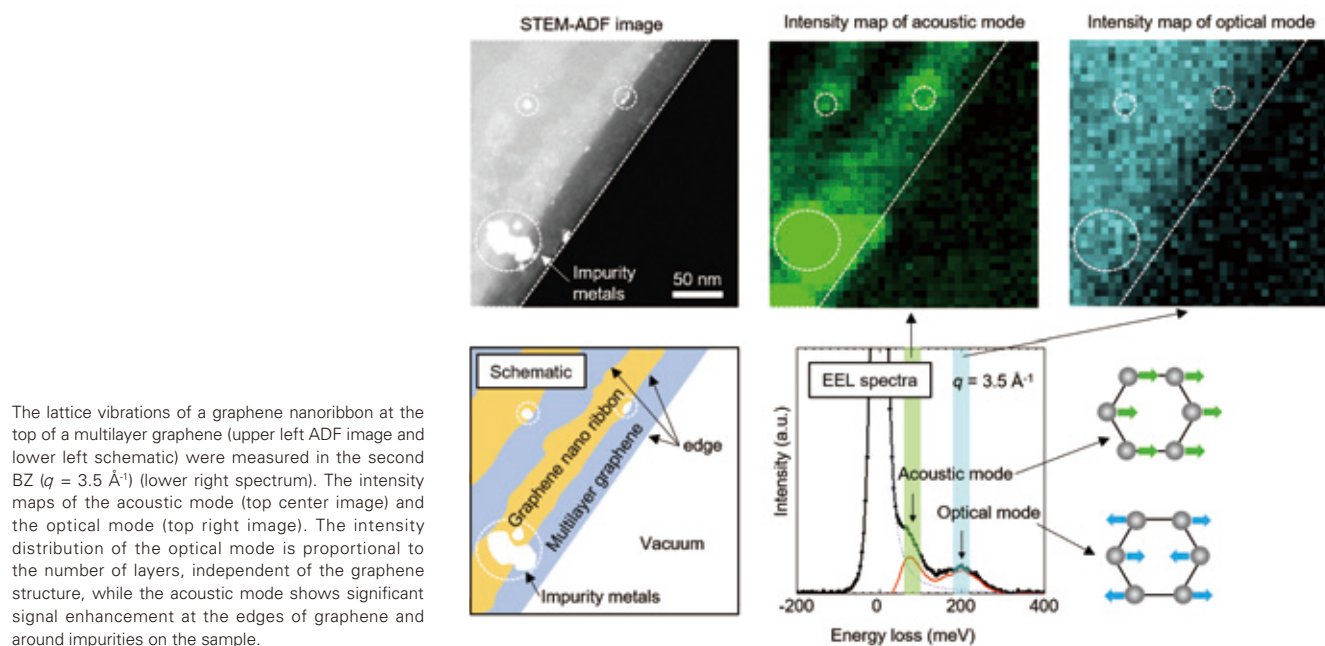
In this study, however, we observed that this is not the case for phonons: as  $q$  increases, the intensity hardly drops even in the outer BZ. Although this result cannot be explained by the conventional rigid-body ion model, we succeeded in reproducing it with high accuracy by theoretical calculations using a unique model that considers the local charge modulation of nuclei (Fig. 4(b)). This finding led to the first measurement of the phonon dispersion relation in graphene monolayers.

The method can measure the energy of phonon excitation with a momentum resolution of less than  $0.2 \text{ \AA}^{-1}$  and a spatial resolution of 10 nm; therefore, it can detect localized lattice vibrations around defects and edges in materials. Figure 5 shows an example of the lattice vibrations in graphene nanoribbons on top of graphite. Here, the sample is scanned at a fixed  $q$  in the second BZ ( $q = 3.5 \text{ \AA}^{-1}$ ), and the intensity distribution of each vibrational mode is mapped. It is interesting to note that the intensity of the longitudinal and transverse optical (LO and TO) modes on the high-energy side depends only on the number of graphene layers, whereas the longitudinal acoustic (LA) modes on the low-energy side show an increase in signal intensity at the edges of graphene nanoribbons and around impurities. Because the acoustic modes are directly related to the thermal properties of the material, the edges of graphene are expected to exhibit different thermal conduction properties than the rest of the sample, and the low-energy peaks are not very straightforward to interpret because they include out-of-plane modes and vibration modes related to the impurities; please refer to Ref. [11] for further details. Because a certain number of defects must be tolerated in actual material applications, there is an increasing demand for such a method that can directly characterize the local structure at the nanoscale.

**Fig. 4 Measurement of phonon dispersion relation of graphene.**



(a) Schematic of nanoscale angular resolved EELS using parallel beam scan. (b) Phonon dispersion relation of the graphene along IM direction from the experiment (top) and calculation (bottom). There is a good agreement including the signal intensity.

**Fig. 5 Localized lattice vibrations at the graphene edge.**

## Summary

The development of the monochromator has significantly improved the energy resolution of EELS, and the range of applications of STEM-EELS has expanded. It is now possible to access the electronic, optical, and vibrational properties of localized regions, such as individual atoms, molecules, or defects that cannot be obtained with conventional methods using X-ray or light probes. Because the modulation of properties in non-periodic structures sometimes dominates all the properties, such local information obtained by monochromatized STEM-EELS is extremely important for discussing the origin of the physical properties of materials. In addition, the identification of isotopic elements using STEM-EELS in the infrared region has been recently reported [9]. These applications may lead to highly sensitive detection of radioactive isotope materials and tracking of chemical reactions using isotope labels in the future.

## Acknowledgments

TripleC#2 was developed in collaboration with JEOL. We would like to thank all the people who supported and worked with us in the setting up and experiments. This study was supported by the Japan Science and Technology Agency (JST) and the Japan Society for the Promotion of Science (JSPS) Grant-in-Aid for Scientific Research.

## References

- [ 1 ] L. H. G. Tizei, Y.-C. Lin, M. Mukai, H. Sawada, A.-Y. Lu, L.-J. Li, K. Kimoto, and K. Suenaga, *Phys. Rev. Lett.* **114**, 107601 (2015).
- [ 2 ] J. Lin, L. Gomez, C. De Weerd, Y. Fujiwara, T. Gregorkiewicz, and K. Suenaga, *Nano Lett.* **16**, 7198 (2016).
- [ 3 ] R. Senga, T. Pichler, and K. Suenaga, *Nano Lett.* **16**, 3661 (2016).
- [ 4 ] R. Senga, T. Pichler, Y. Yomogida, T. Tanaka, H. Kataura, and K. Suenaga, *Nano Lett.* **18**, 3920 (2018).
- [ 5 ] P. K. Gogoi, Y.-C. Lin, R. Senga, H.-P. Komsa, S. L. Wong, D. Chi, A. V. Krasheninnikov, L.-J. Li, M. B. H. Breese, S. J. Pennycook, A. T. S. Wee & K. Suenaga, *ACS Nano* **13**, 9541 (2019).
- [ 6 ] O. L. Krivanek, T. C. Lovejoy, N. Dellby, T. Aoki, R. W. Carpenter, P. Rez, E. Soignard, J. Zhu, P. E. Batson, M. J. Lagos, R. F. Egerton, and P. A. Crozier, *Nature* **514**, 209 (2014).
- [ 7 ] M. J. Lagos, A. Trügler, U. Hohenester & P. E. Batson, *Nature* **543**, 529–532 (2017).
- [ 8 ] F. S. Hage, G. Radtke, D. M. Kepaptsoglou, M. Lazzeri, Q. M. Ramasse, *Science* **367**, 1124–1127 (2020).
- [ 9 ] J. A. Hachtel, J. Huang, I. Popovs, S. J.-Popova, J. K. Keum, J. Jakowski, T. C. Lovejoy, N. Dellby, O. L. Krivanek, J. C. Idrobo, *Science* **363**, 525 (2019).
- [ 10 ] F. S. Hage, R. J. Nicholls, J. R. Yates, D. G. McCulloch, T. C. Lovejoy, N. Dellby, O. L. Krivanek, K. Refson & Q. M. Ramasse, *Science Adv.* **1**, eaar7495 (2018).
- [ 11 ] R. Senga, K. Suenaga, P. Barone, S. Morishita, F. Mauri & T. Pichler, *Nature* **573**, 247–250 (2019).
- [ 12 ] J. Hong, R. Senga, T. Pichler & K. Suenaga, *Phys. Rev. Lett.* **124**, 087401 (2020).
- [ 13 ] M. Mukai, E. Okunishi, M. Ashino, K. Omoto, T. Fukuda, A. Ikeda, K. Somehara, T. Kaneyama, T. Saitoh, T. Hirayama, and Y. Ikuhara, *Microscopy* **64**, 151 (2015).
- [ 14 ] S. Morishita, M. Mukai, K. Suenaga, and H. Sawada, *Appl. Phys. Lett.* **108**, 013107 (2016).
- [ 15 ] S. Morishita, M. Mukai, K. Suenaga, and H. Sawada, *Phys. Rev. Lett.* **117**, 153004 (2016).
- [ 16 ] S. Morishita, R. Senga, Y.-C. Lin, R. Kato, H. Sawada, K. Suenaga *Appl. Phys. Lett.* **113**, 233101 (2018).
- [ 17 ] K. Suenaga, M. Tence, C. Mory, C. Colliex, H. Kato, T. Okazaki, H. Shinohara, K. Hirahara, S. Bandow, and S. Iijima, *Science* **290**, 2280 (2000).
- [ 18 ] K. Suenaga and M. Koshino, *Nature* **468**, 1088 (2010).
- [ 19 ] Y.-C. Lin, P.-Y. Teng, P.-W. Chiu, and K. Suenaga, *Phys. Rev. Lett.* **115**, 206803 (2015).
- [ 20 ] K. De Blauwe, D. J. Mowbray, Y. Miyata, P. Ayala, H. Shiozawa, A. Rubio, P. Hoffmann, H. Kataura, and T. Pichler, *Phys. Rev. B* **82**, 125444 (2010).

# In-Resin CLEM of Epon-Embedded Cells Using Fluorescent Proteins

Isei Tanida, Junji Yamaguchi, Soichiro Kakuta, and Yasuo Uchiyama

Juntendo University Graduate School of Medicine

In-resin CLEM of Epon embedded samples is able to greatly simplify the correlation of fluorescent images with electron micrographs. However the limitation of this technique was the low number of fluorescent proteins that retains fluorescence in the Epon-embedding. For this purpose, we found mWasabi, CoGFP variant 0, mKate2-GGGGSL, mCherry2; two green and two far-red fluorescent proteins. These proteins retain fluorescence after chemical fixation with glutaraldehyde, osmium tetroxide-staining, dehydration, and polymerization of Epoxy resins. Using mKate2-fusion proteins, we demonstrated in-resin CLEM of organelles (mitochondria, the Golgi, and endoplasmic reticulum) in 100 nm-thin sections of the Epon-embedded cells. In addition, when mitochondria-localized mCherry2 and histone H2B tagged with CoGFP variant 0 were expressed in the cells, far-red and green fluorescent signals of mCherry2 and CoGFP variant 0, respectively, were detected in the 100 nm-thin sections of the Epon-embedded cells. In the same thin sections, we correlated the fluorescent signals with mitochondria and the nucleus using a scanning electron microscope. When endoplasmic reticulum-localized mCherry2 was employed instead of mitochondria-localized mCherry2, two-color in-resin CLEM of the endoplasmic reticulum (ER) and nucleus was also succeeded. mWasabi is also suitable for in-resin CLEM. When ER-localized mWasabi and mitochondria-localized mCherry2 were employed for in-resin CLEM, green and far red fluorescent signals were detected the 100 nm-thin sections of the Epon-embedded cells. In the same thin sections, we correlated the green and far red fluorescent signals with the ER and mitochondria, respectively, using a scanning electron microscope. These results suggested that two-color in-resin CLEM was applied to Epon-embedded cells using these proteins.

## Introduction

Correlative light-electron microscopy (CLEM) combines the advantage of fluorescent and electron microscopy and enables the analysis of fluorescent probe expression at the ultrastructural level [1-6]. In standard CLEM, fluorescent images of cells are obtained after chemical fixation with paraformaldehyde and/or glutaraldehyde. Thereafter, the cells are treated with osmium tetroxide, dehydrated with ethanol, and embedded in epoxy resins [7]. After sectioning the Epon-embedded specimens using an ultramicrotome, electron microscopic images of cells in thin sections are obtained. As a detriment, the chemical modifications caused by fixation and the physical sectioning distort the sample's morphology. These factors affect the accuracy in the correlation of the fluorescent image with electron microscopic image.

One of the most efficient ways to get the highest accuracy overlay of the fluorescent and electron microscopic imaging modalities is to merge fluorescent and electron microscopic images from the same section of epoxy resins. Epon-embedding is one of most robust and popular methods, because it preserves the ultrastructure of cells better and with higher contrast than other methacrylate-based resins. A disadvantage of this technique is that the fluorescent intensity of most fluorescent proteins is significantly decreased during chemical treatments essential for epoxy resin-embedding. A proposed solution for these problems is to use Lowicryl HM20 (acrylate- and methacrylate-based) resins instead of Epon resins and high pressure

freezing and freeze substitution techniques for in-resin CLEM with standard fluorescent proteins (mEGFP, mVenus, mRuby2, and YFP). However, these techniques require special instruments and special resins [8-10].

Considering the advantage of fluorescent proteins and Epon based in-resin CLEM in cell biology, in-resin CLEM of Epon-embedded cells should be developed [11-14]. We and other group found monomeric green and red fluorescent proteins that retain their fluorescence after Epon-embedding [12-14]. These proteins can be visualized using a fluorescence microscope with standard filter sets for green (excitation: 450-490 nm, dichroic mirror: 495 nm (LP), emission: 500-550 nm) and red (excitation: 540-580 nm, dichroic mirror: 585 nm (LP), emission: 592.5-667.5 nm) fluorescent probes. We achieved single- and two-color in-resin CLEM of Epon embedded cells using these proteins.

## Experimental Results Fluorescent proteins that retain their fluorescence after osmium tetroxide staining.

We investigated whether or not monomeric green fluorescent proteins including monomeric enhanced GFP with the A206K mutation (mEGFP) ( $\lambda_{ex}$  max = 488 nm,  $\lambda_{em}$  max = 507 nm, pKa = 6.0) (Addgene plasmid # 164163) [15], mWasabi ( $\lambda_{ex}$  max = 493 nm,  $\lambda_{em}$  max = 509 nm, pKa = 6.5) (Addgene plasmid #

164161) [16], mEosEM [12], and monomeric CoGFP variant 0 isolated from *Cavernularia obesa* (CoGFPv0) ( $\lambda_{\text{ex max}} = 498$  nm,  $\lambda_{\text{em max}} = 507$  nm, pKa = 6.0) [17] retain their fluorescence after osmium-staining. Cells expressing each fluorescent protein were fixed with a mixture of 2% paraformaldehyde and 2.5% glutaraldehyde at 4 °C for 1 h, and stained with 1% osmium tetroxide at 4 °C for 10 min. The retained fluorescence of each green fluorescent protein was detected using a fluorescence microscope with a filter set for green fluorescent probe (Fig. 1) [14]. After osmium-staining, fluorescent intensities of mEGFP, mEosEM, mWasabi, and CoGFP were significantly decreased (Fig. 1A). CoGFPv0 and mWasabi retained brighter fluorescence than that of mEGFP under these conditions (Fig. 1B).

We next analyzed monomeric red fluorescent proteins: mCherry2 ( $\lambda_{\text{ex max}} = 589$  nm,  $\lambda_{\text{em max}} = 610$  nm, pKa = 3.3) (Addgene plasmid # 164162) and mKate2-GGGSGL ( $\lambda_{\text{ex max}} = 588$  nm,  $\lambda_{\text{em max}} = 633$  nm, pKa = 5.4) (WAKO # 160-28651). The fluorescence of both proteins was retained after osmium-staining, while their fluorescent intensities of mKate2-GGGSGL and mCherry2 were decreased (Fig. 1A). mCherry2 retained brighter fluorescence than mKate2 under these conditions (Fig. 1B). These results suggested that it will be possible to achieve single- and two-color in-resin CLEM of Epon-embedded cells using these fluorescent proteins.

### How to prepare Epon-embedded cells suitable for in-resin CLEM.

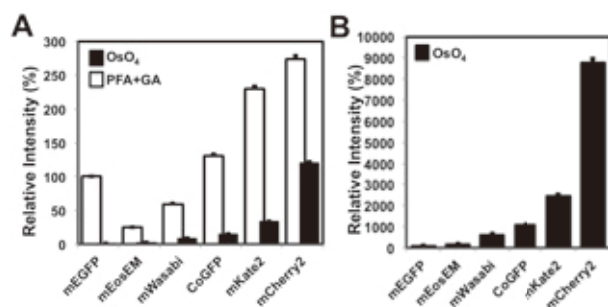
Cells expressing fluorescent proteins and their fusion proteins were prefixed with a fixation solution containing 2% paraformaldehyde and 2.5% glutaraldehyde at 4 °C for 1 h. The fixed cells were washed three times with an HB solution (FUJIFILM WAKO Chemicals, # 080-10591). Fixed cells were

post-fixed in 1% osmium tetroxide at 4 °C for 10 min, and washed three times with an HB solution, incubated in a TUK solution (FUJIFILM WAKO Chemicals, # 209-20851 or 208-21161 for multicolor) at 4 °C for 10 min to recover the fluorescence of the fluorescent proteins, and were washed three times with an HB solution. Cells were dehydrated with a graded series of ethanol, and embedded in Epon812 at 60 °C for 72 h. Thin sections (100 nm) were cut with an ultramicrotome UC6 (Leica) and placed on glass cover slips that were coated with Pt/Au using an ion sputter. Sections were observed in a TUK solution for multicolor using a fluorescence microscope with filter sets for green (excitation: 450-490 nm, dichroic mirror: 495 nm (LP), emission: 500-550 nm), red (excitation: 540-580 nm, dichroic mirror: 585 nm (LP), emission: 592.5-667.5 nm), and blue (excitation: 340-380 nm, dichroic mirror: 400 nm (LP), emission: 415-485 nm) fluorescent probes. Fluorescence of fluorescent proteins in the cells of Epon-embedded samples was observed in the TUK solution. After observation, the thin sections were washed with distilled water, dried overnight at room temperature, stained with uranyl acetate and lead citrate, and observed via scanning electron microscopy.

### In-resin CLEM of mitochondria, endoplasmic reticulum, and the Golgi apparatus in Epon embedded cells using mKate2-GGGSGL.

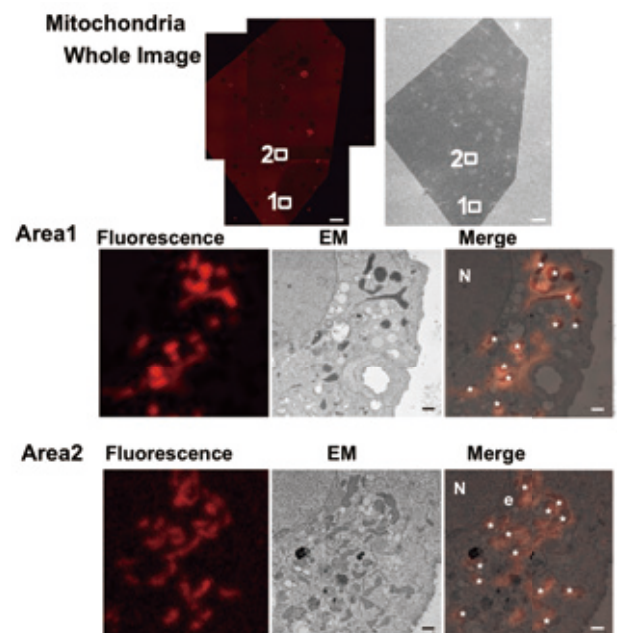
We prepared Epon-embedded samples of cells expressing mitochondria-localized mKate2-GGGSGL (FUJIFILM WAKO Chemicals, # 160-28461) [13, 18, 19], and analyzed them in thin sections using fluorescence microscopy and scanning electron microscopy. Images obtained by fluorescence microscopy show that fluorescent signals were preserved (Fig. 2). Positive signals for mitochondria in fluorescence microscopy were confirmed as mitochondria in corresponding cells via scanning electron microscopy.

**Fig. 1** Fluorescent intensities of fluorescent proteins in the cells were quantified after the fixation with paraformaldehyde and glutaraldehyde and osmification.



Cells expressing mEGFP, mWasabi, CoGFP, mEosEM, mCherry2, and mKate2 were fixed with a mixture of 2% paraformaldehyde and 2.5% glutaraldehyde at 4 °C for 1 h. Fluorescence images were obtained with a fluorescence microscope using filter sets for green (for mEGFP, mWasabi, CoGFP, and mEosEM) and red (for mCherry2 and mKate2) fluorescent probes (PFA+GA, white squares). Next, the fixed cells were treated with 1% osmium tetroxide at 4 °C for 10 min (OsO<sub>4</sub>, black squares). Fluorescence images were obtained with a fluorescence microscope under the same conditions. Fluorescent intensities of the cells (n>340 in each fluorescent protein) were evaluated using ImageJ software. (A) Relative intensity of each fluorescent protein was shown when fluorescent intensity of mEGFP after fixation with a mixture of paraformaldehyde and glutaraldehyde was regarded as 100%. (B) Relative intensity of each fluorescent protein was shown when fluorescent intensity of mEGFP after osmium-staining was regarded as 100%. Error bars indicate standard errors.

**Fig. 2** In-resin CLEM of mitochondria was performed using mKate2-mito.



The "Whole Image" indicates the whole images obtained from a confocal fluorescence microscope and from a scanning electron microscope. Scale bars, 100  $\mu$ m. The images in Areas 1 and 2 indicate a magnification of the areas (white squares 1 and 2). Scale bars, 1  $\mu$ m. The "Merge" is a merged image of the fluorescence image with an electron microscopic image (EM). "N", "e", and asterisks in the images indicate respective nucleus, endoplasmic reticulum, and mitochondria.

We next performed in-resin CLEM of the Golgi apparatus using the Golgi-localized this protein (FUJIFILM WAKO Chemicals, # 160-28621) (Fig. 3) [20-22]. Fluorescent signals were observed in thin sections via the use of fluorescence microscopy. Electron microscopic analyses revealed that fluorescent positive regions corresponded well with Golgi-cisternae and with vesicular/tubular structures.

We expressed this fluorescent protein with an ER-targeting signal at the amino terminus and an ER-retrieve KDEL signal at the carboxyl terminus in cells [23] (FUJIFILM WAKO Chemicals, # 160-28631), and performed in-resin CLEM of the ER in the Epon-embedded cells (Fig. 4). In-resin CLEM revealed that fluorescence-positive signals are representative of the membranous structures of the ER with ribosomes in the electron microscopic image. These results suggested that in-resin CLEM of Epon-embedded cells is available using this protein.

### Two-color in-resin CLEM of nucleus and mitochondria in Epon embedded cells.

We focused on two-color in-resin CLEM of Epon-embedded cells using green and far-red fluorescent proteins [14]. HeLa cells expressing histone H2B-tagged with CoGFPv0 (H2B-CoGFPv0) and mCherry2-fused with a mitochondria-targeting signal (mCherry2-mito; Addgene plasmid # 164164) were fixed, stained and embedded. After Epon-embedding, 100 nm thin sections were prepared. Analysis of the sections using a fluorescence microscope showed that the green fluorescence of H2B-CoGFPv0 was detected in the nucleus (Fig. 5) and the red fluorescence of mCherry2-mito was detected in the cytosol. Electron microscopy analyses revealed that green fluorescent signals corresponded to the nucleus while the red fluorescent signals corresponded to the mitochondria, indicating that two color in-resin CLEM of the nucleus and mitochondria was achieved.

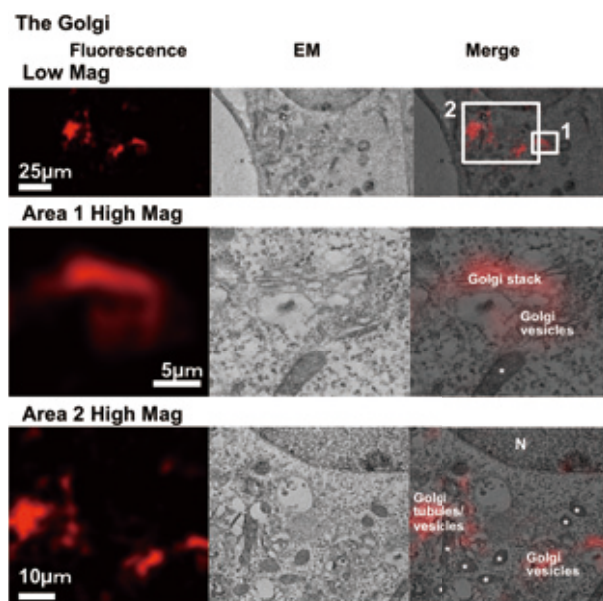
### Two-color in-resin CLEM of the nucleus and endoplasmic reticulum in Epon embedded cells.

For the localization of mCherry2 to ER, we generated an expression plasmid of mCherry2 fused with an ER-targeting sequence of calreticulin and the ER retrieval sequence, KDEL (mCherry2-ER; Addgene plasmid # 164166). H2B-CoGFPv0 and mCherry2-ER were expressed in the cells. After chemical fixation and osmium-staining, cells were embedded in the Epon resins. In 100 nm-thin sections of the Epon-embedded cells, we detected green and red fluorescence from CoGFPv0 and mCherry2 (Fig. 6). In matching electron micrographs, we determined that the red fluorescent signals corresponded to the endoplasmic reticulum and the green fluorescent signals corresponded to the nucleus.

### Two-color in-resin CLEM of mitochondria and the endoplasmic reticulum in Epon embedded cells.

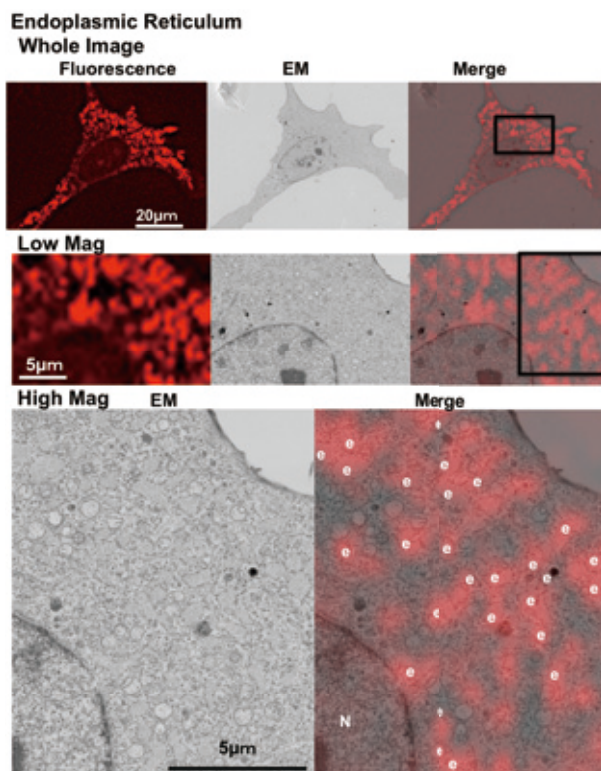
We further performed two-color in-resin CLEM of mitochondria and ER in Epon embedded cells using mWasabi fused with an ER-targeting sequence of calreticulin and the ER retrieval sequence, KDEL (mWasabi-ER; Addgene plasmid # 164165) and mCherry2-mito. Fluorescence microscopy confirmed the detection of green and red fluorescence of mWasabi-ER and mCherry2-mito, respectively (Fig. 7). Electron microscopy analyses of the same thin sections revealed that the red fluorescence from

**Fig. 3 In-resin CLEM of the Golgi apparatus was performed using mKate2-Golgi.**



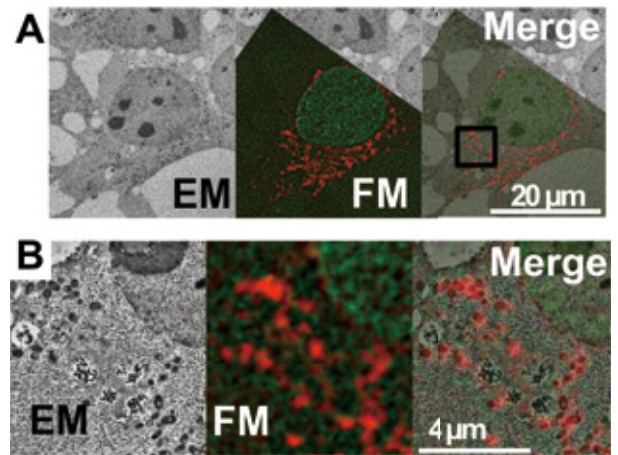
The fluorescent image was obtained using a fluorescence microscope, and the electron microscopic image was obtained using a transmission electron microscope. The "High Mag" in Areas 1 and 2 indicates a magnification of the areas surrounded by white squares 1 and 2 in the "Low Mag" areas. "N" and asterisks in the images indicate respective nucleus and mitochondria.

**Fig. 4 In-resin CLEM of the endoplasmic reticulum was performed using mKate2-ER.**



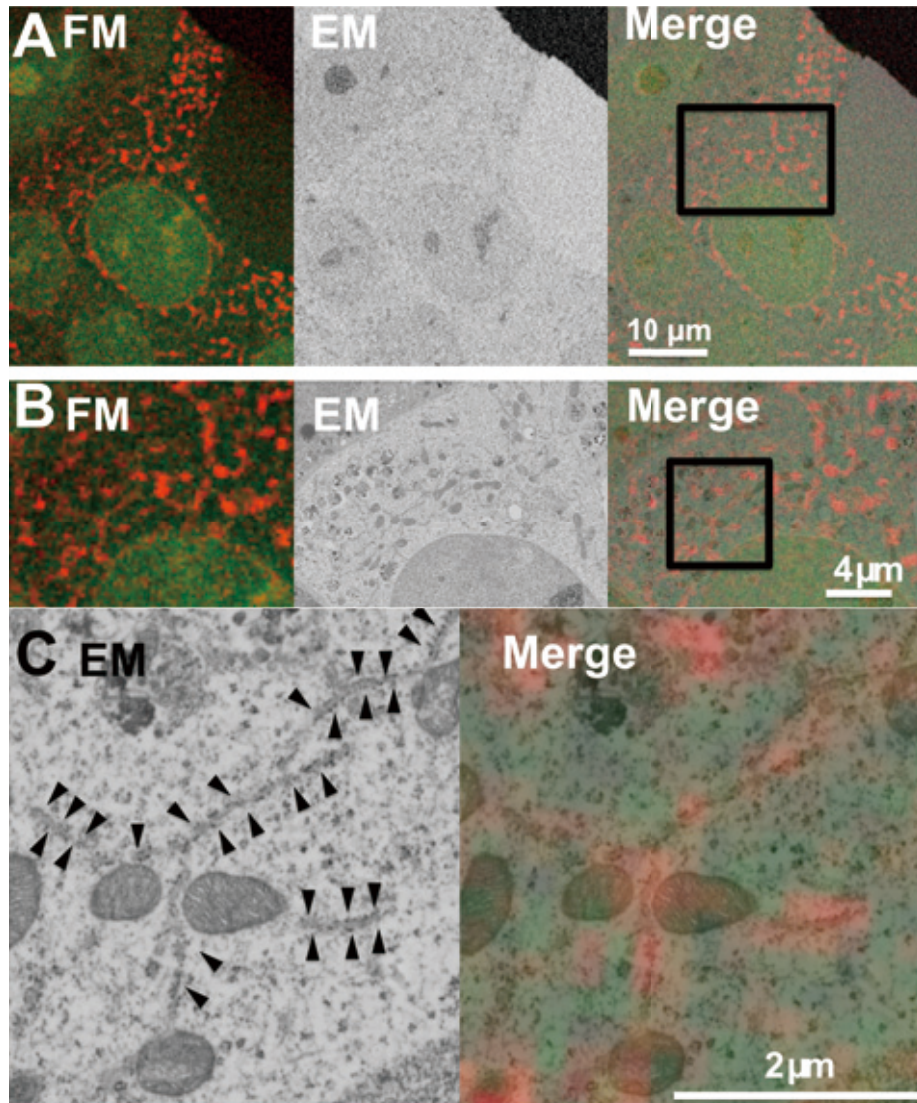
The "Whole Image" indicates the whole images obtained from a fluorescent microscopy and from a scanning electron microscopy. The "Low Mag" indicates a low-level magnification of the area surrounded by a square in the "Whole Image". The "High Mag" indicates a higher magnification of the area surrounded by a square in the "Low Mag". "N" and "e" in the images indicate respective nucleus and endoplasmic reticulum.

**Fig. 5 Two-color in-resin CLEM of the nucleus and mitochondria was performed using H2B-CoGFPv0 and mCherry2-mito.**



Thin section (100 nm) of Epon-embedded cells expressing H2B-CoGFPv0 (green pseudo color) and mCherry2-mito (red pseudo color) was prepared. Fluorescent images (**FM**) were obtained with a fluorescence microscope using filter sets for green and red fluorescent probes. Electron microscopic images (**EM**) were obtained with a scanning electron microscope, and were processed with a method called "Contrast Limited Adaptive Histogram Equalization" using ImageJ software with the plugin Enhance Local Contrast (CLAHE). The "**Merge**" is a merged image of the fluorescence image (**FM**) with an electron microscopic image (**EM**). The images in **B** indicate magnification of images corresponding to the boxed area in the Merge image in **A**.

**Fig. 6 Two-color in-resin CLEM of the nucleus and endoplasmic reticulum was performed using H2B-CoGFPv0 and mCherry2-ER.**



Thin section (100 nm) of Epon-embedded cells expressing H2B-CoGFPv0 (green pseudo color) and mCherry2-ER (red pseudo color) was prepared. The "**Merge**" is a merged image of the fluorescence image (**FM**) with the electron microscopic image (**EM**). The images in **B** and **C** indicate magnification of images corresponding to the boxed area in the Merge image in respective **A** and **B**. Arrowheads in **C** indicate red fluorescence-positive rough endoplasmic reticulum.

mCherry2-mito corresponded to the mitochondria, and green fluorescence from mWasabi-ER corresponded to the ER.

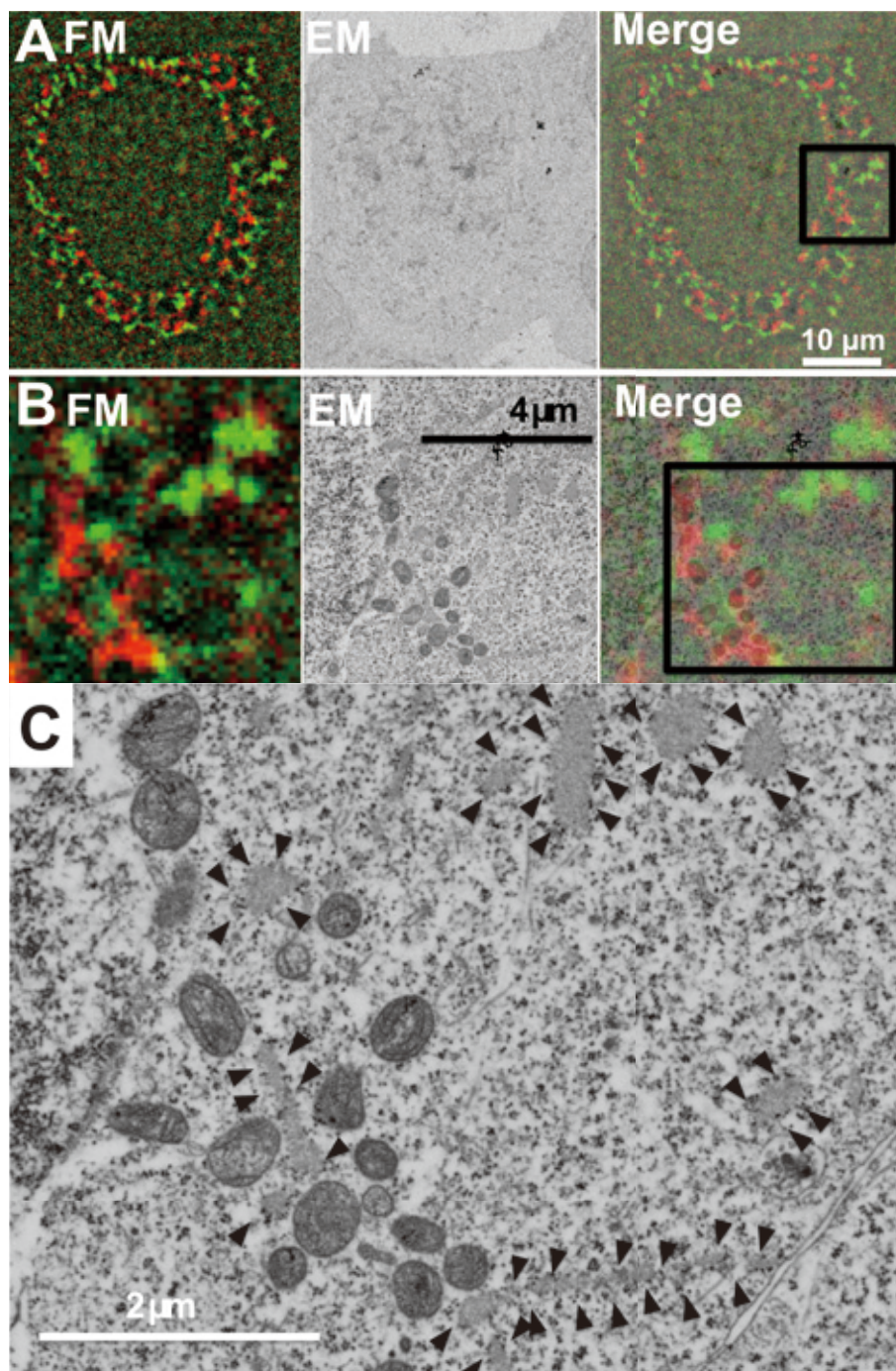
## Discussion

We discovered that two green fluorescent proteins, mWasabi and CoGFPv0, and two red fluorescent protein, mKate2-GGGSGL and mCherry2, can retain their fluorescence after osmium-staining. mWasabi and CoGFPv0 retain brighter fluorescence than mEosEM after osmium staining under our experimental conditions (Fig. 1). When the fluorescent intensities of these fluorescent proteins are compared before and after osmium-staining, these intensities of mEGFP, mEosEM, mWasabi,

CoGFPv0, mKate2, and mCherry2 decrease after osmium-staining. Considering fluorescent intensities of these fluorescent proteins and autofluorescence of 100 nm-thin sections of epoxy resins, we focused on CoGFPv0, mWasabi, mKate2-GGGSGL, and mCherry2. Using these proteins, we achieved single- and two-color in-resin CLEM of cells and organelles in 100 nm-thin sections of the Epon-embedded samples.

Interestingly, mEGFP also retains faint weak fluorescence after osmium staining, while it requires about 100-fold longer exposure than that before osmium staining (Fig. 1). It could be possible to achieve in-resin CLEM of Epon-embedded specimen using mEGFP, if the sensitivity of fluorescence microscopy is improved significantly.

**Fig. 7 Two-color in-resin CLEM of ER and mitochondria was performed using mWasabi-ER and mCherry2-mito.**



Thin section (100 nm) of Epon-embedded cells expressing mWasabi-ER (green pseudo color) and mCherry2-mito (red pseudo color) was prepared. The “Merge” images in **A** and **B** are merged images of the fluorescence image (FM) with the electron microscopic image (EM). The images in **B** indicate magnification of images corresponding to the boxed area in the Merge image in **A**. The EM images in **C** indicate magnification of image corresponding to the boxed area in the Merge image in **B**. Arrowheads in **C** indicate green fluorescence-positive rough endoplasmic reticulum.

## Conclusion

In this study, we found that two green (CoGFPv0 and mWasabi) and two far-red fluorescent proteins (mKate2-GGSGSL and mWasabi) retain their fluorescence after CLEM-processing. Interestingly, these proteins retain 3.2-44 fold brighter fluorescence than previously reported mEosEM after osmium tetroxide-staining. We demonstrated two-color in-resin CLEM of some organelles (mitochondria, the nucleus, endoplasmic reticulum, and the Golgi apparatus) using these fluorescent proteins. These results suggested that two-color in-resin CLEM of other organelles and proteins in the Epon-embedded cells will be achieved with this technique using these fluorescent proteins.

## Acknowledgments

This work is partly supported by the Project for Elucidating and Controlling Mechanisms of Aging and Longevity from the Japan Agency for Medical Research and Development (AMED JP19gm5010003 and 20gm5010003 to Y.U) and by the MEXT-supported Program for the Strategic Research Foundation at Private Universities (to Y.U). This work was also supported by grants from the Japan Society for the Promotion of Science to I.T. (JSPS KAKENHI 15K12749 and 20H05342) and J.Y. (JSPS KAKENHI 20K22744), and the Research Institute for Diseases of Old Age, Juntendo University School of Medicine to I.T. and S.K.

## References

- [ 1 ] R.E. Webster, M. Osborn, K. Weber, Visualization of the same PtK2 cytoskeletons by both immunofluorescence and low power electron microscopy, *Experimental Cell Research*, **117** (1978) 47-61.
- [ 2 ] C.H. Wouters, Techniques for combining light microscopy and scanning electron microscopy: a survey of the literature, *Journal of Microscopy*, **147** (1987) 5-14.
- [ 3 ] A.V. Agronskaia, J.A. Valentijn, L.F. van Driel, C.T. Schneijdenberg, B.M. Humbel, P.M. van Bergen en Henegouwen, A.J. Verkleij, A.J. Koster, H.C. Gerritsen, Integrated fluorescence and transmission electron microscopy, *Journal of Structural Biology*, **164** (2008) 183-189.
- [ 4 ] B.N. Giepmans, Bridging fluorescence microscopy and electron microscopy, *Histochemistry and Cell Biology*, **130** (2008) 211-217.
- [ 5 ] T. Kanemaru, K. Hirata, S. Takasu, S. Isobe, K. Mizuki, S. Mataka, K. Nakamura, A fluorescence scanning electron microscope, *Ultramicroscopy*, **109** (2009) 344-349.
- [ 6 ] M. Grabenbauer, Correlative light and electron microscopy of GFP, *Methods in Cell Biology*, **111** (2012) 117-138.
- [ 7 ] Y. Uchiyama, M. Koike, M. Shibata, M. Sasaki, Autophagic neuron death, *Methods Enzymol*, **453** (2009) 33-51.
- [ 8 ] E. Johnson, R. Kaufmann, Correlative In-Resin Super-Resolution Fluorescence and Electron Microscopy of Cultured Cells, *Methods in molecular biology (Clifton, N.J.)*, **1663** (2017) 163-177.
- [ 9 ] E. Johnson, R. Kaufmann, Preserving the photoswitching ability of standard fluorescent proteins for correlative in-resin super-resolution and electron microscopy, *Methods in Cell Biology*, **140** (2017) 49-67.
- [10] C.J. Peddie, M.C. Domart, X. Snetkov, P. O'Toole, B. Larijani, M. Way, S. Cox, L.M. Collinson, Correlative super-resolution fluorescence and electron microscopy using conventional fluorescent proteins in vacuo, *Journal of Structural Biology*, **199** (2017) 120-131.
- [11] M.G. Paez-Segala, M.G. Sun, G. Shtengel, S. Viswanathan, M.A. Baird, J.J. Macklin, R. Patel, J.R. Allen, E.S. Howe, G. Piszczek, H.F. Hess, M.W. Davidson, Y. Wang, L.L. Looger, Fixation-resistant photoactivatable fluorescent proteins for CLEM, *Nature Methods*, **12** (2015) 215-218.
- [12] Z. Fu, D. Peng, M. Zhang, F. Xue, R. Zhang, W. He, T. Xu, P. Xu, mEosEM withstands osmium staining and Epon embedding for super-resolution CLEM, *Nature Methods*, **17** (2020) 55-58.
- [13] I. Tanida, S. Kakuta, J.A. Oliva Trejo, Y. Uchiyama, Visualization of cytoplasmic organelles via in-resin CLEM using an osmium-resistant far-red protein, *Scientific Reports*, **10** (2020) 11314.
- [14] I. Tanida, Y. Furuta, J. Yamaguchi, S. Kakuta, J.A. Oliva Trejo, Y. Uchiyama, Two-color in-resin CLEM of Epon-embedded cells using osmium resistant green and red fluorescent proteins, *Scientific Reports*, **10** (2020) 21871.
- [15] D.A. Zacharias, J.D. Violin, A.C. Newton, R.Y. Tsien, Partitioning of lipid-modified monomeric GFPs into membrane microdomains of live cells, *Science*, **296** (2002) 913-916.
- [16] H.W. Ai, S.G. Olenych, P. Wong, M.W. Davidson, R.E. Campbell, Hue-shifted monomeric variants of Clavularia cyan fluorescent protein: identification of the molecular determinants of color and applications in fluorescence imaging, *BMC Biology*, **6** (2008) 13.
- [17] K. Ogoh, T. Kinebuchi, M. Murai, T. Takahashi, Y. Ohmiya, H. Suzuki, Dual-color-emitting green fluorescent protein from the sea cactus *Cavernularia obesa* and its use as a pH indicator for fluorescence microscopy, *Luminescence*, **28** (2013) 582-591.
- [18] G. Guntas, R.A. Hallett, S.P. Zimmerman, T. Williams, H. Yumerefendi, J.E. Bear, B. Kuhlman, Engineering an improved light-induced dimer (iLID) for controlling the localization and activity of signaling proteins, *Proceedings of the National Academy of Sciences of the United States of America*, **112** (2015) 112-117.
- [19] E. Tanida-Miyake, M. Koike, Y. Uchiyama, I. Tanida, Optimization of mNeonGreen for *Homo sapiens* increases its fluorescent intensity in mammalian cells, *PloS One*, **13** (2018) e0191108.
- [20] J. Llopis, J.M. McCaffery, A. Miyawaki, M.G. Farquhar, R.Y. Tsien, Measurement of cytosolic, mitochondrial, and Golgi pH in single living cells with green fluorescent proteins, *Proceedings of the National Academy of Sciences of the United States of America*, **95** (1998) 6803-6808.
- [21] N. Yamaguchi, M.N. Fukuda, Golgi retention mechanism of beta-1,4-galactosyltransferase. Membrane-spanning domain-dependent homodimerization and association with alpha- and beta-tubulins, *The Journal of Biological Chemistry*, **270** (1995) 12170-12176.
- [22] P.A. Gleeson, R.D. Teasdale, J. Burke, Targeting of proteins to the Golgi apparatus, *Glycoconjugate Journal*, **11** (1994) 381-394.
- [23] L. Fliegel, K. Burns, D.H. MacLennan, R.A. Reithmeier, M. Michalak, Molecular cloning of the high affinity calcium-binding protein (calreticulin) of skeletal muscle sarcoplasmic reticulum, *The Journal of Biological Chemistry*, **264** (1989) 21522-21528.

# Degradation Analysis for Polymer Materials by Spin-Trapping

Wataru Sakai Faculty of Materials Science and Engineering, Kyoto Institute of Technology

Although polymer materials are familiar to us, the detailed mechanisms of their degradation reactions are still unclear. Therefore, much of the knowledge about the radical species of reaction intermediates has been obtained by analysing the products after degradation. To address this problem, the author focused on using the spin-trapping method to observe short-lived radical species, which is an application of electron spin resonance (ESR), and attempted to detect the ESR of short-lived radical species produced in the degradation process of polymer materials. As a result, the molecular structures could be assigned, and the thermal degradation scheme of a relatively early stage could be clarified, which has not been confirmed thus far. In this study, the author briefly introduces the actual flow used to analyse the degradation of polymer materials by the spin-trapping method and shows an example of the analysis result.

## Introduction

Polymer materials were previously made of natural materials, such as silk, cotton, animal hair, wood, and leather. Since the 19th century, polymer materials have been artificially produced in industry. However, the basic concept that polymers are “macromolecules”, large molecules composed of thousands of covalent bonds, was first proposed by H. Staudinger, a German chemist, in 1920, almost 100 years ago [1]. Since then, polymer science has made remarkable progress not only academically but also industrially from the viewpoint of both chemistry and physics. Polymer materials have excellent moulding processability, colourability, transparency, and high specific strength and can be functionally enhanced with various chemical reactions. Therefore, polymer materials have been widely used together with metals and ceramics as one of the three major industrial materials. However, because polymer materials are made of organic compounds, “degradation” which the original performance and function are lost is likely to occur. The molecular structures are easily destroyed by various energy stimuli, such as heat, light, and mechanical stress, and by the presence of oxygen, which causes an autoxidation chain reaction (Fig. 1). The analytical methods used to study the degradation mechanism of polymer materials generally include molecular weight analysis by gel permeation chromatography (GPC) and gas chromatography mass spectrometry (GC-MS), spectral analysis by Fourier transform infrared spectroscopy (FT-IR) and nuclear magnetic resonance (NMR), and thermal analysis, such as differential scanning calorimetry (DSC) and thermogravimetric analysis (TGA). However, since these methods cannot observe short-lived reaction intermediates, the degradation mechanism reported has been inductively derived by product analysis after degradation.

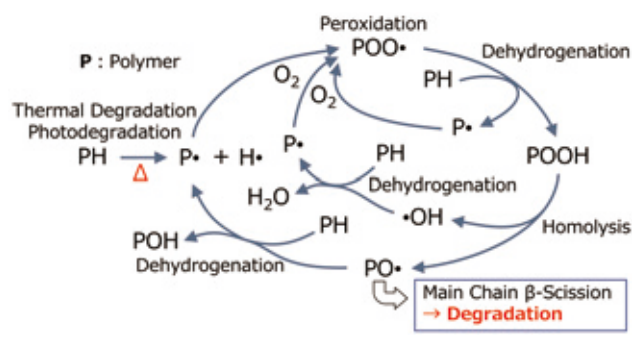
Electron spin resonance (ESR) is the only analytical method that can identify the molecular structure of radical species. After the first successful ESR observation of radical species by Zavoisky, a Soviet physicist, in 1945 [2], chemical studies with ESR were “explosively” performed in the 1960s [3]. It was also around that time when ESR began to demonstrate that the degradation of

polymer materials occurs via radical reactions. However, radical species generally have a lifetime of less than a millisecond and cannot be detected by normal continuous wave ESR equipment. Therefore, researchers have conducted degradation studies by the matrix isolation method and the freezing method as well as the flow-injection method and time-resolved ESR. However, in many cases, complicated systems are required, or the degradation conditions are different from the actual conditions.

From the above background, the radical species produced during the degradation reaction of most polymer materials have not been fully elucidated, even now. Although it is known that some of the degradation inhibitors added to polymer materials effectively suppress radical reactions, they have been empirically added in the same way that humans are symptomatically prescribed cold remedies to suppress symptoms. Therefore, if radical species produced during the degradation of polymer materials can be detected, the reaction mechanism can be understood in more detail, and causal treatments to more effectively prevent degradation become possible.

With the background described above, the author focused on the “spin-trapping method”, which is an application method of ESR,

Fig.1 Schematic diagram of the autoxidation degradation mechanism of polymer materials.



to detect and identify the short-lived radical species produced during the degradation reaction process of polymer materials. Consequently, the early stage of the thermal degradation can be clarified thus far; for poly(butylene terephthalate) (PBT) [4], thermoplastic elastomer of PBT copolymer [5], and poly(vinyl alcohol) [6].

## ESR and Spin-Trapping Method

### Principle of ESR and the Hyperfine Structure

(As a number of good books have been published about the basics of ESR, please refer to them to study in detail.) The radical species produced by the degradation of polymer materials is a molecule that has an unpaired electron. The unpaired electron has a magnetic dipole moment due to its own spin. When an external magnetic field is applied to the radical species in the polymer, the unpaired electrons are classified as two types due to the Zeeman effect: energetically stable  $\beta$ -spins and unstable  $\alpha$ -spins (Fig. 2(a)). When an electromagnetic wave with the same energy as Zeeman splitting is applied to the system, the  $\beta$  spin translates to the  $\alpha$  spin through resonance. To observe this ESR, it is necessary to satisfy the ESR equation:  $h\nu = g\mu_B H_0$ . Common ESR equipment uses an external magnetic field of approximately 0.3 T and a microwave frequency of approximately 9 GHz. Here,  $h$  is Planck's constant,  $\nu$  is the microwave frequency,  $\mu_B$  is the Bohr magneton,  $H_0$  is the external magnetic field, and the proportional constant is called

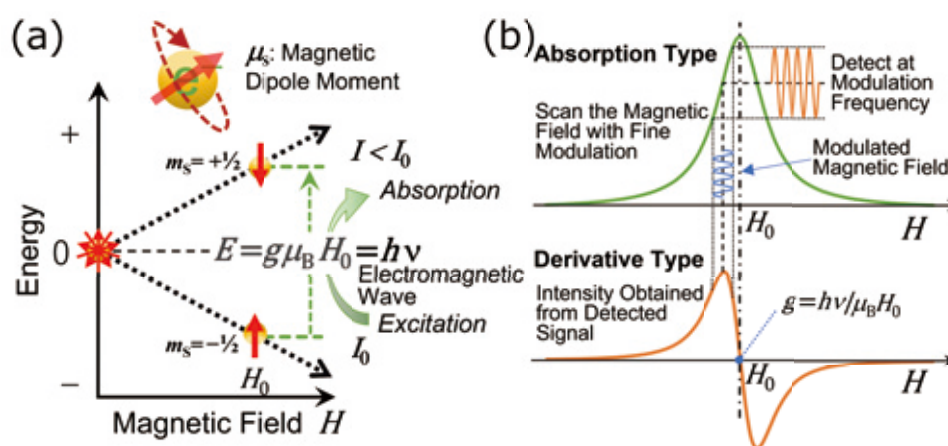
the  $g$  value. In the actual measurement, while the microwave frequency is fixed, the magnetic field is swept with a small modulation at a high frequency, normally at 100 kHz, to increase the detection sensitivity. Because the component with the same frequency is extracted as a signal, the ESR spectrum appears to be a somewhat complicated derivative-type curve.

If there is a nucleus with a nonzero nuclear spin number near the unpaired electron (e.g.,  $^1\text{H}$  ( $I = 1/2$ ),  $\text{D}$  ( $^2\text{H}$ ) ( $I = 1$ ),  $^{13}\text{C}$  ( $I = 1/2$ ),  $^{14}\text{N}$  ( $I = 1$ ), and  $^{19}\text{F}$  ( $I = 1/2$ )), the Zeeman split becomes complicated by the influence of its nuclear magnetic moment, and as a result, an ESR spectrum with multiple peaks is observed. This structure is called the hyperfine structure (*hfs*). By analysing the hyperfine coupling constant (*hfcc*) between the peaks, the molecular structure near the unpaired electron can be deduced (Fig. 3). The  $g$  value calculated from the centre position of the spectrum using the ESR equation (Fig. 2(b)) is a unique value that reflects the difference between the environments surrounding unpaired electrons and is also used to identify the radical species.

### Spin-trapping Method

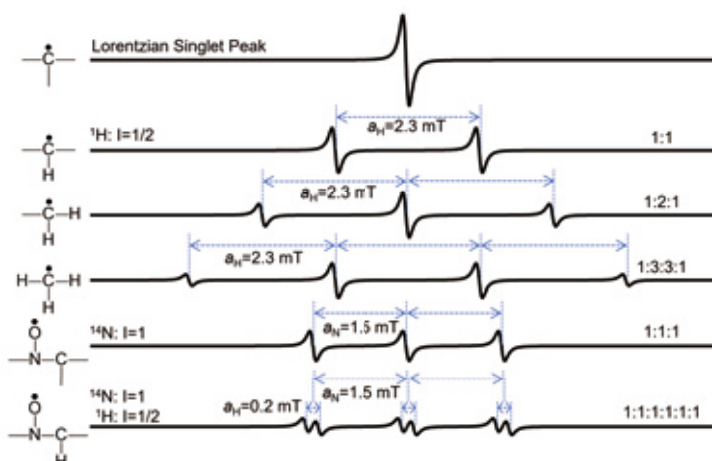
The spin-trapping method was first proposed by Janzen in 1968 [7]. The spin-trapping reagent added in advance to the reaction system becomes a "spin adduct" of nitroxide-type radicals when it traps a radical intermediate (Fig. 4). Since the spin adduct has a long lifetime, it can be observed with normal continuous wave ESR equipment and shows unique *hfs* that reflects the molecular structure of the original radical species. In recent years, the spin-

Fig. 2



(a) Schematic diagram of the basic principle of the electron spin and the ESR and (b) absorption-type and derivative-type spectra of the ESR.

Fig. 3 Some examples of ESR spectra of the various radical species with different hyperfine structures (*hfs*).



The constant  $a$  is the hyperfine coupling constant (*hfcc*). When  $n$  nuclei with nuclear spin number  $I$  interact evenly with the unpaired electron, their *hfs* splits into  $2nI+1$ . The intensity ratios of those peaks are the so-called binomial coefficient (Pascal's triangle).

trapping method has been widely used in fields such as medicine, pharmaceuticals, and engineering, especially for low-molecular-weight free radicals and reactive oxygen species in solution systems. However, there have not been many research examples applied to the degradation of polymer materials [8].

Spin-trapping reagents are mainly classified into two types: the nitroso-type and nitrone-type. These are selected according to the purpose of the experiment (Fig. 5). Nitroso-types are usually unstable to light and heat, and their spin adducts are also relatively unstable. However, since the addition position of the original radical species is closer to the unpaired electron than in the nitrone-type, a *hfs* is more likely to appear in the ESR spectrum, and the structure of the original radical species is easier to distinguish. On the other hand, nitrone-types show a simpler *hfs*, from which it is more difficult to distinguish the original radical species than the nitroso-types; however, most nitrone-types are stable to light and heat. Since nitrone-type reagents easily capture oxygen-centred radicals, they are often used for radical analysis of reactive oxygen species such as  $\bullet\text{OH}$ , and most of them are water soluble.

## Degradation Analysis of Polymer Materials by the Spin-Trapping Method

### Addition of the Spin-Trapping Reagent to the Polymer Materials

To add a spin-trapping reagent to a polymer material in advance, the solvent casting method or the swelling method under temperature conditions that do not degrade the polymer is used. If the added concentration is too high, the spin-trapping reagents will react with each other, and if it is too low, the polymer radicals cannot be captured. Therefore, we need to decide the concentration by trial and error. In addition, in the case of engineering plastics with extremely low solubility, impregnation using supercritical carbon dioxide ( $\text{scCO}_2$ ) may be effective. We have confirmed the effectiveness of applying  $\text{scCO}_2$  treatment to polypropylene fibres. When using spin-trapping reagents that are sensitive to light, sample preparation must proceed in the dark or under red light illumination without UV and blue light. If the effect of dissolved oxygen has to be eliminated, the sample must be prepared in a nitrogen-substituted glove box.

### ESR Measurement Procedure used for the Spin-Trapping Method

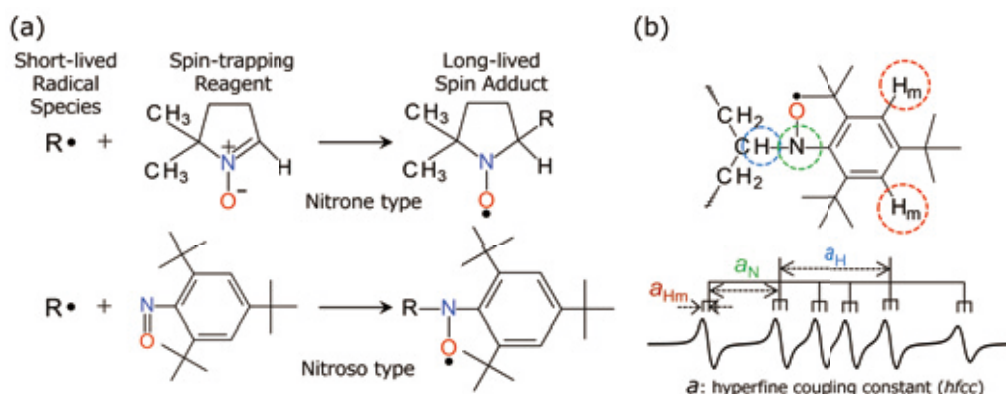
The procedure is basically the same as the procedure used for normal ESR measurement, and a polymer material with a spin-trapping reagent is inserted into a sample tube made of synthetic

quartz with an outer diameter  $\phi$  of 5 mm. Nitrogen substitution is necessary to suppress the oxidative degradation of the sample, but conversely, the oxidative degradation can be observed by purging air or oxygen. A temperature controller is used to measure the thermal degradation, and the temperature is kept constant during the measurement of one ESR spectrum. Since the state of the sample changes slightly as the temperature rises, it is necessary to readjust the Q-dip of the ESR equipment as appropriate. Elapsed time is also an important factor in the thermal degradation, and more detailed knowledge may be obtained by repeating measurements at a constant temperature. In the case of the photodegradation, the ESR measurement is performed while irradiating with light directly from an external light source through the round hole on the front side of the resonator.

### ESR Spectrum Simulation Analysis

To determine the molecular structure of the reaction intermediate, it is first necessary to separate the observed ESR spectrum into components for each spin adduct. Furthermore, the *hfs* indicated by each component spectrum should be isolated for each peak, and the molecular structure of the spin adduct can be identified by analysing their *hfcc* and intensity ratios. Finally, the molecular structure of the trapped intermediate radical species is clarified. In this study, this series of analyses is inductively performed by computer simulation, as described below. First, consider various radical species that can be generated from the molecular structure of the polymer material to be investigated and assume various spin adducts that will be produced when the radicals are captured by a spin-trapping reagent. Next, referring to research papers on similar radical compounds and the data obtained thus far by us, the number of peaks, the *hfcc*, and the intensity of each peak in the component spectrum shown by one spin adduct are assumed. Then, one ESR spectrum is plotted with all the peaks using the basic functions shown below, and this is repeated for all possible spin adducts. One absorption peak based on one ESR transition can be simulated by a Lorentzian function for a homogeneous system or a Gaussian function for a heterogeneous system depending on the environment surrounding the unpaired electron. The intensity  $I(H)$  with magnetic field  $H$  can be derived by the following equations. Here,  $\Delta H_{pp}$  is the magnetic width between the upper and lower peaks,  $H_0$  is the resonance central magnetic field, and  $S$  of the integrated intensity is an area proportional to the observed radical amount. In actual analysis work, these two equations may be linearly combined to adjust the spectral curves. Referring to the reported data on the *hfcc* of spin adducts, the data list compiled by Buettner [9] and

**Fig. 4 Scheme of the spin-trapping method**



(a) nitrone-type and nitroso-type spin-trapping reactions and (b) examples showing a spin adduct using TBNB that was derived from the secondary carbon radical and the ESR spectrum of the spin adduct.

Forrester [10] and the online database by National Institute of Environmental Health Sciences (NIEHS) [11] are very useful.

$$I'(H) = \frac{8\sqrt{3} S}{\pi \Delta H_{pp}^2} \cdot \frac{[(H_0 - H)/(\Delta H_{pp}/2)]}{\left\{3 + [(H_0 - H)/(\Delta H_{pp}/2)]^2\right\}^2} \quad (\text{Lorentzian})$$

$$I'(H) = \frac{4 S}{\sqrt{2\pi} \Delta H_{pp}^2} \cdot \left(\frac{H_0 - H}{\Delta H_{pp}/2}\right) \exp\left[-\frac{1}{2}\left(\frac{H_0 - H}{\Delta H_{pp}/2}\right)^2\right] \quad (\text{Gaussian})$$

Next, the calculated component spectra of each spin adduct are added to form one ESR spectrum while considering the relative intensities of the components, and the spectrum is compared with the measured spectrum. Then, if there is a difference, reconsider not only all the simulation parameters but also the type of spin adduct and patiently repeat the above simulation work until the difference is as small as possible. In the case of polymer materials, because the molecular motion of radical species is usually suppressed, the asymmetry of the spectrum is indeed observed due to the effect of anisotropy. Therefore, to accurately simulate the details of the spectrum, fine adjustment of all parameters for each peak is essential, and we use general spreadsheet software instead of ready-made special software to perform the series of analyses above. In fact, this simulation analysis is a kind of many-body problem, and nearly 150 peaks are sometimes analysed simultaneously, which is a persevering task that requires considerable time and effort. Is it possible to create analysis software that can use AI to automatically fit based on reported spin-trapping data?

## Example of Degradation Analysis by the Spin-Trapping Method

### Analysis of the Thermal Degradation of PVA

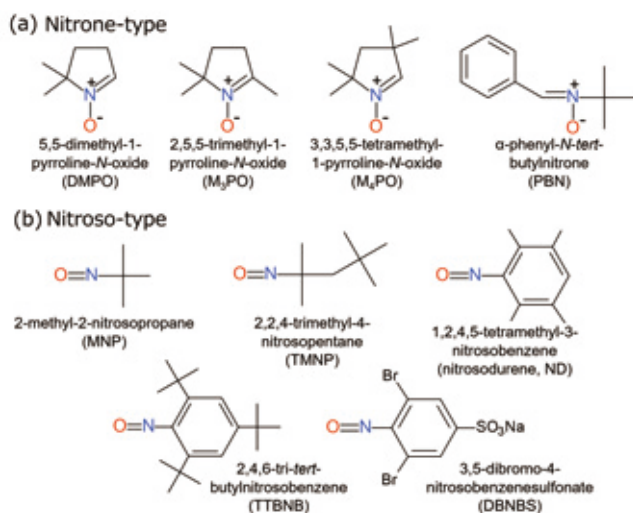
As mentioned above, we investigated the thermal degradation process of some polymer materials using the spin-trapping method [4-6]. In this article, we introduce some of the results for poly(vinyl alcohol) (PVA) [6]. PVA is a polymer with excellent

film-forming and adhesive properties and is widely used as a raw material for synthetic fibres and films. Since PVA is water soluble, DMPO was selected as a spin-trapping reagent, and a PVA/DMPO film sample was prepared by a solvent casting method. The concentration of DMPO was adjusted to 3 wt%. **Fig. 6** shows each spectrum taken by an ESR spectrometer (JEOL JES-TE300) while heating the PVA/DMPO sample stepwise using a temperature controller (JEOL DVT3). As the temperature increased, an ESR spectrum dominated by the six lines indicated by ▲ was obtained. The same measurement was performed for neat PVA without DMPO, but no ESR signal was obtained. Therefore, the ESR spectrum observed for PVA/DMPO indicated that the short-lived radical intermediates were generated by the thermal degradation of PVA and trapped by DMPO, resulting in long-lived spin adducts. In addition to the six lines, small peaks and shoulders were also observed, which indicated that several types of spin adducts were mixed.

**Fig. 7** shows the results of the simulation analysis for the spectrum obtained at 160 °C. After dozens of trials, we finally concluded that the observed spectrum consisted of five spin adduct components,  $S_1 \sim S_5$ . Some reference parts of spectral components are indicated by \*, \*\*, and \*\*\*. **Table 1** lists the structures and *hfcc* of the trapped radical intermediate species, along with data from the references used for assignment. The reasons for the assignment are as follows.

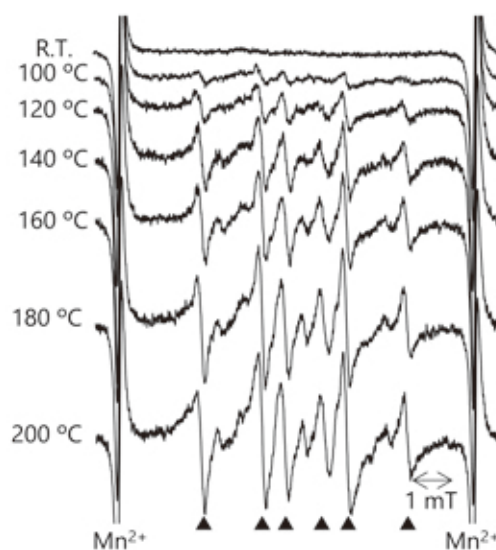
The *hfcc* of  $S_1$  was consistent with the parameter of the DMPO spin adduct from •OH produced in the Fenton reaction by Fe and H<sub>2</sub>O<sub>2</sub> in *tert*-butanol [12]. However, since the bond-dissociation energy of the C–OH bond is approximately 5 ~15 kJ/mol higher than that of other bonds [13], it is unlikely that •OH is generated by homolysis from the PVA main chain. On the other hand, there is a report that the thermal degradation of PVA causes a nonradical dehydration reaction via an intramolecular four-membered ring to produce a main chain allyl alcohol (–CH=CH–CH(OH)–CH<sub>2</sub>–) [14]. Since the dissociation energy of the C–OH bond in this structure is approximately 50 kJ/mol lower than that before dehydration [13], this structure can be a source of •OH derived by homolysis.  $S_2$  was assigned to a spin adduct derived from the PVA main chain –CH<sub>2</sub>•CH–

**Fig. 5 Examples of typical spin-trapping reagents**



(a) nitron-types and (b) nitroso-types.

**Fig. 6**



ESR spectra of PVA/DMPO in stepwise heating using an ESR spectrometer (JEOL JES-TE300) and a temperature controller (JEOL DVT3) [6].

CH<sub>2</sub>- since the *hfcc* of S<sub>2</sub> was very close to that derived from the alkyl radical CH<sub>3</sub>-•CH-CH<sub>3</sub> [15]. This intermediate can be a counterradical of •OH. S<sub>3</sub> is characterized by the fact that the *hfcc* of the N atom was slightly smaller than usual. Generally, the spin adduct of DMPO derived from alkyl radicals shows an α<sub>N</sub> of approximately 1.6 mT in aqueous solution; however, there are reports that α<sub>N</sub> decreases in carbon radicals with OH groups [16, 17]. In this study, S<sub>3</sub> was identified as a spin adduct derived from •CH(OH)-CH<sub>2</sub>- based on the difference in the solvation effect by PVA and on the results of verification experiments performed using another trapping reagent, DNBNS. S<sub>4</sub>, which is the most dominant in the observed spectrum, is known as a spin adduct derived from the radical species generated by the thermal decomposition of DMPO itself [18] and not a component due to the thermal degradation of PVA. S<sub>5</sub>, which showed three lines, could not be a DMPO spin adduct because it should show at least six lines of *hfs* by one N and one H in the DMPO structure. Chen et al., who observed the same three lines, considered

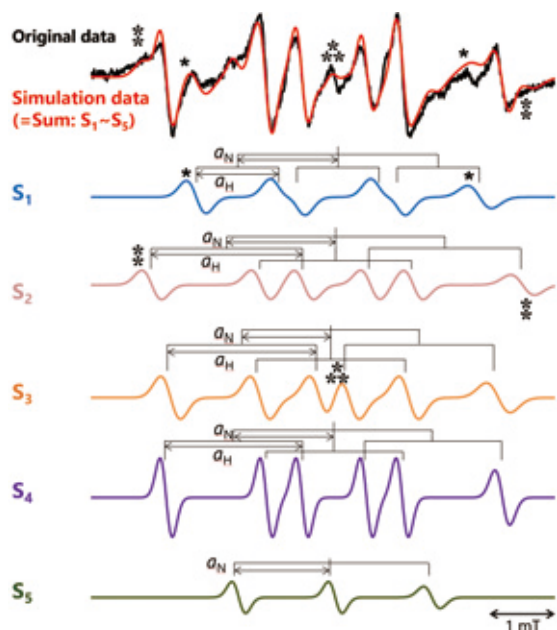
it an unknown component caused by a secondary reaction between spin adducts [19]. Since the amount of S<sub>5</sub> produced here was the smallest among the five components and did not increase, even when the temperature was raised, S<sub>5</sub> was also assigned to a component unrelated to the thermal degradation of PVA. Regarding S<sub>1</sub>, there was a possibility that H<sub>2</sub>O mixed in hydrophilic PVA may be a source of •OH radical. To confirm this possibility, two solution samples containing H<sub>2</sub>O or PVA with the same number of OH groups were prepared using another trapping reagent, DNBNS, and the solvent DMSO, and the amounts of spin adducts derived from •OH were compared. As a result, the amount produced in the H<sub>2</sub>O sample was much smaller than that produced in the PVA sample. Therefore, we could conclude that •OH originates from the PVA main chain.

From the ESR spectrum obtained at each temperature, the relative amount of radical spin adduct was calculated by double integration for S<sub>1</sub>~S<sub>3</sub> and is shown in Fig. 8. The amount of every component increased with increasing temperature, but the amount of S<sub>1</sub> and S<sub>2</sub> increased more slowly above 160 °C, while that of the main chain scission radical S<sub>3</sub> showed a faster tendency to increase. From DSC measurement, the melting behaviour of crystalline part of PVA was observed between ca. 170 °C and 200 °C. Therefore, the molecular motion of PVA was activated and main chain scission was actively promoted in the region above 160 °C.

In addition, the change in the molecular weight distribution of neat PVA heated for 10 h was investigated by GPC measurement. When heated at 100 °C and 150 °C, the distribution of the higher-molecular weight part increased slightly, which indicated that the PVA molecules were crosslinked. However, when heated at 200 °C, most of the PVA sample showed gelation with the GPC solvent, and the molecular weight distribution of the dissolved part largely shifted to a lower molecular weight. These results indicate that random decomposition of the main chain competitively proceeds at the same time as crosslinking when PVA is heated.

Comprehensively considering the analysis results based on the spin-trapping method, the •OH radical that dissociated from the side chain of the main chain type allyl alcohol is an important active species in the thermal degradation reaction of PVA. At 160 °C or lower, hydrogen is absorbed from the main chain to produce polymer radicals (-CH<sub>2</sub>-•CH-CH<sub>2</sub>- and -CH<sub>2</sub>-•C(OH)-CH<sub>2</sub>-), which cause intermolecular crosslinking. Above 160 °C, as crosslinking progresses, β-scission of the main chain polymer radicals proceeds at the same time, which reduces the molecular

Fig. 7



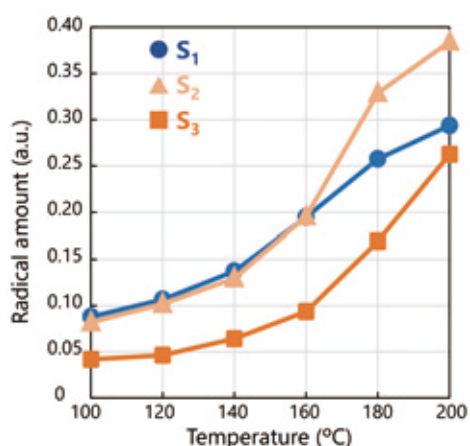
Results of simulation analysis for the ESR spectrum of PVA/DMPO at 160 °C [6].

Table 1

	Trapped Radical	<i>hfcc</i> /mT		<i>g</i>	Trapped Radical (ref)	<i>hfcc</i> /mT (ref)		<i>g</i> (ref)	Investigated Materials/solvent (ref)
		<i>a<sub>N</sub></i>	<i>a<sub>H</sub></i>			<i>a<sub>N</sub></i>	<i>a<sub>H</sub></i>		
S <sub>1</sub>	•OH	1.52	1.25	2.0052	•OH	1.46	1.20	N.A.	H <sub>2</sub> O <sub>2</sub> /t-butanol
S <sub>2</sub>	-CH=CH-•CH-CH <sub>2</sub> -	1.65	2.30	2.0052	CH <sub>3</sub> -•CH-CH <sub>3</sub>	1.61	2.44	N.A.	Iproniazid/Water
S <sub>3</sub>	•CH(OH)-CH <sub>2</sub> -	1.35	2.25	2.0055	•CH(OH)-CH <sub>3</sub>	1.57	2.24	N.A.	Fe, cysteine, ethanol/Water
	-CH <sub>2</sub> -•C(OH)-CH <sub>2</sub> -				CH <sub>3</sub> -•C(OH)-CH <sub>3</sub>	1.52	2.28	N.A.	
S <sub>4</sub>	DMPO degradation	1.51	2.05	2.0055	DMPO degradation	1.53	2.20	N.A.	Xanthin/Water
S <sub>5</sub>	DMPO-X	1.46	-	2.0054	DMPO-X	1.45	-	2.0050	PEO/Water

Molecular structure of the trapped radical species produced through PVA degradation, the *hfcc* and *g*-value of spin adducts, and data in references [6].

Fig. 8



The change in the relative amounts of radicals for spin adducts  $S_1$ – $S_3$ , as produced by PVA/DMPO upon stepwise heating from 100 to 200 °C [6].

weight. Therefore, the addition of an antidegradation agent that quenches the  $\bullet\text{OH}$  generated in the system may be a causal treatment that can suppress the thermal degradation of PVA.

The above is an example of the degradation of polymer materials analysed by the spin-trapping method. However, because of the space limitations of this article, many parts of the paper have been omitted, so some explanations are lacking. In fact, it is very important to use analytical methods other than ESR in combination to elucidate the reaction pathway. If you are interested, I would appreciate it if you could refer to our papers.

## Summary

Generally, most of the analyses of the thermal degradation of polymer materials focus on the temperature range near the melting point or higher, and there are few reports on reactions that occur at relatively low temperatures, as in our study. However, observation by the spin-trapping method using ESR, which is a very sensitive analysis method, can clarify the initial reaction process of the degradation of polymer materials, which has not been investigated well until now. Currently, we are conducting research on mechanical and photodegradation in addition to the thermal degradation. For example, it may be possible to analyse fatigue fractures as perceived by the long-term accumulation of minute changes. Recently, despite the growing interest in the durability and longevity of polymer materials, academic research in this field does not seem to be very active. However, on the other hand, I have often been consulted by companies about basic or specialized knowledge of the degradation or lifetime of polymer materials. I feel that the specific and detailed knowledge required by the industry is still lacking. I would like to continue to patiently study degradation to acquire more scientific knowledge that enables causal treatment measures to protect against degradation and control the lifetime of polymer materials.

## Acknowledgements

First, I would like to express my sincere appreciation to Professor Masahide Yamamoto (Professor Emeritus of Kyoto University) and Professor Jun Yamauchi (Professor Emeritus of Kyoto University), who gave me valuable knowledge and advice on the ESR study of polymer degradation from my student days.

I wish to express my sincere gratitude to Professor Kunihiko Tajima (Professor of Kyoto Institute of Technology), Professor Akira Nakajima (Professor of Miyazaki University), Professor Masahiro Kono (Professor of Tokyo Institute of Technology) and Professor Masayoshi Tabata (Visiting Professor of Chitose Institute of Science and Technology) for their great comments and advice on the ESR results by the spin-trapping method. The work on PVA introduced in this article [6] was financially supported by Kuraray Co., Ltd. I would like to acknowledge the staff at JEOL RESONANCE Inc., including Ms. Yumi Nakai, Mr. Masahito Okano, Dr. Aiko Shimada, Mr. Koichi Okuzumi, and the staff at JEOL Ltd., including Dr. Yukio Mizuta, and many others, for their kind advice and cooperation regarding ESR equipment. I wish to express my special thanks to the late Dr. Norio Manabe, who was first interested in our spin-trapping study and strongly encouraged me to proceed with this study. In fact, the experimental results are the fruits of the efforts of many students in my laboratory, and I would like to express my sincere gratitude to all of them, as well as Professor Naoto Tsutsumi and Associate Professor Kenji Kinashi for their kind help.

## References

- [ 1 ] Staudinger H. *Ber. Dtsch. Chem. Ges.* **53**(6), 1073–1085 (1920).
- [ 2 ] Zavoisky E. *J. Phys. (USSR)* **9**, 211–216 (1945).
- [ 3 ] Ohya H.; Yamauchi J. *Electron Spin Resonance, Micro-Characterization of Materials*, Kodansha (1989) [in Japanese].
- [ 4 ] Sono, M.; Kinashi, K.; Sakai, W.; Tsutsumi, N. *Macromolecules* **50**(1), 254–263 (2017).
- [ 5 ] Sono, M.; Kinashi, K.; Sakai, W.; Tsutsumi, N. *Macromolecules* **51**(3), 1088–1099 (2018).
- [ 6 ] Hayashi T.; Kinashi K.; Sakai W.; Tsutsumi N; Fujii A.; Inada S.; Yamamoto H. *Polymer* **217**, 123416. (2021) Figures and Table are reprinted from this paper, Copyright(2021), with permission from Elsevier.
- [ 7 ] Janzen E. G.; Blackburn B. J. *J. Am. Chem. Soc.* **90**, 5909–5910 (1968).
- [ 8 ] Schlick S. *Advanced ESR Methods in Polymer Research*, Wiley (2006).
- [ 9 ] Buettner, G. R. *Free Radic. Biol. Med.* **3**(4), 259–303 (1987).
- [ 10 ] Forrester, A. R. *Nitroxide Radicals/Nitroxid-Radikale (Landolt-Börnstein: Numerical Data and Functional Relationships in Science and Technology - New Series (17d1&d2))*, Springer-Verlag, (1989).
- [ 11 ] Spin Trap Database, National Institute of Environmental Health Sciences, <https://tools.niehs.nih.gov/stdb/index.cfm>
- [ 12 ] Kalyanaraman, B.; Mottley, C.; Mason, R. P. *J. Biochem. Biophys. Methods* **9**, 27–31 (1984).
- [ 13 ] Yu-Ran, L. *Handbook of Bond Dissociation Energies in Organic Compounds*, CRC press, (2002).
- [ 14 ] Holland, B. J.; Hay, J. N. *Polymer* **42**(16), 6775–6783 (2001).
- [ 15 ] Kalyanaraman, B.; Sinha, B. K. *Environ. Health Perspect.* **64**, 179–184 (1985).
- [ 16 ] Kirino, Y.; Ohkuma, T.; Kwan, T. *Chem. Pharm. Bull.* **29**(1), 29–34 (1981).
- [ 17 ] Searle, A. J. F.; Tomasi, A. *J. Inorg. Biochem.* **17**(2), 161–166 (1982).
- [ 18 ] Finkelstein, E.; Rosen, G. M.; Rauckman, E. J.; Paxton, J. *Mol. Pharmacol* **16**(2), 676–685 (1979).
- [ 19 ] Chen, L.; Kutsuna, S.; Yamane, S.; Mizukado, J. *Polym. Degrad. Stab.* **139**, 89–96 (2017).

# High-Speed Electron Beam Modulation System Using Electrostatic Deflection and Laser Delivery System to the Specimen in Transmission Electron Microscopy

Takeshi Kaneko<sup>1</sup>, Norihiro Okoshi<sup>1</sup>, Takeo Sasaki<sup>1</sup>, Kazuki Yagi<sup>1</sup>, Takeshi Sato<sup>1</sup>, Hiroki Hashiguchi<sup>1</sup>, Ichiro Ohnishi<sup>1</sup>, Yu Jimbo<sup>1</sup>, Hidetaka Sawada<sup>1</sup>, and Shinsuke Ogiwara<sup>1,2</sup>, Ruth Shewmon Bloom<sup>2</sup>, Bryan Reed<sup>2</sup>, Sang Tae Park<sup>2</sup>, Daniel Masiel<sup>2</sup>

<sup>1</sup> JEOL Ltd. <sup>2</sup> IDES: Integrated Dynamic Electron Solutions, Inc. 5653 Stoneridge Dr. #117 Pleasanton, CA 94588

A high-speed electron shuttering system (Electrostatic Dose Modulator: EDM) using an electrostatic deflector has been developed to control electron dose with a beam-blank switching time of 20 ns. It enables smart electron illumination with quantitative modulation of frequency and duty ratio to control electron dose. A newly developed laser illumination system (Luminary Micro) is used for localized specimen heating. Application data taken with the laser illumination system is reported using gold nanoparticle specimens. The system enables in-situ observation of laser-driven photoreactions during high-resolution imaging in an electron microscope.

## 1. Introduction

In scanning transmission and transmission electron microscopy (STEM/TEM), remarkable resolution improvements have been achieved through development of electron optics, including aberration correctors and cold field emission guns, together with improvement of the electrical and mechanical stability of the equipment, yielding a resolution less than 50 pm. In addition, the analytical performance of STEM has been improved so that atomic-resolution two-dimensional mapping can be obtained routinely with energy dispersive X-ray analyzers (Energy Dispersive X-ray Spectroscopy: EDS) and electron energy-loss spectroscopy (Electron Energy Loss Spectroscopy: EELS). In terms of ease-of-use, automated control of the instrument provides alignment free operation. Whereas the resolution and analytical capability of the integrated system has been continuously improved by such cutting-edge technology developments, future improvements in in-situ environmental observation of function and dynamic structural changes demand greater control of the electron beam.

Thus, in this study, we have developed a high-speed shutter system (Electrostatic Dose Modulator: EDM) using an electrostatic deflector plate. The system can quantitatively control illumination electron dose by changing frequency and duty ratio, using technology similar to the fast electrostatic switching systems used for temporal compressive sensing [1]. It can be utilized for electron-dose control and time-resolved data acquisition with  $\mu$ s or sub- $\mu$ s stroboscopic imaging methods.

We have also developed a laser illumination system that can

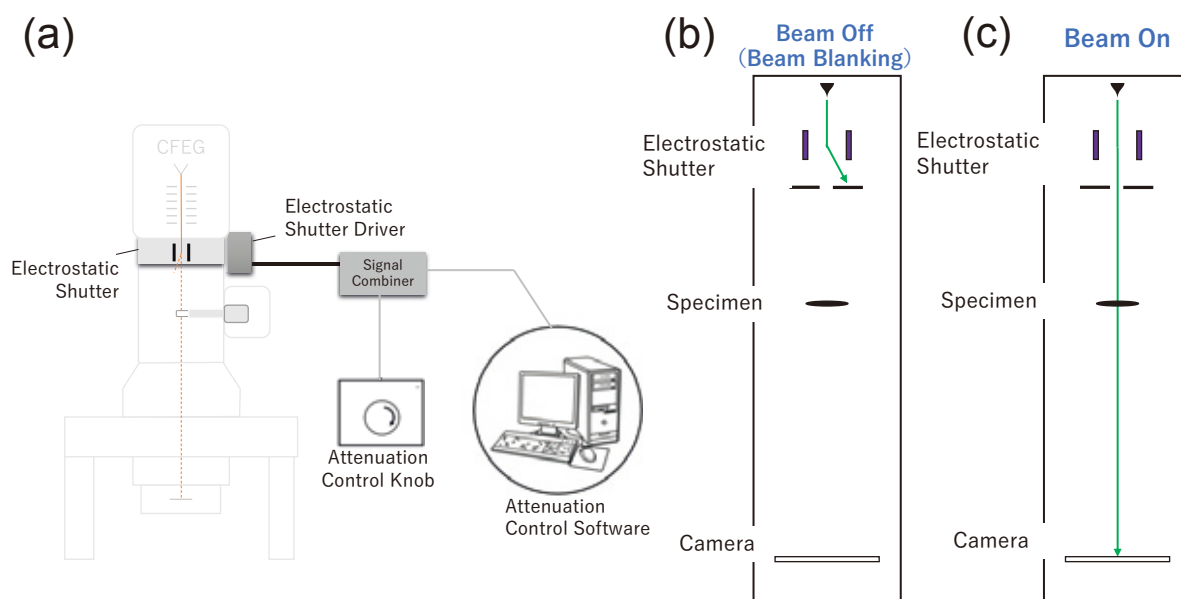
introduce lasers with various intensities into a specimen in an electron microscope. This system focuses and directs a laser beam onto the specimen using lenses and mirrors. This makes it possible to observe the interaction between light and specimens in high resolution TEM or STEM observation. Moreover, the system can be used for highly localized specimen heating; focused laser illumination with a high-power density can be applied locally on the specimen, heating a 50  $\mu$ m region at the center of the field of view. Compared to more conventional methods in which entire TEM samples are heated at once, this produces much less specimen drift and also allows multiple independent heating experiments to be conducted on each specimen.

## 2. High Speed Electron Beam Modulation System Using Electrostatic Deflection in Transmission Electron Microscopy

### 2.1. High-speed blanking technology using electrostatic deflection plates

The Electrostatic Dose Modulator (EDM) is a high-speed beam blanking system consisting of a pair of electrostatic deflector plates mounted above the condenser lens system, a controller, and software (**Fig. 1(a)**). Using EDM, high-speed blanking can switch the electron beam illuminating the sample on and off 100,000 times faster than a conventional beam blanking system. Using pulse width modulation (PWM), the electron beam illumination density to the specimen can be controlled quickly and quantitatively without changing focus or beam alignment, in contrast to conventional methods of changing the illumination

Fig. 1



(a) Schematic diagram of the electrostatic shutter and control system.

(b) Diagram for blanking an electron beam by applying a voltage to an electrostatic shutter.

(c) Diagram in which an electron beam is directed onto a specimen when the electrostatic shutter voltage is turned off.

condition by changing lens strengths and apertures. The 10%-90% switching time between the on and off states (Figs. 1(b-c)) is 20 ns or less, enabling PWM at  $\mu$ s-scale periods.

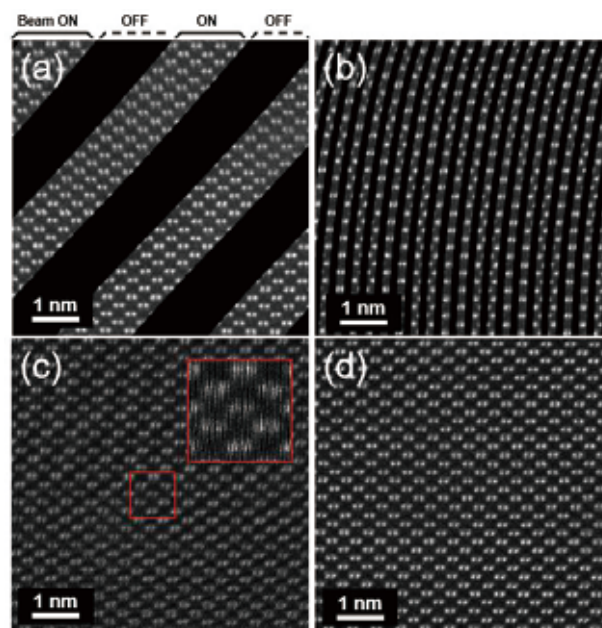
## 2.2. Demonstration of High-Speed Blanking using Electrostatic Deflection

Fast blanking with EDM can be used to pulse the electron beam illumination on the specimen. **Figures 2(a)-2(d)** show an example of fast blanking in operation during annular dark field STEM (ADF-STEM) observation. Figure 2(a) shows a high-resolution ADF-STEM image taken with the blanking period set to 10 ms (5 ms blanking, 5 ms illumination) under STEM observation conditions where each scan line takes approximately 20 ms. The specimen used is a Si [110] crystal and the accelerating voltage is 300 kV. The electron beam is blanked at high speed during STEM observation and the boundary between the illuminated and dark regions of the STEM image is less than 1 pixel thick. It shows that the transition time of blanking (from blank to illumination, and from illumination to blank) is less than the dwell time per pixel of 38  $\mu$ s. No obvious disturbance of the image by blanking can be seen, indicating that the electron probe in STEM is sharply deflected for blanking and returned to the same position at the atomic level. ADF-STEM images with higher blanking frequencies are shown in Figs. 2(b)-2(c). The dark bands corresponding to the times when the beam is blanked progressively become thinner, and in Fig. 2(c) it becomes finer than the width of image of a Si atomic column. In Fig. 2 (d), the period of the blanking (10  $\mu$ s) is less than the dwell time per 1 pixel (38  $\mu$ s), and we can no longer see the vertical dark lines. Instead, the entire image intensity is reduced by a factor of 2 corresponding to the 50% duty ratio. Even in this condition, we observe no distortion or loss of resolution in the image. Combining these techniques allows for selective scans at only particular locations and with controllable illumination intensity.

## 2.3 Current Modulation using Pulsed Illumination

**Figure 3** is a high-resolution ADF-STEM image of Si [110] taken by pulsed electron-beam illumination (frequency 500 kHz,

Fig. 2



ADF-STEM images using illumination with different frequencies, with a STEM image size of  $512 \times 512$  pixels and pixel dwell time of 38  $\mu$ s/pix, using a [110]-oriented Si crystalline specimen.

(a) with frequency of 100 Hz (10 ms period); duty ratio 50% (5 ms illumination)

(b) with frequency of 1 kHz (1 ms period); duty ratio 50% (0.5 ms illumination)

(c) with frequency of 10 kHz (100  $\mu$ s period); duty ratio 50% (50  $\mu$ s illumination)

(d) with frequency of 100 kHz (10  $\mu$ s period); duty ratio 50% (5  $\mu$ s illumination)

period 2  $\mu$ s) and changing the modulation ratio (duty ratio) during STEM observations. The illumination turns on and off on average 9.5 times per 19  $\mu$ s pixel dwell time. Since the illumination blanking speed is faster than the dwell time, the stripe pattern seen in Figs. 2 (a)-(c) will not be observed in the STEM image.

The acceleration voltage is 300 kV and the dwell time is 19  $\mu$ s per pixel ( $1024 \times 1024$  pixels). In Fig. 3 (a), while acquiring

a STEM image of one image for 20 seconds, the duty ratio is changed from 90% to 50%. At a duty ratio of 90%, the illumination is on for 1800 ns, and blanked for 200 ns during each cycle. In the case with a duty ratio of 50%, both the electron beam illumination time and the blanking time are 1000 ns. Figure 3(a) shows the STEM image obtained by changing the duty ratio from 90% to 50% at the middle of the image acquisition; electron dose can be controlled by only changing duty ratio in EDM, again with no change in focus or alignment.

Figure 3(b) shows the STEM image where the duty ratio is gradually changed from 90% to 10% and then increased again to 90%. At the center of the image the electron beam dose is low, whereas the electron beam dose is high at the top and bottom of the image. Even if the dose is changed during scanning, a high-resolution ADF-STEM image can be obtained without specimen drifting. These techniques allow for advanced STEM imaging that changes the illumination current for different parts of the image. This is not only much faster but also much easier than changing illumination current by changing the spot size, condenser lens excitations, aperture sizes, and/or electron gun settings, as it requires neither refocusing nor realignment. The TEM column remains thermally stable because the excitation of each lens does not need to be changed when changing the electron dose.

#### 2.4 EDS True Area Scan by “flyback cut” using EDM

In the case of a scanning system, which deflects an electron beam by passing an electric current through a coil and generating a magnetic field, there is a nonlinear scan region that cannot be used for STEM image acquisition because of the overshoot of the magnetic coil and the limited response speed of signal reception. This nonlinear scanning area is not used for elemental mapping in EDS analyses, even though the electron beam irradiates the specimen during this time. This is called flyback and is unavoidable in scan systems with magnetic coils. This causes needless specimen damage through electron irradiation.

Blanking the electron beam using another magnetic coil does not solve the problem, since the magnetic blanking system will be subject to the same speed limitations as the magnetic scanning system. This modifies the behavior but still introduces scan nonlinearity and needless irradiation of the sample. As the magnetic beam blanker shuts off, the beam can oscillate, overshoot, and produce a poorly aligned beam for some milliseconds.

To solve this problem, we used EDM to remove the flyback area (Fig. 4(a)), taking advantage of the ns-scale switching time to blank and unblank the beam without introducing significant

overshoot or distortion on the time scale of the scan (10-50  $\mu$ s pixel dwell times). We integrated the EDM with an EDS scan system and synchronized the EDM so that the beam is blanked during the flyback time (Fig. 4(b)). The EDM system thus removes the flyback area and the excess irradiation that otherwise occurs during EDS two-dimensional mapping. We call this EDS True Area Scan because it only scans the electron beam during the linear part of the scan, when the beam strikes the area it was intended to strike and nothing more, completely eliminating the extra irradiation during flyback.

#### 2.5 Applications of EDS True Area Scan

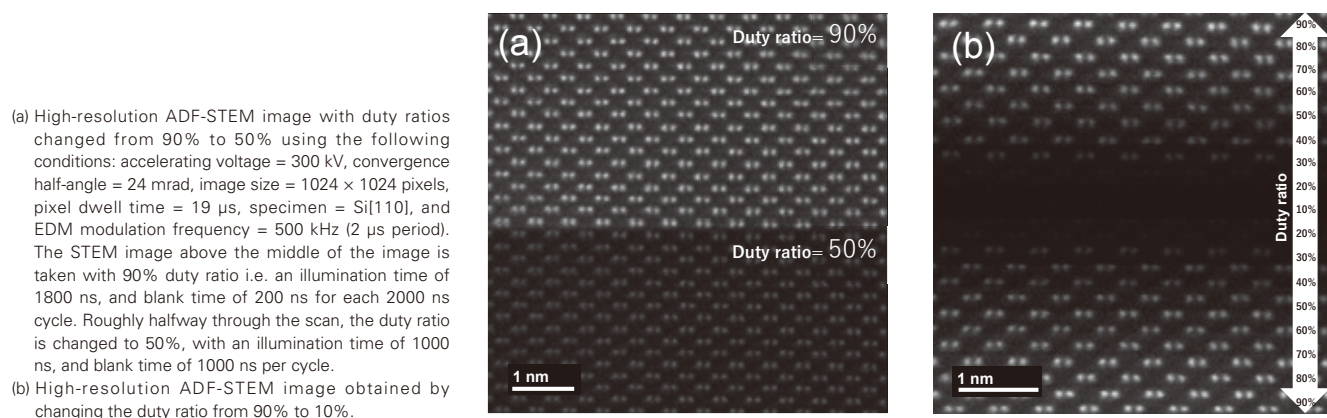
Figures 5(a) and 5(b) shows the image and intensity profile of the scan area taken by the CMOS camera. Figure 5(a) is the conventional scan area image and 5(b) is the scan area image with EDM True Area Scan. In the conventional scanning, the specimen is irradiated with high-intensity electron beam in the flyback area. On the other hand, in the scan with EDS True Area Scan, the specimen is scanned without extra non-linear irradiation. Figures 5(c) and 5(d) shows the EDS mapping of SrTiO<sub>3</sub> from the orientation of [100] direction. Figure 5(c) shows the conventional EDS elemental mapping, and Fig. 5(d) shows the EDS “true area” elemental mapping with flyback cut by EDM. In conventional EDS elemental mapping, the flyback area is not removed, so electron beam damage to the specimen can be observed as shown by the white dashed line area in Fig. 5(c). The intensity profile in right hand side in Fig. 5(c) shows the signal from EDS for each element of Sr, Ti, and O as a function of the time, corresponding the number of the atoms in the specimen. Decreasing the signal indicated that the number of the atoms inside the specimen is reduced by electron irradiated damage due to large current. On the other hand, reduction of the signal intensity profile with true area scan by EDS True Area Scan in EDS elemental mapping is relatively small even with large current shown in the right-hand side of Fig. 5(d). It can also be seen in left hand figure in Fig. 5(d), showing that there is relatively uniform intensity contrast in EDS two dimensional elemental mapping due to reducing electron beam damage to the specimen.

### 3. Laser Introduction System to the Specimen [2]

#### 3.1. Laser illumination of the specimen

Luminary Micro was developed as a compact specimen optical excitation system for TEM. The system consists of a continuous-wave (CW) laser, a compact optical delivery system, and a

**Fig. 3 High-resolution ADF-STEM image using pulsed illumination.**

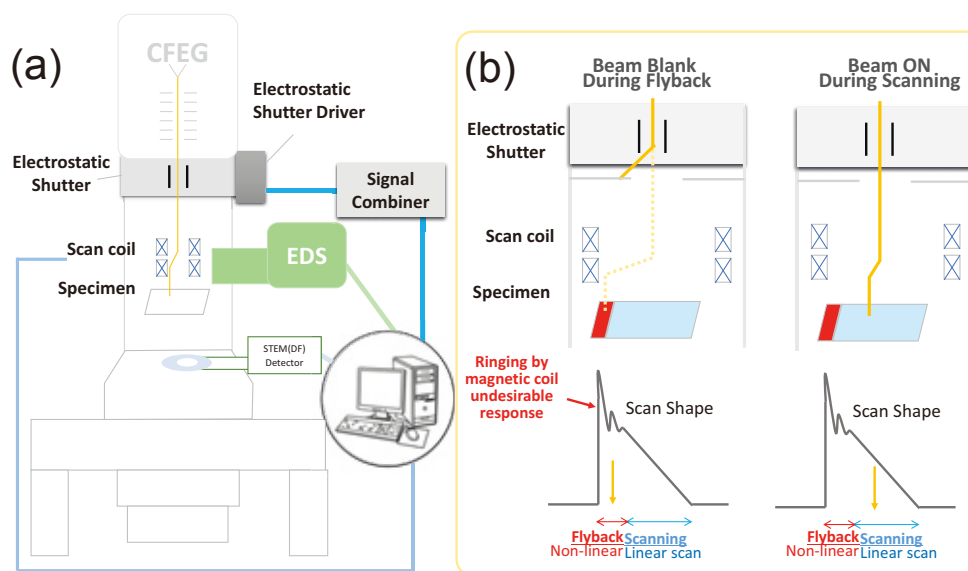


mirror (Fig. 6(a)). The laser is introduced through a backscattered electron imaging device (BEI) port and can irradiate the specimen from directly above using mirrors and other optical systems. The laser illumination position on the specimen can be precisely aligned to the center of the observed area of the specimen. The laser illumination area is 20-50  $\mu\text{m}$  diameter, and the illumination

intensity can be adjusted by controlling the laser output.

The left image in Fig. 6(b) is a high-resolution image of an amorphous carbon film (QUANTIFOIL by QUANTIFOIL Micro Tools), in which holes of several  $\mu\text{m}$  diameter are arranged. Fig. 6(b) shows the same region after illuminating the specimen with 1 W of laser power for 1 second. A hole of about

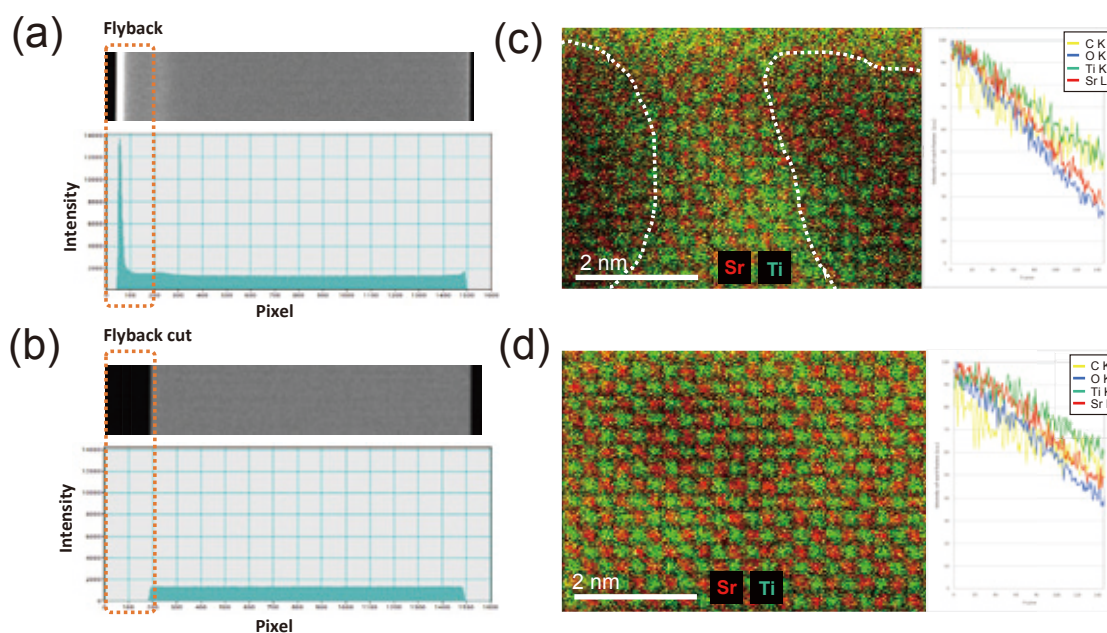
**Fig. 4**



(a) Configuration diagram of EDS True Area Scan.

(b) The left-hand schematic diagram shows blanking during the flyback time by applying voltages to the EDM electrostatic plates. The right-hand schematic shows electron beam illumination with a linear scan for EDS mapping on the specimen with no voltage to the EDM. The system automatically switches modes during the flyback time of every single scan line.

**Fig. 5**



EDS True Area Scan with flyback cut with EDM using an accelerating voltage of 300 kV and a beam current of 660 pA. The specimen is  $\text{SrTiO}_3$  and the magnification is 25Mx. The image is 256 pixels wide and the flyback time at the end is equivalent to 128 pixels. The pixel dwell time is 10  $\mu\text{s}$ .

(a) (Upper) Real-space image of part of the scan as captured by a CMOS camera. (Lower) The corresponding intensity profile summed in the vertical direction.

(b) As (a), but with the True Area Scan flyback-cut system engaged. The true scan area is uniformly illuminated and the total dose is significantly reduced, especially near the left edge.

(c) (Left) EDS two-dimensional elemental map using a conventional scanning system corresponding to (a). (Right) The EDS signal intensity for each element as a function of the time, showing the decay rate caused by specimen damage by the electron beam.

(d) As (c), but with the True Area Scan flyback-cut system engaged. The image is much more uniform and the rate of damage is significantly reduced.

30-40  $\mu\text{m}$  diameter has been created by the laser illumination, aligned to the center of the field of view. By reducing the laser power, it is possible to observe heating phenomena and the interaction between light and matter at the atomic resolution.

### 3.2. Demonstration of specimen heating in a localized area by Luminary Micro

Figure 7(a) shows a high-resolution TEM image of gold particles before laser illumination. A laser with a wavelength of 577 nm illuminates the particles with a power of 2 mW and an area of about 40  $\mu\text{m}$  diameter. Figure 7(b) shows the sample after 5 minutes of illumination, during which some of the gold sublimated due to laser heating, causing the particles to become smaller. Because the laser heating is localized, the specimen drift caused by changing the temperature of the support film is minimal. Thus, high-resolution TEM imaging observation is feasible even in high-temperature heating conditions. Figure 7(c) shows the gold particles after 5 minutes of additional illumination at 5 mW. The gold particles continued to reduce in size, and the sample drift was still relatively small.

Luminary Micro is utilized not only for in-situ observation with laser excitation of a specimen, but also for heating a specimen without a special holder. In combination with EDM, Luminary Micro can also be used for microsecond time-resolved studies using the pump-probe method, since the specimen laser can be modulated by the same timing control system that controls the EDM.

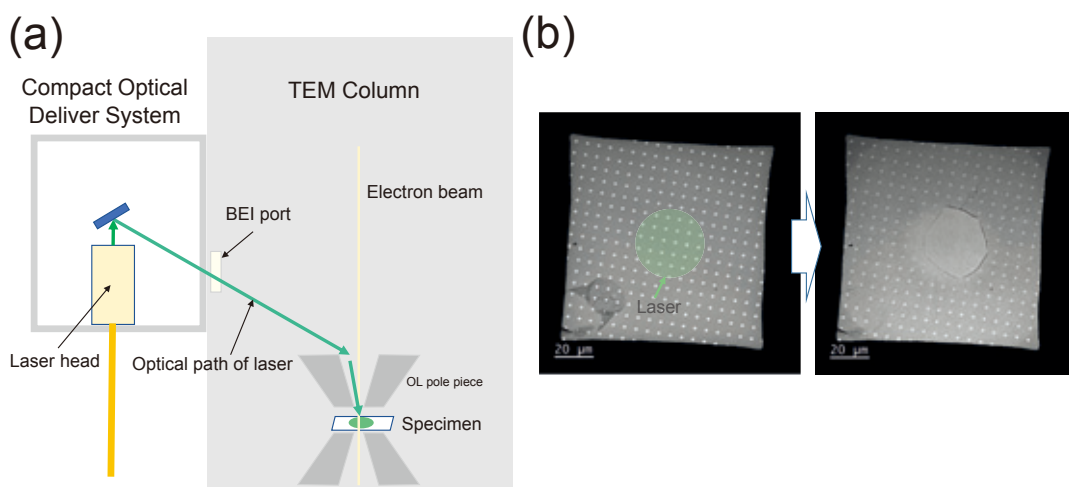
## Summary

This paper introduces advanced illumination current modulation called EDM using electrostatic deflection plates and high-speed blanking. We demonstrated dose control in STEM using EDM. Further, the EDM system enabled a True Area Scan system to reduce sample damage in STEM by turning off the beam during flyback. This paper also reports application data demonstrating a laser introduction system for the specimen called Luminary Micro, showing sublimation of gold nanoparticles imaged at atomic resolution with relatively little sample drift. These techniques open the possibility of unprecedented in-situ and time-resolved observations without the need of laser-driven photocathodes used in previous work [2].

## References

- [ 1 ] B. W. Reed, A. A. Moghadam, R. S. Bloom, S. T. Park, A. M. Monterrosa, P. M. Price, C. M. Barr, S. A. Briggs, K. Hattar, J. T. McKeown, and D. J. Masiel, Electrostatic subframing and compressive-sensing video in transmission electron microscopy. *Structural Dynamics* **6**, 054303 (2019).
- [ 2 ] Thomas LaGrange, Geoffrey H. Campbell, Jeffrey D. Colvin, Bryan Reed, Wayne E. King, J Mater, Nanosecond time resolved electron diffraction studies of the  $\alpha \rightarrow \beta$  in pure Ti thin films using the dynamic transmission electron microscope (DTEM) *Sci* **41**, 4440 (2006).

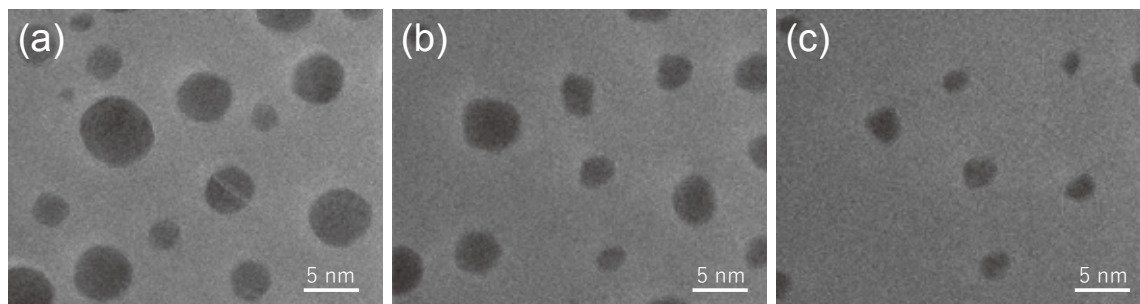
Fig. 6



(a) Schematic of a laser introduction system (Luminary Micro).

(b) Amorphous carbon film before (left) and after (right) laser illumination (specimen: QUANTIFOIL by QUANTIFOIL Micro Tools), with the estimated laser spot superposed in green.

Fig. 7



(a) High-resolution TEM image before laser illumination of gold nanoparticles on a thin carbon film using an accelerating voltage of 300 kV.

(b) High-resolution TEM image after 5 minutes of illumination with a laser power of 2 mW and an illumination area of 40  $\mu\text{m}$  diameter.

(c) High-resolution TEM image after 5 minutes of illumination with a laser power of 5 mW and an illumination area of 40  $\mu\text{m}$  diameter.

# The New Detection System of High-End FE-SEM JSM-IT800 Super Hybrid Lens <SHL>

Tatsuro Nagoshi, Yuuki Yamaguchi EP Business Unit, JEOL Ltd.

Scanning Electron Microscope (SEM) is able to acquire various information on a specimen surface by selecting energy and emission angles of electrons emitted from the specimen. The latest high-end FE-SEM JSM-IT800 <SHL> is equipped with Super Hybrid Lens (SHL) and various detectors including a newly developed Upper Hybrid Detector (UHD). It is possible to select information such as surface structure and composition of the specimen with high spatial-resolution in various fields. In this paper, we explain various information on a specimen surface provided by electrons emitted from the specimen. And then, we introduce the information obtained by using the various detectors together with observation examples.

## Introduction

SEM enables us to obtain images with information on specimen surface by scanning focused electron beam and detecting secondary electrons (SEs) and backscattered electrons (BSEs) emitted from the vicinity of the surface. Information in SEM images changes depending on energy and emission angles (define the angle parallel to the specimen surface as zero) of emitted electrons. For example, SEs are usually thought to reveal surface morphology. However, if the detector acquires both SEs and BSEs, the image reflects not only the structure of the specimen surface with SEs, but also the composition of the specimen with BSEs [1]. Therefore, it is necessary to select an appropriate detector for purposes.

JSM-IT800 <SHL> has features such as an intuitive graphical user interface and an energy dispersive X-ray spectroscopy (EDS) integration system that enables seamless operation both of observation and analysis [2]. Furthermore, as a high-end model of JSM-IT800 series, it is equipped with a new detection system that enables selecting information with high spatial-resolution for a wide variety of specimens. This new detection system has made possible to acquire various information on specimen by selecting energy and emission angle of the emitted electrons.

## 1. Difference in image depending on energy and emission angle of emitted electrons

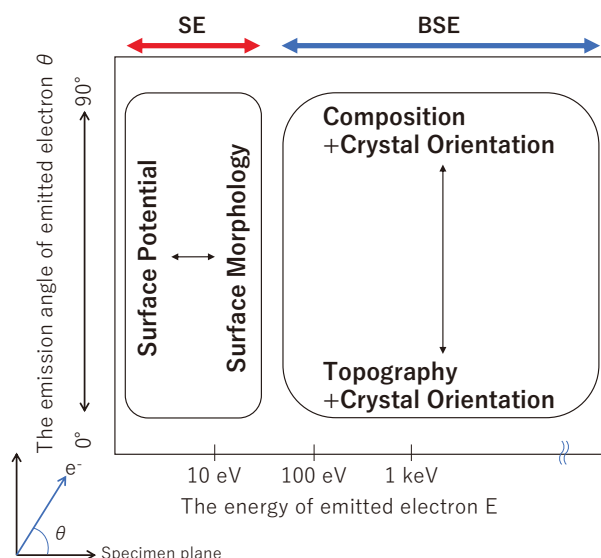
In SEM observation, electrons emitted from a specimen surface by irradiation with a primary electron beam are classified into SEs and BSEs. **Figure 1** shows the difference in SEM images which depends on the energy and the emission angles.

### 1.1. Secondary electrons (SEs)

SEs are excited from atoms of a specimen. They are generated in inelastically scattering process when incident electrons

penetrate into the specimen. Since energy of SEs is several tens of eV or less, the SEs generated within about 10 nm from the specimen surface can escape into a vacuum. When the primary electron beam enters the slope, the distance from the inside of

**Fig. 1 SEM image information that depends on the energy and the emission angle of the emitted electrons.**



The horizontal axis is the energy  $E$  of the emitted electrons, the vertical axis is the emission angle  $\theta$  of the emitted electrons, and the emission angle parallel to the specimen surface is defined as  $0^\circ$ . SE images have contrast of surface potential or surface morphology depending on the energy. BSE images have contrast of composition or topography which includes crystal orientation depending on the emission angle. In this paper, the "structure" of the specimen surface obtained by SEs is referred to as surface morphology, and the one obtained by BSEs is referred to as topography.

the specimen, where the SEs are generated, to the slope becomes short, so that the SEs are more easily emitted. As a result, the slope gives a brighter contrast in the image than a flat surface, and surface morphology of the specimen surface is enhanced. In addition, SEs with relatively low energy (several eV) are easily affected by differences in surface potential and charged states on the specimen. Therefore, it is possible to acquire images containing information on the surface morphology and surface potential by selecting the energy of SEs.

### 1.2. Backscattered electrons (BSEs)

BSEs are emitted from specimens in the opposite direction of the incident electrons when they are elastically or inelastically scattered. Since the maximum energy of BSEs is the same energy as the incident electrons, the escape depth of BSEs is deeper than that of SEs. Since the BSE images have a contrast depending on the chemical composition (the average atomic number) of the specimen, the image has compositional information on the specimen surface. In addition, since the emission angle of BSEs changes on the slope angle of the specimen, the image has also the topographic information on the specimen. If the emission angle of BSEs is large, the compositional information becomes dominant, and if it is small, the topographic information becomes dominant. Furthermore, BSE images are also useful for crystal orientation information on specimens [3]. The electron channeling effect, in which the penetration depth of incident electrons changes depending on the crystal orientation of the specimen, changes

the number of BSEs emitted from the specimen.

As shown above, it is possible to obtain images based on the target information by selecting the detection range of SEs or BSEs.

## 2. The configuration of detection system in JSM-IT800 <SHL>

As shown in **Figure 2**, JSM-IT800 <SHL> consists of Super Hybrid Lens (SHL), a specimen stage bias function and detectors placed at four locations.

### 2.1. Super Hybrid Lens

In general, an electron beam is focused on a specimen surface with only a magnetic lens. JSM-IT800 <SHL> is equipped with an objective lens which combines with a magnetic lens and an electrostatic lens. In this objective lens, a tubular accelerating electrode is located inside the magnetic lens in order to superpose an electrostatic lens. As a result, the chromatic aberration of the objective lens can be reduced, and the primary electron beam can be focused more finely. Further, this electrostatic lens can draw electrons emitted from the specimen surface into the objective lens. By changing working distance (WD), the magnetic field and electrostatic field near the specimen can be changed and the trajectories of electrons can be controlled to some extent. In addition, JSM-IT800 <SHL> enables switching between SHL mode combined with a magnetic lens and an electrostatic lens, and standard (STD) mode with only the magnetic lens (**Figure 3**).

**Fig. 2 JSM-IT800 <SHL> detection system.**

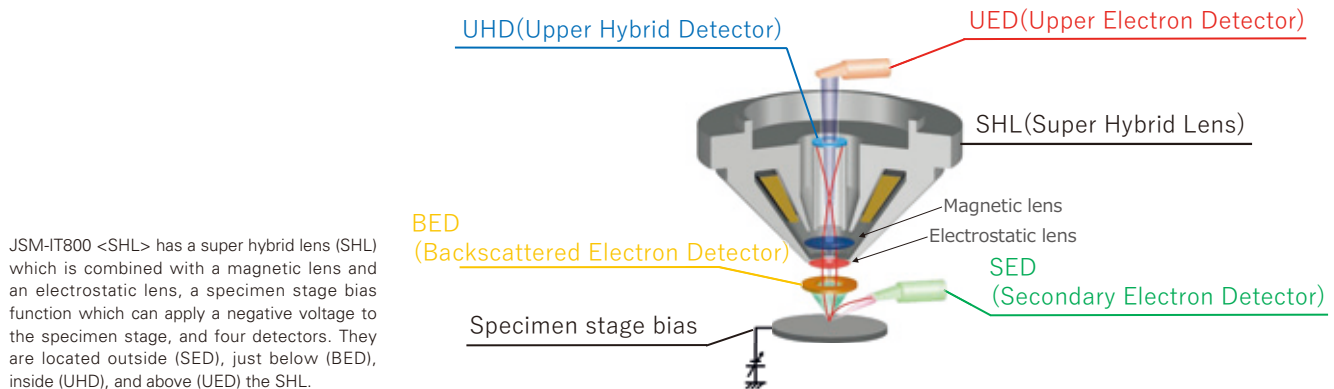
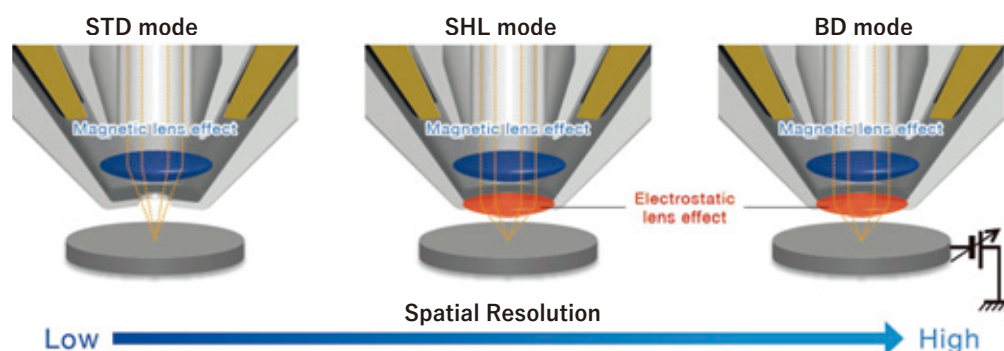


**Fig. 3 Observation mode of JSM-IT800 <SHL>.**



JSM-IT800 <SHL> has STD mode with only a magnetic lens, SHL mode with a magnetic lens and an electrostatic lens superposed, and BD mode with specimen stage bias function. Spatial-resolution increases in the order of STD mode, SHL mode, and BD mode.

## 2.2. Specimen stage bias

JSM-IT800 <SHL> has Beam Deceleration (BD) mode, which decelerates the primary electron beam by applying a negative bias voltage up to -5 kV to a specimen stage (Figure 3) as well as SHL mode which combines with a magnetic lens and an electrostatic lens. In BD mode, the chromatic aberration of the electron beam is reduced even at a low acceleration voltage by deceleration of the electron beam just before the specimen, and then it enables observation with high spatial-resolution [4]. In addition, this negative bias voltage accelerates the electrons emitted from the specimen as an accelerating electrostatic field. As a result, it is possible to change the trajectories of the emitted electrons.

## 2.3. Detector

As shown in Figure 2, the four detectors are located at outside, just below, inside, and above the objective lens.

### 2.3.1 Secondary Electron Detector (SED)

SED is a so-called ET (Everhart-Thornley) detector that consists of a scintillator and a photomultiplier tube, placed outside the objective lens. In addition, a collector electrode is installed in front of the scintillator. By applying a voltage of +300 V to the collector electrode, SEs are collected. Then, the SEs are accelerated by a high voltage applied to the scintillator, the SEs colliding with the scintillator are converted into light, and the light is converted into an electric signal in the photomultiplier tube to obtain SEM images. SED can detect not only SEs but also BSEs emitted in the direction of the detector. In addition, since SED is placed at the side of the objective lens, the topographic contrast is strongly enhanced as if it was illuminated from the direction of the detector (illumination effect).

### 2.3.2 Backscattered Electron Detector (BED)

BED is an annular detector located just below the objective lens. Due to this location, it has a large solid angle of the detection element from the electron beam irradiation position, and it can detect BSEs with high efficiency. Conventionally, the detection element is composed of a silicon photodiode. When BSEs enter the detection element, electron-hole pairs are generated inside, and the current of them is detected.

It is possible that JSM-IT800 <SHL> is equipped with new two types of BEDs as well as the conventional silicon photodiode type (Table 1).

One is Scintillator BED (SBED) which has an annular scintillator as the detection element. In SBED, BSEs are converted into light in the scintillator and detected. Compared to the silicon photodiode type, it has the features of high responsiveness and high sensitivity at low energy (for example, 1 kV).

The other is Versatile BED (VBED). VBED has a silicon photodiode as the detection element which is composed of the center parts divided into 5 segments and shadow part. By using VBED, it is possible to select the emission angle of BSEs. Therefore, we can select the compositional and topographic information, and also obtain topographic information with a strong illumination effect. Furthermore, 4 segments around the center part of VBED enable us to reconstruct of three-dimensional images of the specimen surface.

### 2.3.3 Upper Hybrid Detector (UHD)

UHD is located inside the objective lens and it can be used in SHL and BD modes. It detects SEs that are drawn by the electrostatic lens or accelerated by the specimen stage bias into the objective lens. It also detects BSEs that are emitted at high angles. The images by using UHD do not have illumination effect like SED images and they have less shadow effect.

### 2.3.4 Upper Electron Detector (UED)

UED is located on top of the objective lens and it can be used in SHL and BD modes. It detects BSEs and SEs that are passed through the UHD. It is capable of detecting BSEs and SEs emitted at higher angles than the electrons detected by UHD. In addition, an energy filter is placed in front of the detector, and we can select a mixed image of SEs and BSEs and an image of only BSEs. The images of only BSEs have compositional contrast and crystal orientation contrast with little topographic information.

## 3. Observation mode of JSM-IT800 <SHL> and electron detection-range

As mentioned above, JSM-IT800 <SHL> has the three observation modes: STD, SHL, and BD mode (Figure 3). It is possible to obtain information on the target specimen surface by selecting an appropriate detector in these observation modes. Here, the electron detection range of each detector is shown for each observation mode.

**Table 1 Various BEDs that can be attached to JSM-IT800 <SHL>.**

	BED	SBED	VBED
Element Shape			
Detection Element	Silicon photodiode type	Scintillator type	Silicon photodiode type
Feature	General purpose	High responsiveness High sensitivity at low energy	5 segments + Shadow part Selection of emission angle 3D reconstruction

JSM-IT800 <SHL> can be attached to not only a conventional silicon photodiode type BED, but also a SBED with high responsiveness and high sensitivity even for low energy, and a VBED with 6 segmented parts which can select the emission angle.

### 3.1. STD mode

Figure 4(a) shows the range of electron detection-energy and emission angles of each detector in STD mode. Only SED and BED can be used because the number of electrons entering the objective lens is small. SED detects SEs emitted in a wide range of directions and BSEs emitted to the direction of SED. Therefore, SED provides surface morphology and topographic information with illumination effects. BED detects middle and low angle BSEs. Therefore, BED provides images in which topographic, compositional, and crystal-orientation information are mixed.

### 3.2. SHL mode

Figure 4(b) shows the electron detection range of each detector in SHL mode. Since most of the SEs are drawn into the objective lens by the electrostatic lens, SED detects only BSEs. Therefore, SED with SHL mode provides topographic information with stronger illumination effects than with STD mode. SEs are detected by UHD inside the objective lens. Although the UHD also detects some of the BSEs at high angles due to the electrostatic lens, the surface morphology and surface potential information is dominant because of the high detection rate of SEs. UED detects high emission angle SEs and BSEs that are not detected by UHD. By using the energy filter, it can detect only BSEs, and compositional information with less topographic information can be obtained. Similar to STD mode, BED in SHL mode can detect BSEs at middle and low angles.

Furthermore, changing the WD makes it possible to select the energy of SEs entering the objective lens in SHL mode. In the long WD, SEs with the low energy which have the surface potential information can be detected. In the short WD, SEs with relatively high energy which have the surface morphology information can be detected. Therefore, the minimum energy of SEs that can be detected by UHD and UED in Figure 4(b) depends on WD.

### 3.3. BD mode

Figure 4(c) shows the electron detection range of each detector in BD mode which specimen stage bias is applied in SHL mode. Due to the specimen bias, SEs are accelerated

and enter the objective lens. Since the SEs with low energy go through along the optical axis in the objective lens, they are detected by UED not UHD. Although UED also detects BSEs at high angles, SEs are dominant. Therefore, the images have the information on surface morphology and surface potential. SEs with high energy go through away from the optical axis and they are detected by UHD. In addition, since BSEs are also accelerated towards the objective lens by the specimen bias, UHD in BD mode detects the BSEs emitted at lower angles than in SHL mode. Therefore, we can obtain surface morphological and topographic information. BED with BD mode can acquire only BSEs with relatively low angles compared to SHL mode. Therefore, BED provides images with topographic information.

As shown above, Table 2 summarizes the information in images which depends on the detectors and observation mode.

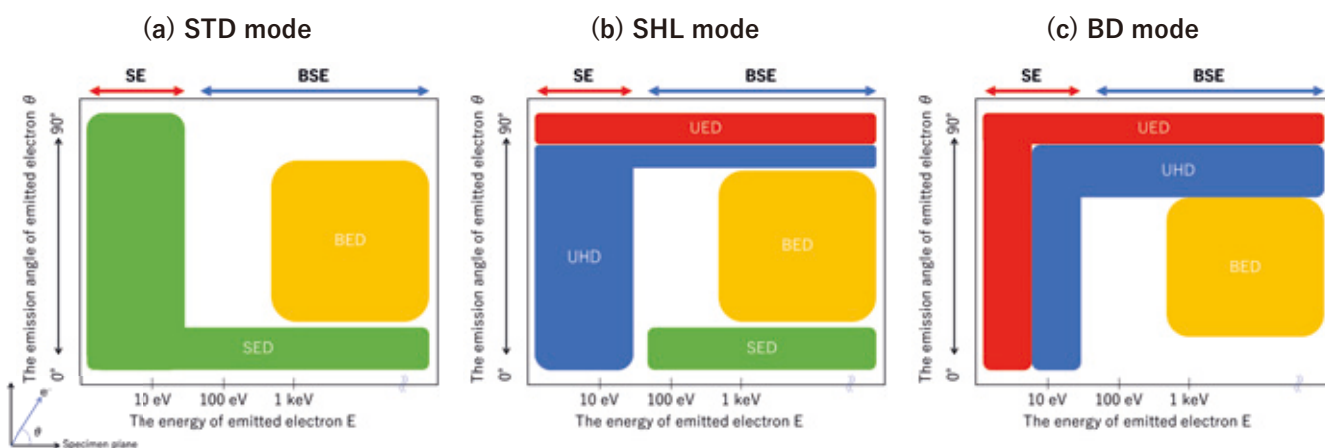
## 4. Observation examples by using new detection system

As mentioned above, the various detectors installed in JSM-IT800 <SHL> acquire images with different information by selecting energy and emission angles of SEs and BSEs. In this chapter, we introduce how to use detectors and observation conditions to accurately acquire information in various specimens.

### 4.1. Observation of topographic structure for a non-conductive specimen by using SED

Observation of topographic structures in specimens requires detection of BSEs emitted at low angles by using SED as shown in Figure 4(a, b). However, in case of non-conductive specimens, images of topographic structures become unclear due to electron charging unless the observation mode is properly selected. Because of low energy of SEs, the trajectories of SEs are affected by the charging. Since SED with STD mode detects SEs and BSEs, charging contrast appears. On the other hand, SED with SHL mode detects BSEs except SEs, so the charging contrast does not appear. Figure 5 shows images of a fracture surface in resin. For the resin without conductivity, charging contrast appears in observation by using SED with STD mode (Figure 5(a)). On the other hand, the charging contrast is

Fig. 4 SE and BSE detection range of detectors for each observation mode.



(a) STD, (b) SHL, and (c) BD mode. The horizontal axis is the energy  $E$  of the emitted electrons, the vertical axis is the emission angle  $\theta$  of the emitted electrons, and the emission angle parallel to the specimen surface is defined as  $0^\circ$ .

suppressed and the topographic structures is clearly observed by using SED with SHL mode (Figure 5(b, c, d)).

**4.2. Observation of organic substances on metal surface by using SBED**

To obtain the compositional contrast of organic substances on a metal surface, it is necessary to acquire BSEs images at low incident voltages. An electron beam with low incident voltages makes penetration depth in a specimen small, and it enables us to observe the outermost surface of a specimen. For example, the penetration depth of an incident electron beam into gold (Au), which is simulated by Electron Flight Simulator (Small World LLC), is around 40 nm at an incident voltage of 3.0 kV and around 7 nm at an incident voltage of 0.8 kV (Figure 6). In addition, it is necessary to detect BSEs with middle or high angle emission in order to obtain compositional contrast. According to Figure 4, BED enables us to obtain compositional contrast in any observation mode. Therefore, SBED with high sensitivity for low energy is useful. Figure 7 shows the BSE images of a gold wire obtained at different incident SBED voltages. At an incident voltage

of 3.0 kV, channeling contrast is enhanced (Figure 7(a)), but at an incident voltage of 0.8 kV, the compositional contrast of organic substances on the surface is enhanced (Figure 7(b)).

**4.3. Selection of compositional and topographic contrast by using VBED**

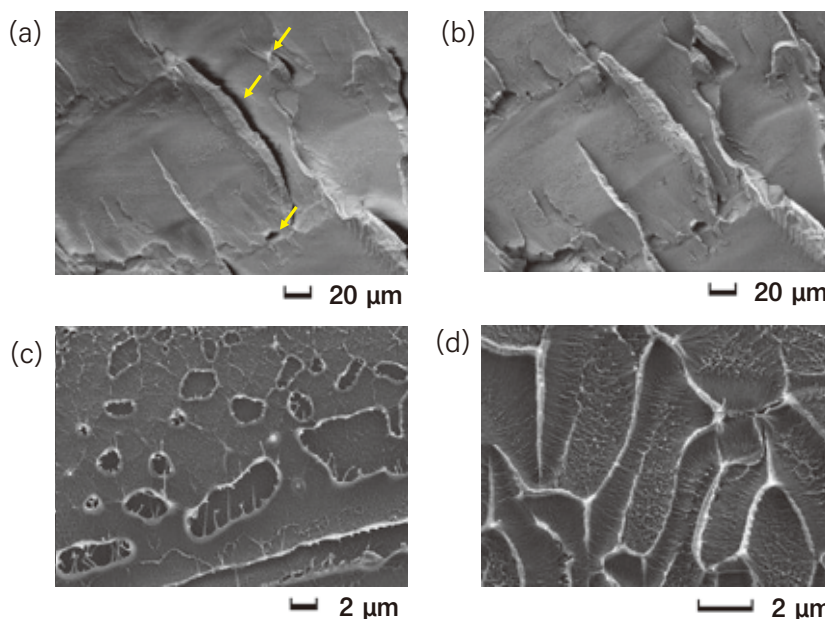
BSE images have compositional and topographic contrast of specimens. VBED makes it possible to select those contrasts. In an inner detection element of VBED which detects BSEs emitted at high angles, compositional contrast is enhanced. In outer detection elements of VBED which detect BSEs emitted at low angles, topographic contrast is enhanced. Figure 8 shows examples of observing phosphor particles in an aluminum film. In a BSE image acquired by the inner element, compositional contrast is enhanced (Figure 8(a)), and the phosphor particles on aluminum film (arrow A) is clearly observed. Compositional contrast of the phosphor particles under the aluminum film (arrow B) is also observed with bright although edges are blurred. On the other hand, topographic contrast of the phosphor particles is enhanced in a BSE image acquired by the outer elements (Figure 8(b)).

**Table 2 SEM image information obtained by each detector in each observation mode.**

	SED	BED	UED	UHD
STD mode	Surface Potential Surface Morphology Topography	Composition Topography Crystal Orientation	-	-
SHL mode	Topography	Composition Topography Crystal Orientation	Composition Crystal Orientation Surface Potential* Surface Morphology*	Surface Potential Surface Morphology
BD mode	-	Composition Topography Crystal Orientation	Surface Potential Surface Morphology	Surface Morphology Topography

\* Controllable with energy filter

**Fig. 5 Observation of resin fracture surface by using SED.**



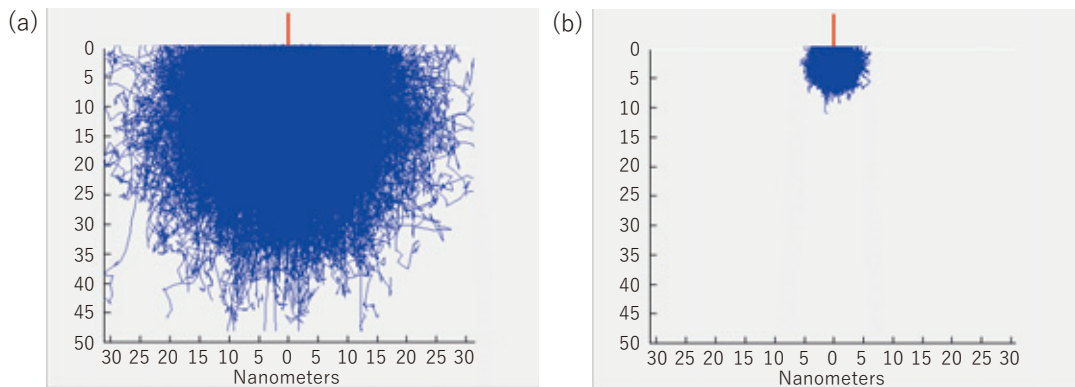
Observation of resin fracture surface by using SED at an incident voltage of 1.0 kV. (a) Charging contrast is observed in STD mode (black part of the arrow). (b) No charging contrast is observed in SHL mode. (c, d) The topographic structure is observed on magnified images in SHL mode.

#### 4.4. Selection of voltage and morphological contrast by using UHD

Since boron nitride tends to have a surface potential difference on own surface., both of voltage contrast and morphological contrast are observed. In order to obtain such contrast, it is necessary to select energy range of SEs. As shown in Figure 4 (b), UHD is useful to detect low energy SEs of several eV. In SHL mode and WD 4 mm, voltage contrast is enhanced (Figure 9(a)). The detection energy range of SEs can be modified by changing WD. For example, in SHL

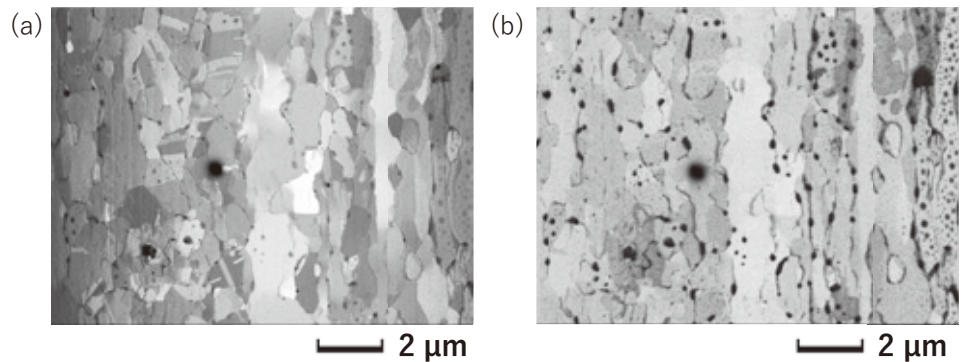
mode and WD 1 mm, morphological contrast is enhanced and voltage contrast is suppressed (Figure 9(b)). This is because high energy SEs of several tens of eV are mainly detected. In order to further enhance the morphological contrast, it is effective not to detect secondary electrons with low energy in UHD as shown in Figure 4(c). For example, in BD mode and WD 2 mm, morphological contrast is enhanced and voltage contrast is almost not observed (Figure 9(c)). This is because not only SEs with high energy but also BSEs with topographic information are detected.

**Fig. 6 Simulation of penetration depth of incident electron beam in a bulk sample of gold (Au).**



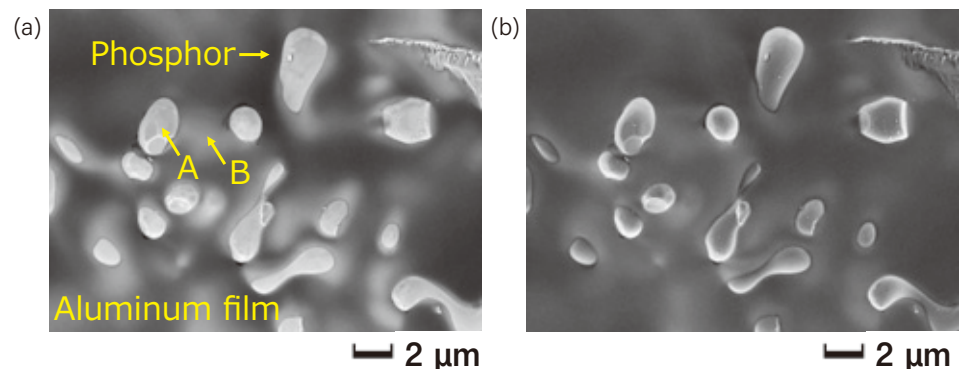
The simulation was performed with Electron Flight Simulator (manufactured by Small World LLC). Red lines show the incident electron beam, and blue lines show the scattering orbit of the incident electron beam in the specimen. (a) The penetration depth is about 40 nm at an incident voltage of 3.0 kV, and (b) the penetration depth is about 7 nm at an incident voltage of 0.8 kV.

**Fig. 7 Observation of gold wire by using SBED.**



(a) Channeling contrast is enhanced at an incident voltage of 3.0 kV. (b) The compositional contrast of organic substances on metal surface is enhanced at an incident voltage of 0.8 kV.

**Fig. 8 Observation of phosphors by using VBED.**



Observation of phosphors by using VBED at an incident voltage of 3.0 kV. (a) The compositional contrast between phosphor particles and aluminum film is enhanced by using the inner element of VBED. (b) The topographic contrast of phosphor particles is enhanced by using the outer elements of VBED.

#### 4.5. Observation of fine structure for a non-conductive specimen

Although it is possible to observe the fine structure of polymer materials by using UHD, the non-conductive materials produce charging contrast in their images. Therefore, we need to eliminate low energy SEs in their images. Therefore, it is better to use UHD with BD mode as shown in Figure 4(c) than SHL mode as shown in Figure 4(b). **Figure 10** shows acrylic particles which are non-conductive polymer materials. In SHL mode and WD 4 mm, due to the effect of charging contrast by SEs with low energy of several eV, bright streaks appear in the images and the surface morphology becomes unclear (Figure 10(a)). However, the charging contrast is suppressed in SHL mode and WD 1 mm (Figure 10(b)), and the charging contrast is not observed in BD mode and WD 2 mm (Figure 10(c)). This is because high energy SEs and BSEs are mainly detected and low energy SEs are not detected.

#### 4.6. Observation of segregation in metal by using UHD

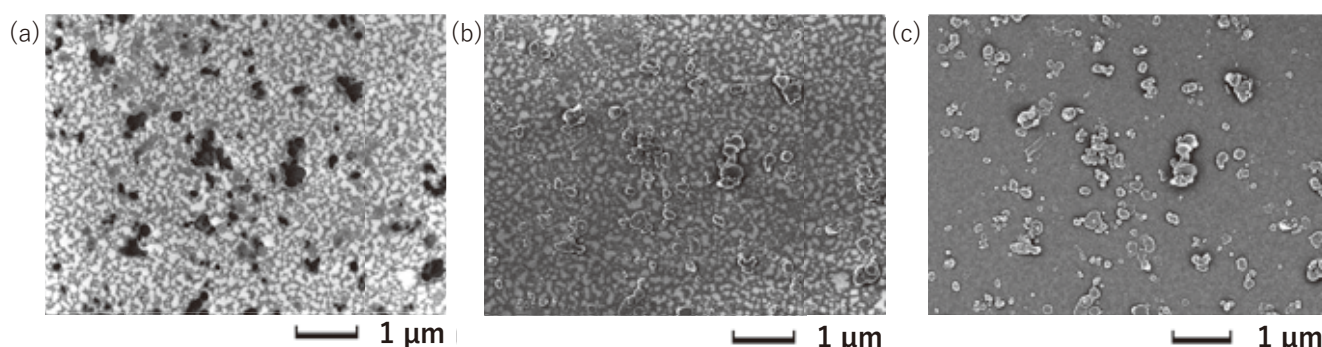
When we observe segregation with different compositions in metals, it may be difficult to distinguish each kind of segregation by compositional contrast. Even in this case, if there are surface potential difference for each kind of the segregation, it is possible to easily distinguish by enhancing voltage contrast. **Figure 11** shows EDS elemental maps and observation images of a cross section of an aluminum alloy. From the EDS elemental maps,

segregation of Cu and Si-Mn-Fe are observed in the aluminum alloy (Figure 11(a)) and EDS spectra of them are shown in Figure 11(b). However, it is difficult to distinguish between them in the BED image (Figure 11(c)). In order to distinguish them, we need to detect low energy SEs which are affected by surface potential using UHD with SHL mode as shown in Figure 11(d). Since the contrast is different between the two kinds of segregation, these can be easily distinguished. This is because there is a difference in surface potential between them.

#### 4.7. Observation of supported catalysts by using UHD and UED

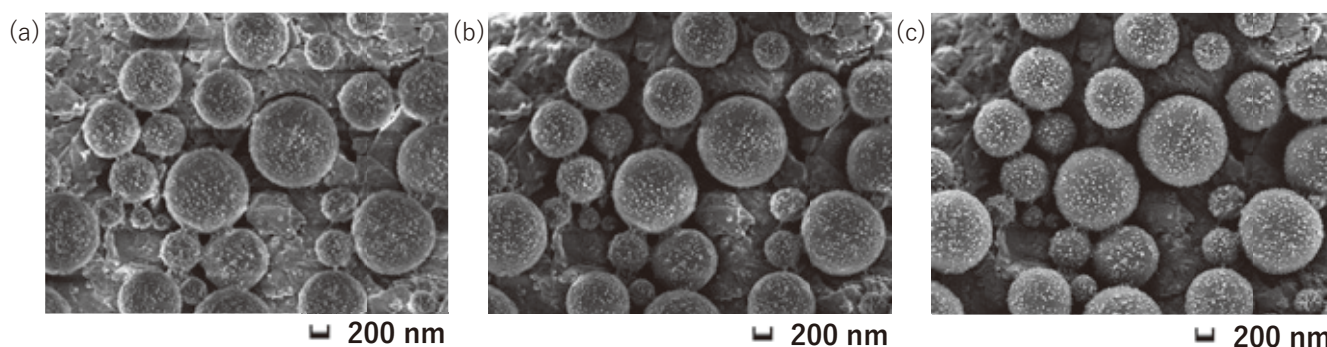
Surface fine structure of particles with catalysts such as supported catalysts can be observed by detecting low energy SEs. In this purpose, using UHD with SHL mode as shown in Figure 4(b) is needed. On the other hand, since UED detects BSEs emitted at high angles, the distribution of the catalyst can be revealed by compositional contrast with less morphological contrast. Figure 12 shows titanium-oxide particles with silver nanoparticles. The surface structure of the titanium-oxide particles is observed by using UHD (**Figure 12(a)**), and the compositional contrast of the silver nanoparticles is observed brightly by using UED (Figure 12(b)). In this observation, a negative voltage of -500 V is applied to the UED energy filter. Therefore, SEs are not detected and only BSEs are detected by UED.

**Fig. 9 Observation of Boron Nitride by using UHD.**



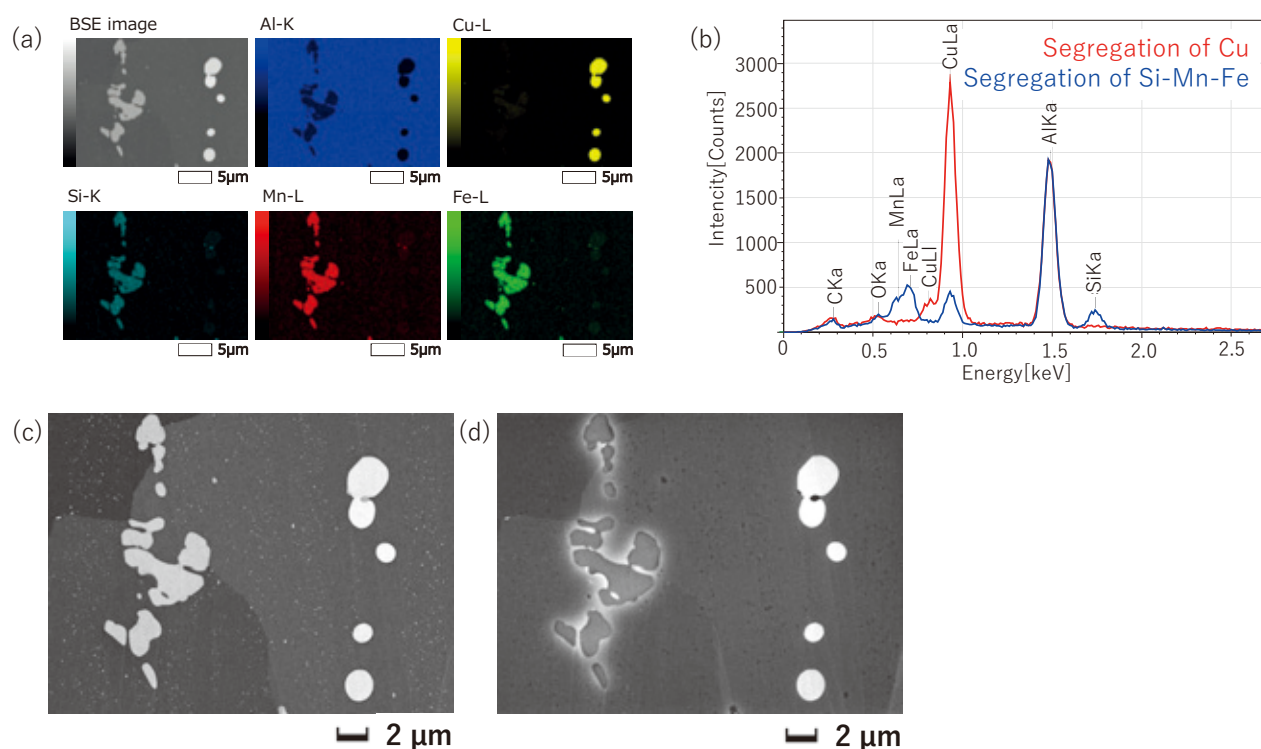
Observation of Boron Nitride by using UHD at an incident voltage of 0.7 kV. (a) In SHL mode and WD 4 mm, the voltage contrast between black and white particles is enhanced. (b) In SHL mode and WD 1 mm, the morphological contrast is enhanced and the voltage contrast is suppressed. (c) In BD mode and WD 2 mm, the morphological contrast is enhanced and the voltage contrast is almost invisible.

**Fig. 10 Observation of acrylic particles by using UHD.**



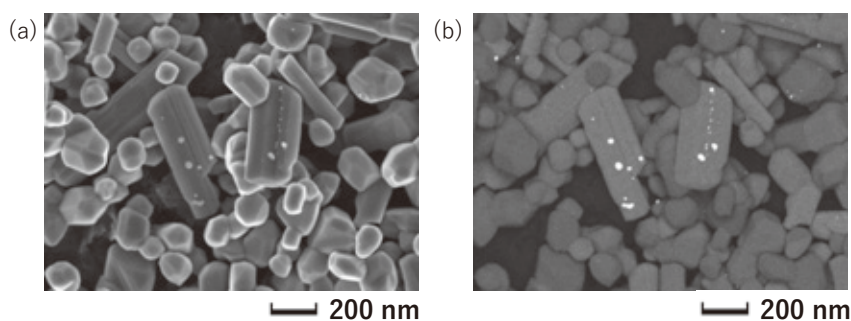
Observation of acrylic particles by using UHD at an incident voltage of 0.7 kV. (a) In SHL mode and WD 4 mm, charging contrast is observed. (b) In SHL mode and WD 1 mm, charging contrast is suppressed. (c) In BD mode and WD 2 mm, the charging contrast disappears.

**Fig. 11 EDS analysis and observation of aluminum alloy by using BED and UHD.**



(a) The BSE image and the EDS elemental maps (measurement time of about 12 minutes) were acquired at an incident voltage of 4.0 kV and a probe current of 3.6 nA. For obtaining these images, we used BED and JED (EDS detector EX-74720U1L5Q manufactured by JEOL Ltd.). In the EDS elemental maps, the segregation parts of Cu and Si-Mn-Fe can be confirmed. (b) EDS spectra of them were extracted from the EDS maps. (c) The BSE image by BED at an incident voltage of 3.0 kV, SHL mode, and WD 4 mm. The compositional contrast is enhanced in the Cu and the Si-Mn-Fe segregation parts. However, it is difficult to distinguish between them. (d) The BSE image by UHD at an incident voltage of 3.0 kV, SHL mode, and WD 4 mm. The voltage contrast between the segregated part of Cu and Si-Mn-Fe is clearly visible.

**Fig. 12 Observation of titanium-oxide particles carrying silver nanoparticle catalysts by using UHD and UED.**



Observation of titanium-oxide particles carrying silver nanoparticle catalysts by using UHD and UED at an incident voltage of 2.0 kV. (a) Surface morphology of titanium-oxide particles observed by using UHD. (b) Compositional contrast of the silver nanoparticle catalysts observed by using UED. At this time, -500 V is applied to the energy filter of UED.

## Summary

In this paper, we explained the various information (surface potential, surface morphology, topography, composition, and crystal orientation) in SEM images depending on the energy and emission angles of electrons emitted from specimens. In addition, we introduced the functions of each detector and observation modes in JSM-IT800 <SHL>. In the observation examples by using each detector, we showed the differences in the images obtained by changing the observation mode and observation conditions for various specimens. JSM-IT800 <SHL> enables us to obtain various information in specimens by properly using the detectors and observation modes.

## References

- [ 1 ] D. Bell, N. Erdman, *Low Voltage Electron Microscopy Principles and Applications*, Wiley (2013).
- [ 2 ] O. Suzuki, M. Inoue, Y. Yamaguchi, Various Analyses of Fine Structures using Multipurpose High Throughput Analytical FE-SEM: JSM-IT800, *JEOL News*, Vol.55, No.1, 49-55 (2020).
- [ 3 ] L. Reimer, *Scanning Electron Microscopy Physics of Image Formation and Microanalysis Second Edition*, Springer (1998).
- [ 4 ] H. Niimi, Y. Sakuda, N. Asano, S. Asahina, Observation and Analysis at Low Accelerating Voltage Using Ultra High Resolution FE-SEM JSM-7900F, *JEOL News*, Vol.54, No.1, 72-82 (2019).

# Preparation of TEM Specimens Having Specific Crystal Orientations Using FIB-SEM and EBSD

## ～Applications to Allende meteorite～

Misumi Kadoi<sup>1</sup>, Masateru Shibata<sup>1</sup> and Ichiro Ohnishi<sup>2</sup>

<sup>1</sup> EP Business Unit, JEOL Ltd. <sup>2</sup> EM Business Unit, JEOL Ltd.

In TEM or STEM observations of micro-crystals or poly-crystals, we need to search for crystalline grains having the primary crystal orientations of the target rather than the random crystal orientations, and, if necessary, we also need to perform specimen tilting and crystal-orientation alignment. These procedures require a significant effort and long hours. To improve this situation, we used a FIB-SEM equipped with an EBSD detector to examine a method to select crystalline grains having specific orientations and then prepare TEM specimens of crystals having the target primary orientations. In our study, we applied the method to Allende meteorite and prepared TEM specimens of olivine grains having the orientations of [100], [010] and [001] from the fine-grained matrix in the meteorite. Our TEM results confirmed that the TEM specimens can be aligned to the target primary orientations with an accuracy of a tilt angle of 5 degrees using the TEM goniometer stage, and they were thin enough to produce good atomic-resolution STEM images. The results suggest that our method is very effective in preparing TEM specimens having specified crystal orientations of the target from not only the matrix of Allende meteorite but also from any specimens composed of various micro-crystals or poly-crystals.

### Introduction

Recent development of the aberration correction technology has enabled us to observe atomic resolution TEM (Transmission Electron Microscope) or STEM (Scanning Transmission Electron Microscope) images for crystalline specimens. However, in order to observe the crystal structure at the atomic level, the electron beam has to be irradiated along the target zone axis of the crystal. If this condition is not satisfied, it is necessary to align the orientations by tilting the specimen using the TEM goniometer stage. In general, the powder or poly-crystal specimens such as ceramics, minerals, and so on, contain randomly oriented many crystalline grains and therefore, specimen tilting and orientation alignment are essential procedures, and require many efforts and long hours. Moreover, if the specimen tilt angle is large, the specimen appears thicker, resulting in degrading image resolution by increased chromatic aberration. To avoid these problems, it is useful to obtain the information on crystal orientations of the specimen before or during the preparation of TEM specimen. This orientation information facilitates preparation of TEM specimen having the primary crystal orientations, thus greatly reducing the efforts and hours for observation steps.

The FIB (Focused Ion Beam) technique irradiates and scans a finely-focused gallium ion beam on the surface of bulk sample to make a specially shaped specimen by ion-sputtering. Since

FIB can prepare the TEM specimen with specific size and thickness from an arbitrary area, this technique is indispensable for the preparation of TEM specimen. Common FIB instrument configuration includes not only an ion gun but also an electron beam gun, called multi-beam or FIB-SEM system. This system can acquire SEM images such as secondary electron image (SEI) and backscattered electron image (BEI). The instrument can observe the surface morphology and Z contrast of the sample to help us prepare a TEM specimen. With detection of secondary electrons which are generated by the interactions between a gallium ion beam and a sample, the FIB is also able to acquire SIM (Scanning Ion-beam Microscope) images. The SIM image is highly sensitive to the surface structure of sample, compared with the SEM image. In addition, the SIM image shows channeling contrast which depends on the crystal orientation, thus providing the relative difference in the orientations among the crystalline grains. However, such information reflects only qualitative one, and thus the SIM image cannot provide detailed and quantitative information on the crystal orientations.

On the other hand, the EBSD (Electron Back-Scatter Diffraction) method is more useful for obtaining precise crystal orientation information. In the method, the electron back-scatter diffraction pattern (Kikuchi pattern), which is formed by the interaction between electron beam and sample, is acquired using a CCD or CMOS camera. Then, we can conduct quantitative

study of the crystal orientation on the sample surface. By combining EBSD with the scanning function of SEM, a two-dimensional (2D) crystal orientation map of the sample surface can be obtained. Furthermore, the incorporation of an EBSD detector into a FIB-SEM can take a three-dimensional (3D) distribution analysis of the crystal orientations by iterative procedures of milling a sample and then acquiring crystal orientation maps for milling surface at the specified interval.

In our study, we used an FIB-SEM system equipped with an EBSD detector. Then, the crystal orientation information on the sample surface was obtained by the EBSD method, followed by preparing TEM specimens having the target primary crystal orientations by the FIB method. This method was applied to the matrix of Allende meteorite and we prepared TEM specimens of olivine grains having the orientations of [100], [010] and [001] for TEM & STEM observations. From the observation results, we confirmed the effectiveness of our method. In this article, we will report the detailed procedures of this method and the results of observing TEM specimens prepared with the method.

## Sample

Allende meteorite was used as a sample for this study (Fig. 1). This meteorite belongs to carbonaceous chondrite, which is one of the groups in stony meteorite. Carbonaceous chondrite has chemical composition similar to that of the solar atmosphere. That is, it contains information on the pre-solar or early process of the Solar System, which was lost in many planets and satellites caused by the geological activities after the formation of those bodies. Therefore, it is regarded to be an important sample to study the formation process of the solid materials in the early Solar System. Allende meteorite consists mainly of mm-sized spherical objects, called as chondrules, and irregular shaped Ca, Al-rich inclusions (CAIs) embedded in the matrix composed of fine grained aggregate of olivine, pyroxene and Fe-Ni oxide/sulfide (Fig. 1). Since the grain sizes of constituent minerals of the matrix are very small (<10 μm in size), there have been only a few studies for these grains compared with chondrules and CAIs.

Ohnishi et al. (2018) reported that very thin plate-shaped precipitates (~1 nm in thickness) are generated in the olivine

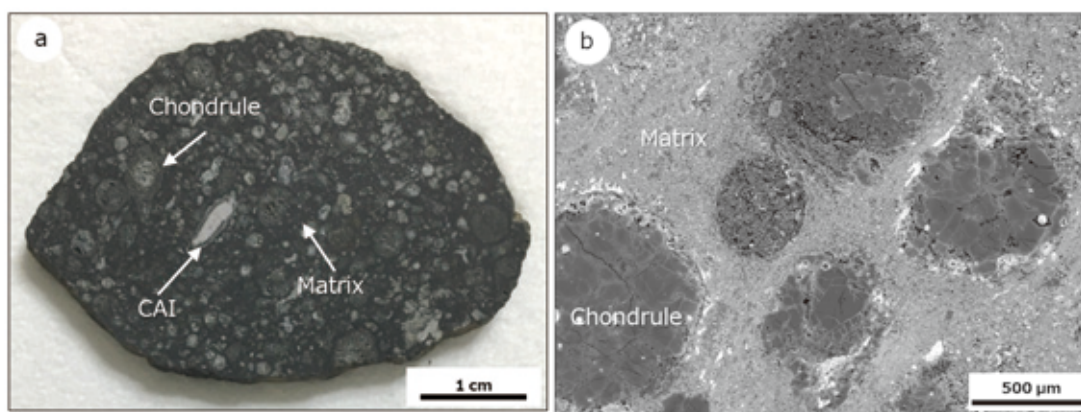
grains from Allende matrix and their long axes are parallel to the (100) plane of the host of olivine. Based on their results, they suggested that the precipitates are Fe, Cr-rich oxides and they were probably formed by the high-temperature oxidation process of olivine [1]. However, it should be noted that the number of olivine grains that they studied is limited and it is still controversial whether the plate-shaped precipitates commonly occur in the matrix olivine. In order to observe the precipitates parallel to the (100) plane, we need to observe them in the specific orientation (for example, [010] or [001]). But the olivine grains are randomly oriented in the matrix and thus, if we study the TEM specimen prepared by using the conventional FIB method or the ion-milling method, many efforts and long hours are required for searching the target grains and the orientation alignment. To overcome this situation, we applied our method to prepare TEM specimens from the matrix of olivine grains in the [001], [010] and [100] orientations and then, we examined whether the precipitates reported in [1] commonly occur or not in olivine grains from the Allende matrix.

For the FIB-SEM observations, we conducted the following two steps. A thick section of Allende meteorite was embedded by conductive resin and the surface of embedded section was mechanically polished. For performing EBSD analysis after these steps, mirror polishing using a colloidal silica was performed to obtain mirror polish of the surface. Furthermore, in order to prevent electrical charging, osmium coating was applied to the mirror polished surface of embedded section.

## Instruments

For EBSD analysis and TEM specimen preparation, we used a JEOL Multi-Beam System, JIB-4700F (Fig. 2) which is equipped with an EDAX DigiView EBSD detector. The JIB-4700F is a FIB-SEM system equipped with both a gallium ion-beam gun and a Schottky electron gun. This system enables us to perform both FIB milling and high spatial-resolution SEM observation and analyses in a single instrument. The JIB-4700F also includes the Picture Overlay function [2] for performing overlay display of an arbitrary image on the FIB image or SEM image. The use of this unique function allows us to provide overlay-displaying the SEM image on the SIM image, leading

**Fig. 1 Optical micrograph of a thick section of Allende meteorite (a) and SEM image obtained from an area of surface of the section (b).**



- (a) Optical reflection image of Allende meteorite. The meteorite is composed of white-colored CAIs and chondrules (a few mm in size), black-colored matrix which fills the gaps among CAIs and chondrules.  
(b) SEM image of Allende meteorite (backscattered electron image). The matrix of aggregated small grains occurs as filling the gaps in chondrules.

to highly precise positional setting of deposition or milling onto the target region. For observing the TEM specimen prepared by FIB milling, a JEOL Atomic Resolution Analytical Electron Microscope, JEM-ARM300F, was used. This microscope is our 300 kV aberration-corrected S/TEM equipped with a cold field emission gun [3-4]. In the JEM-ARM300F, two types of the objective lens pole-pieces; FHP (Full High resolution Pole-piece) for ultra-high resolution imaging and WGP (Wide Gap Pole-piece) for ultrahigh sensitive analysis are selectable. In our study, the microscope equipped with the WGP was used.

## Experimental Results and Discussion

The workflow of preparation and observation of TEM specimens using the method in our study is shown in **Fig. 3**. First, the crystal orientation maps were obtained from the matrix in a thick section of Allende meteorite using the EBSD method, and olivine grains were selected for the preparation of TEM specimens. Next, TEM specimens of the selected grains were prepared with FIB function. At that time, using the Picture Overlay function, the acquired crystal orientation map was overlaid on the SEM image for helping us to determine the milling position, and then electron-beam deposition was applied to this position for preparing TEM specimens. Finally, TEM observations were performed to evaluate the prepared TEM specimens. The following descriptions will show each process of the method in detail.

### Selecting olivine grains for TEM observations

In **Fig. 4(a)** to **(c)**, an SEM image of the matrix of Allende meteorite and crystal orientation maps of olivine grains, which were obtained from the same field of view using the EBSD method, are shown. From **Fig. 4(b)** and **(c)**, it is clearly confirmed that olivine grains in the matrix are randomly oriented. From them, the preparation of TEM specimens for observing the grains having the [100], [010] and [001] orientations was carried out with the following procedures. First, as shown in **Fig. 4(b)**, olivine grains having the [001], [100] and [010] orientations, which are aligned within the tilt angle of 20 degrees in the direction vertical to the polished surface of the sample (Z direction), were selected and colored (**Fig. 5(a)**). The crystal structure of olivine belongs to the orthorhombic crystal system, and thus the [100], [010] and [001] orientations are orthogonal to each other (**Fig. 4(d)**). Therefore, if TEM specimen is prepared for the above-mentioned, selected and colored grains in the direction parallel to the sample surface, it becomes possible to obtain the TEM specimens of olivine grains having the [100], [010] and [001] orientations within at least the tilt angle of 20 degrees. Even if this condition is satisfied, several grains and two kinds of the orientations in the direction parallel to the sample surface become candidates for milling (for example, in the case of grains having the [001] orientation parallel to the Z direction, it is possible to prepare TEM specimens in the two directions of [100] and [010]). From them, we selected grains and directions so that the TEM specimens can be made over the area as large as possible with the FIB milling accuracy. After this selection, we prepared TEM specimen for observing in the [100] direction from the olivine grains having the [001] orientation within the tilt angle of 20 degrees in the Z direction (**Fig. 5(b)**). In the same way, TEM specimen for observing in the [010] direction was prepared from the olivine grains having the [100] orientation (**Fig. 5(c)**), and also for observing in the [001] direction from the olivine grains having the [010] orientation (**Fig. 5(d)**).

### Preparation of TEM specimen by FIB

For the preparation of TEM specimens by FIB, we utilized the bulk pickup method, which uses a pickup tool independent of the FIB system, described as follows. First, a thick specimen block is prepared by FIB milling. This block is mounted onto a TEM grid using the pickup tool. After that, FIB milling is performed again for the preparation of a thin specimen.

The detail procedures of preparation of TEM specimen for observation in the [100] direction of olivine, using the bulk pickup method in our study, are shown in **Fig. 6**. First, electron-beam deposition was performed on the target area (grain) to be milled. Next ion-beam deposition was further performed on the electron-beam deposition area. During the electron-beam deposition on the target area, the Picture Overlay function was used to overlay the crystal orientation map on the SEM image,

**Fig. 2 Appearance of the JIB-4700F**



The JIB-4700F is an FIB-SEM system that is equipped with a gallium ion-beam gun and a Schottky electron gun. The system also includes the 3D observation function. Furthermore, the EDS (Energy Dispersive X-ray Spectroscopy) and the EBSD systems are optionally available, thus utilizing a diversified range of applications.

**Fig. 3 Workflow of preparation and observation of TEM specimens using our method.**

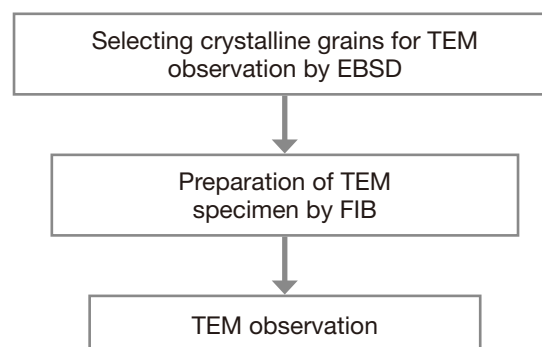


**Fig. 4 SEM image of the matrix of Allende meteorite (a), Crystal orientation map of olivine grains (b), Pole Figures (PF) of the (001), (100) and (010) planes (c), and an ideal crystal structure of olivine (d).**

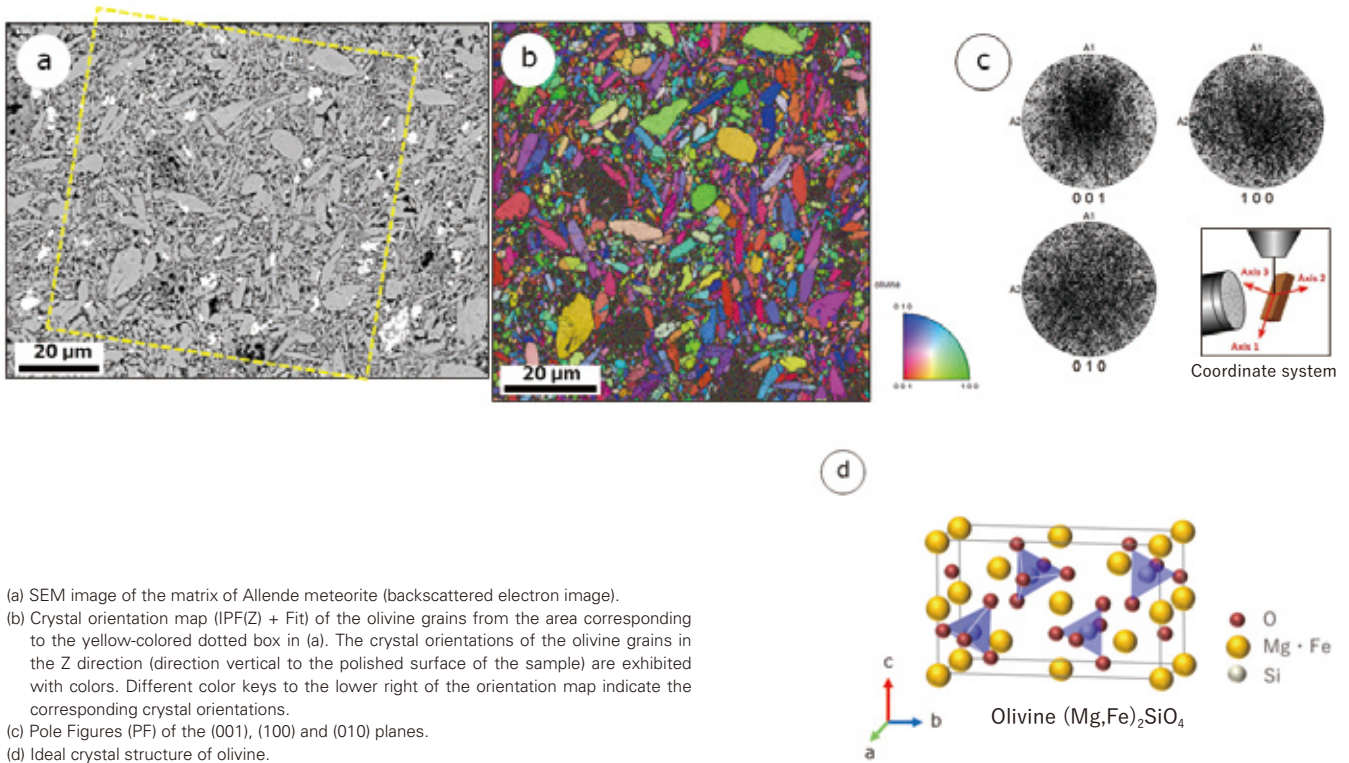
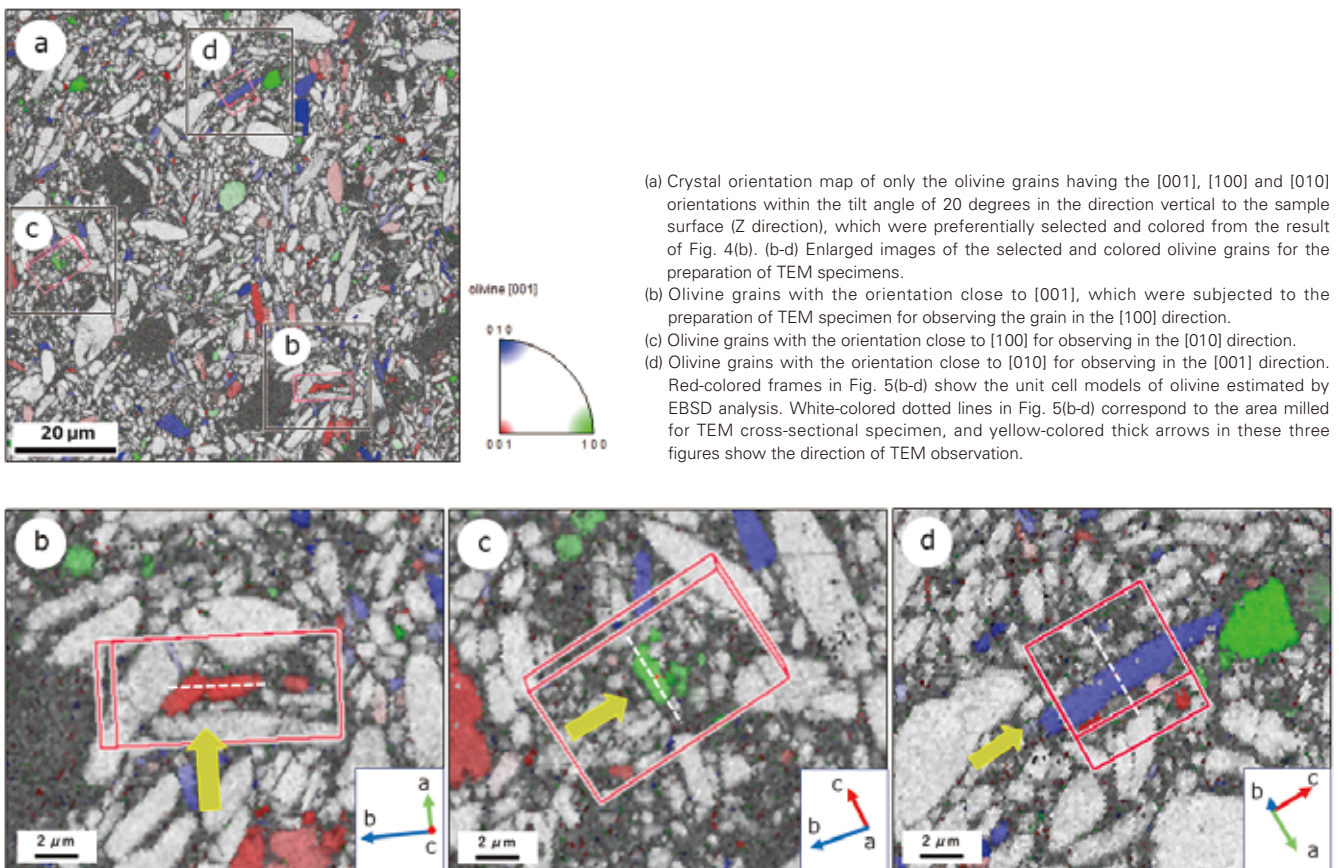


**Fig. 5 Crystal orientation maps of olivine grains selected for the preparation of TEM specimens.**



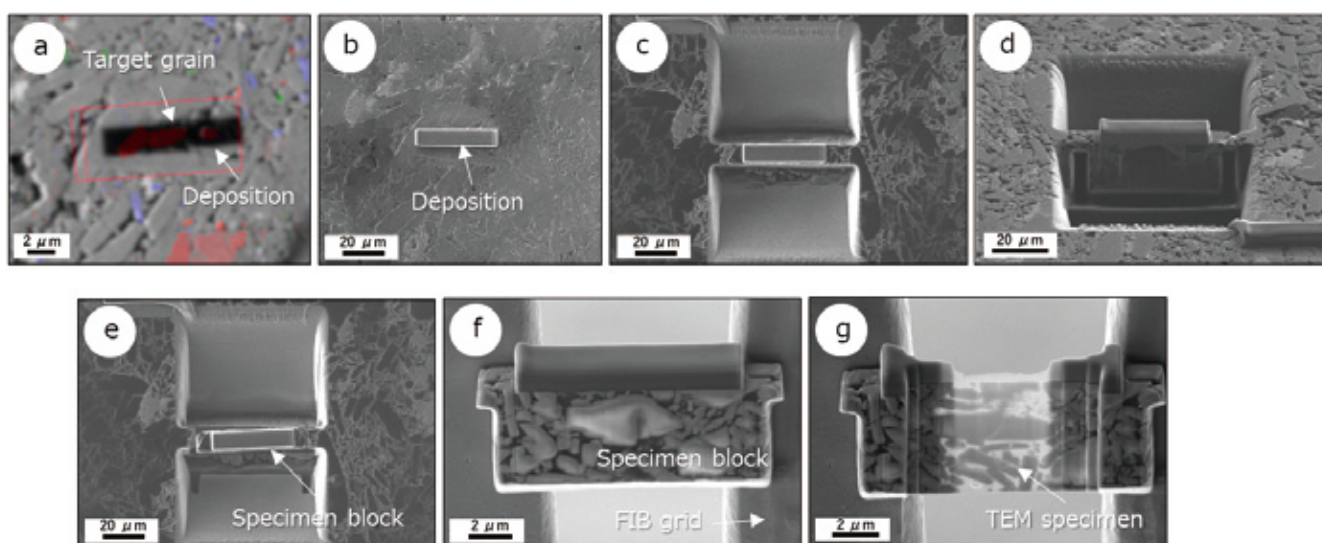
so as to precisely select the grains to be milled and to locate the milling position (Fig. 6(a) and Fig. 7(a), (c)). After the deposition, a specimen block, which included the deposition layer and a part of the sample, was cut out at an accelerating voltage of 30 kV (Fig. 6(c-e)). After that, this chunk was moved to the FIB grid using the pickup tool, and it was mounted on the grid by epoxy resin (Fig. 6(f)). Finally, the chunk mounted on the grid was returned to the FIB system and it was thinned using the ion beam (accelerating voltages: 30 kV and 5 kV). With this procedure, the specimen was thinned down to about 80 nm in thickness, which enables us to perform high-resolution TEM/STEM observations (Fig. 6(g)). With the same procedures, TEM specimens were also prepared for observation in the [010] and [001] directions of olivine (Fig. 7).

### Evaluation of Prepared Specimens Using TEM

TEM specimens prepared by the above-mentioned method were evaluated using TEM. Figure 8 shows the upper Selected Area Diffraction (SAD) patterns and the lower atomic-resolution STEM-HAADF (High Angle Annular Dark Field) images in the [100], [010] and [001] direction of olivine, respectively.

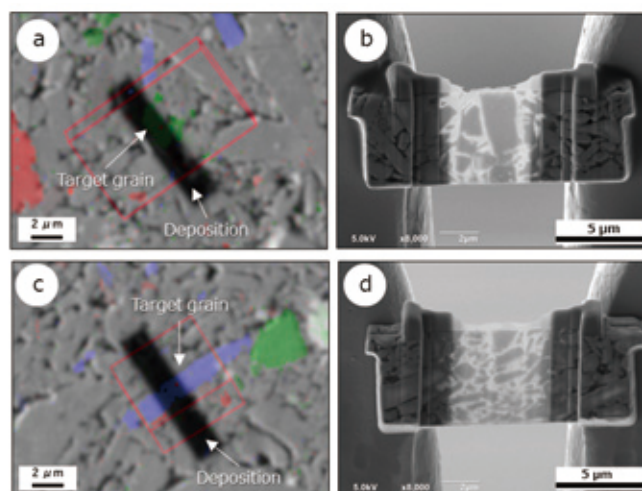
As shown in Fig. 8, atomic-columns were clearly observed in every direction, thus suggesting that all the prepared specimens are thin enough for atomic-resolution observations. From the results of STEM-HAADF observation, we confirmed that plate-shaped precipitates (<1 nm in thickness) occur along the (100) plane of olivine in the [010] and [001] directions of olivine (Fig. 8), while no distinct defects were found in the [100] direction of olivine. These results are consistent with the previous study [1],

**Fig. 6 Secondary electron images of TEM specimen prepared for observation of the [100] direction of olivine.**



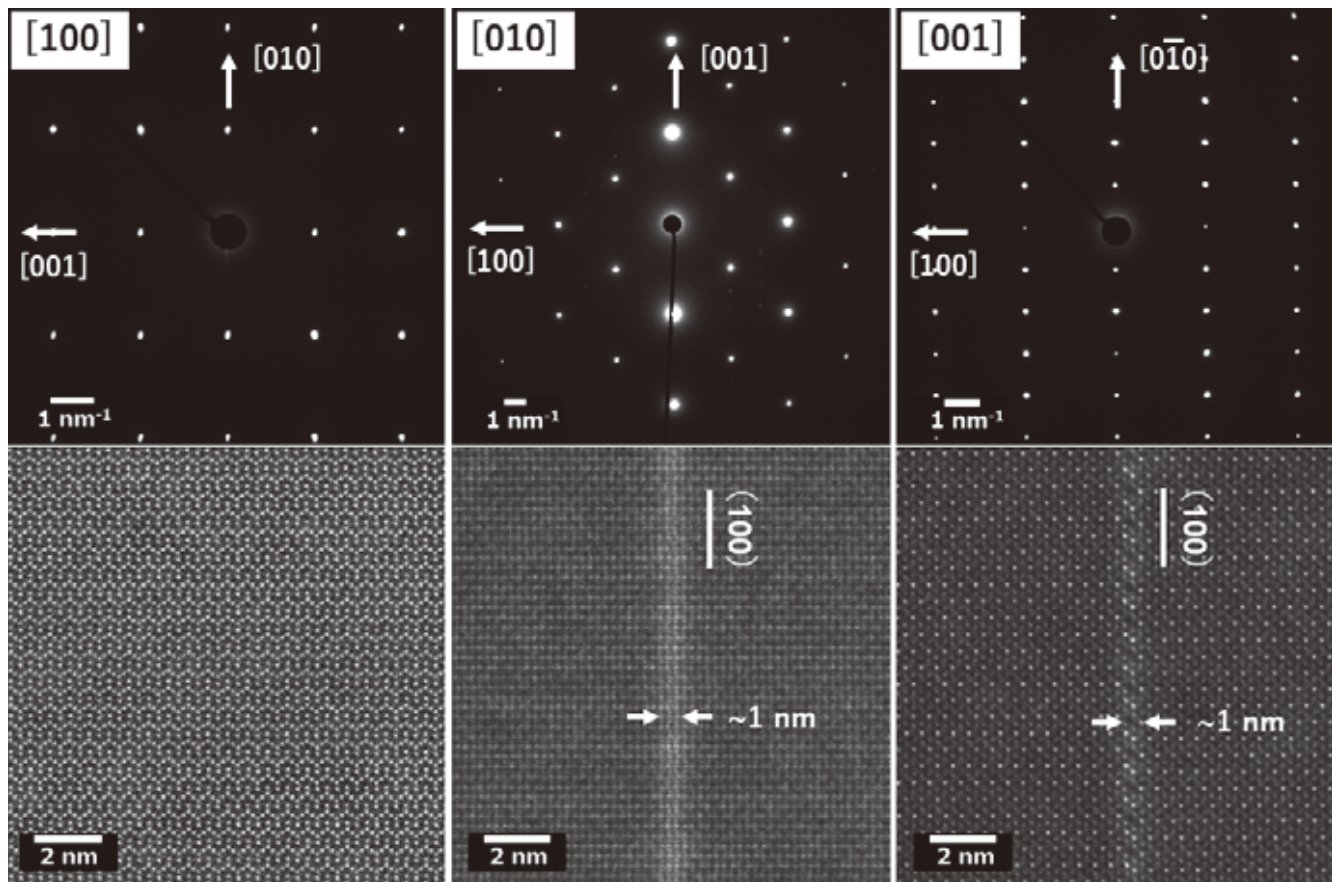
- (a) Electron-beam deposition. Using the Picture Overlay function, the crystal orientation map was overlaid on the secondary electron image to perform the deposition precisely on the target milling position. This image was obtained from the same area as that of Fig. 5(b).  
 (b) Ion-beam deposition directly onto the electron-beam deposition area.  
 (c) FIB milling was performed for both the front and back side of the deposition area to create a hole.  
 (d) The sample was tilted so that it can be observed with the FIB-SEM from the oblique direction, and then the bottom portion of the milled specimen was cut.  
 (e) Both sides of the deposition were cut out to separate a specimen block from the host of the sample.  
 (f) The cut-out block was mounted on the FIB grid.  
 (g) Thin specimen was made by milling the specimen block.

**Fig. 7 Secondary electron images of area of TEM specimens prepared for observation in the [010] and [001] directions of olivine (a, c), and of the prepared TEM specimens (b, d).**



- (a, b) olivine grains for observation in the [010] direction.  
 (c, d) olivine grains for observation in the [001] direction.

**Fig. 8 TEM observation results of the prepared specimens of the matrix olivine in Allende meteorite in the [100], [010] and [001] directions.**



Upper: Selected electron diffraction patterns in each direction. Lower: Atomic-resolution STEM-HAADF images. Instrument: JEM-ARM300F (WGP). Accelerating voltage: 300 kV.

indicating that plate-shaped precipitates might commonly occur in the matrix olivine of Allende meteorite.

Table 1 shows the tilt angles of the TEM goniometer stage when the SAD patterns were obtained in each orientation. These tilt angles were found to be within 5 degrees for all the prepared specimens. The small tilt angle of the stage can be due to the accuracy of the crystal orientation map obtained by the EBSD method, the FIB milling accuracy for the bulk pickup, the precision for mounting the specimen on the FIB grid and for thin specimen milling, the errors in loading the FIB grid on TEM specimen holder, etc. We successfully achieved the tilt angle of the TEM stage within 5 degrees under any conditions. This result suggests that our method described in this article is very effective for preparation of TEM specimens having the target primary orientations, where EBSD and FIB are combined.

## Summary

In our study, we examined a method which combines EBSD and FIB-SEM, for preparing TEM specimens with specific crystal orientations and applied the method to the matrix of Allende meteorite. From the results, we confirmed that our method enables us to prepare TEM specimens having the specific orientations with high accuracy. That is, by using this method, the TEM specimens of olivine grains with [100], [010] and [001] orientations were prepared within the accuracy of tilt angle of 5 degrees using the TEM goniometer stage.

In the preparation of TEM specimens with FIB, the selection

**Table 1 Tilt angles of TEM goniometer stage when the selected electron diffraction patterns in Fig. 8 were obtained.**

		TEM specimen		
		[ 100 ]	[ 010 ]	[ 001 ]
Tilt	X	-1.7	-3.5	+3.4
	Y	+2.6	+2.7	-0.5

of the target crystalline grains by using the EBSD method greatly reduces the efforts and hours required to find the target crystal and adjust the crystal orientation to a specific direction in the TEM observation steps. Thus, it is suitable to apply our method not only to the matrix of Allende meteorite, but also to the powder specimens (ceramics, minerals, etc.) or the polycrystal specimens composed of randomly oriented grains.

## References

- [ 1 ] I. Ohnishi, et al. (2018) *81st Annual Meeting of The Meteoritical Society* 6105.
- [ 2 ] Y. Ikeda, *TEM Users Meeting 2014* abstract (in Japanese).
- [ 3 ] H. Sawada, et al. (2014) *JEOL News* vol.49 p.51-58.
- [ 4 ] E. Okunishi, et al. (2015) *JEOL News* vol.50 p.58-63.

# Chemical Bonding State Analysis of Boron and Phosphorus Compounds by Soft X-ray Emission Spectroscopy and Electronic Structure Calculations

Shogo Koshiya, Takanori Murano, Masaru Takakura and Hideyuki Takahashi

SA Business Unit, JEOL Ltd.

The spectra of characteristic X-rays obtained using a soft X-ray emission spectrometer and appropriately selecting X-ray lines of the elements show fine structures that reflect the chemical bonding state of the specimen. It is said that the bonding state is closely related to the physical properties of the specimen, and is suitable for material evaluation. There are several methods to interpret the spectra reflecting the bonding state. In this paper, theoretical calculations (first-principles electronic structure calculations) were used. We present the results of our attempt to interpret the fine structure of the soft X-ray spectra of various boron and phosphorus compounds by comparing the measured soft X-ray emission spectra with the calculated electronic structure (density of states).

## Introduction

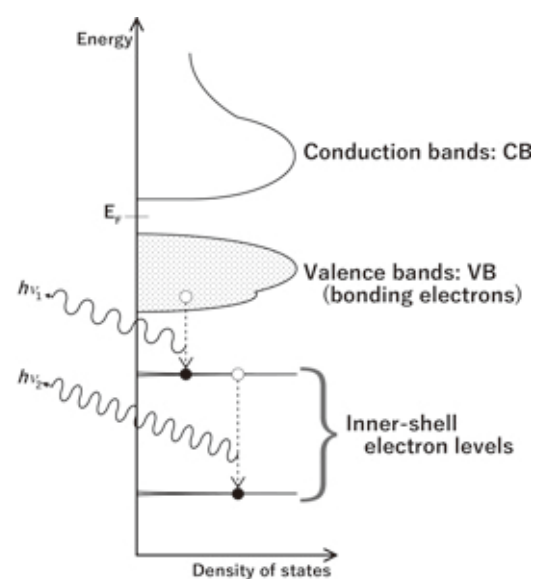
In materials research and development, obtaining information on the valence electrons of a target material is one of the most important ways to understand its physical properties. In general, valence electrons are the outermost electrons. In the case of boron (B, atomic number 5) as an example, the electron configuration is K-shell  $1s^2$ , L-shell  $2s^2, 2p^1$ , and the valence electrons are those in the L-shell. Unlike the inner-shell electron level, which has a symmetrical electronic structure with an energy width of a few eV, the valence band (VB) formed by the valence electrons has a width (energy band) of about 10 eV. The electronic structure of the VB has a fine structure that reflects the bonding state of the valence electrons.

There are several methods to obtain information on the VB. In this paper, we will focus on soft X-ray emission spectroscopy (SXES) by electron beam excitation. When a specimen is irradiated with an electron beam having energy sufficiently higher than the binding energy of the inner-shell electron levels (accelerated by a voltage higher than the critical excitation voltage), the electrons in the specimen are excited and then the vacancies are created. An electron of a lower binding energy level transitions into this vacancy. And then, characteristic X-rays of the energy difference are emitted (**Fig. 1**). The spectrum of these characteristic X-rays can be regarded as a convolution of the electronic structures of the vacancy created electron level and the transition electron belonged level. If the electron transition is between a vacancy in the inner-shell and an electron in the VB, the characteristic X-ray ( $h\nu_1$  in Fig. 1) spectrum reflects the electronic structure (density of states; DOS distribution) of the VB. In this case, the electronic transitions

follow the dipole selection rule. The component of a particular electron orbital in the VB appears in the spectral profile.

In the soft X-ray region (in this paper, it refers to the energies from 50 to 2,300 eV, which is the detectable energy range of

**Fig.1 Schematic diagram of electron transitions in X-ray emission.**



$h\nu_1$ : VB to inner-shell level,  $h\nu_2$ : inner-shell to inner-shell level.

our spectrometer), characteristic X-rays associated with electron transitions between the VB and the inner-shell level of light elements up to third period and transition-metal elements in fourth and fifth periods are contained. The electronic structures of the VB involve information on the bonding states with neighboring atoms, and thus the spectral profile indicates complicated structures. There are several ways to interpret the spectra. The so-called fingerprinting method, which compares the spectra with those obtained from reference materials, is often used. For a more detailed interpretation, it is useful to compare the spectra with electronic structures obtained by theoretical calculations, as is the case with other spectroscopic methods.

We have developed a soft X-ray spectrometer with Terauchi *et al.* in the JST project from 2008 to 2012 [1]. Since 2013, the commercial soft X-ray emission (SXE) spectrometers [2] developed based on this technology, have been provided. The lineups of SXE spectrometer are SXES-LR (SXE spectrometer lower-energy range; SS-94000SXES, detectable energy range: 50 - 210 eV) and SXES-ER (SXE spectrometer extended energy range; SS-94040SXSER, detectable energy range; 100 - 2300 eV). They can be attached to our electron probe micro analyzer (EPMA) and field emission scanning electron microscope (FE-SEM). As for EPMA, a product that can be attached to the EDS port is currently under development. The spectrometer is a wavelength-dispersive type using an aberration-corrected varied-line-spacing concave grating. The back-illuminated type CCD detector makes it possible to acquire characteristic X-rays spectra of multiple elements at once with high sensitivity and high energy resolution. The SXES Handbook [3] is a collection of spectra of reference specimens acquired using these spectrometers, and the principles and measurement examples of SXES are also explained.

In this paper, we compare the measured SXE spectra of various boron and phosphorus compounds with the electronic structures (DOS distributions) obtained from theoretical calculations, and present the results of our attempt to interpret the fine structure of the spectra.

## Experiment

The SXES apparatus used for the experiments was an SXES-LR attached to an EPMA (JEOL JXA-8530FPlus, JXA-iHP200F). The grating used was JS200N (detectable energy range: 70 - 210 eV). The accelerating voltage and the probe current were set at 2 - 5 kV and 7 - 100 nA, respectively, depending on the specimen to avoid the electron irradiation damage. The exposure times were set 4 - 15 min in total to obtain spectra with sufficient S/N. The boron compound specimens were borosilicate glass, which contains 14.9% boron oxide ( $B_2O_3$ ), hexagonal boron nitride (*h*-BN), and cubic boron nitride (*c*-BN). The phosphorus compounds were gallium phosphide (GaP), aluminum phosphate ( $AlPO_4$ ), fluorapatite ( $Ca_5(PO_4)_3F$ ), and black phosphorus (P). The electronic structure calculations were performed using commercial WIEN2k program package [3]. The crystal structure models used were those available in the crystal structure database [4].

## Results and Discussion

### 1. Measured SXE spectra of boron compounds

The B K-emission spectrum is the emission of an electron transition from 2p orbital of the VB to the 1s vacancy in the inner-shell created by electron irradiation. This spectrum reflects the p-orbital electronic structure of the VB of B.

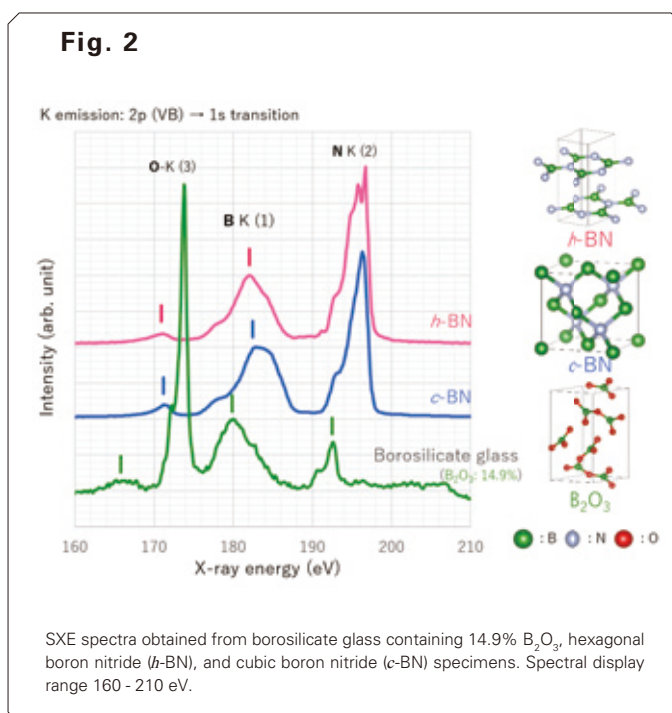
**Figure 2** shows the SXE spectra obtained from the specimens and corresponding crystal structure models (the crystal structure models were drawn by VESTA [6]). The horizontal axis is the X-ray energy and the vertical axis is the intensity. The structure indicated by the vertical line ( | ) corresponds to the characteristic X-ray of B. In all the spectra, the main structure of B is observed from 177 to 187 eV. The spectrum of borosilicate glass specimen indicates additional structures around 165 and 192 eV. The structure around 174 eV originates from O. In the spectra of boron nitride (BN) specimens, the structure around 171 eV originates from B and the structures around 196 eV originates from N. The *h*-BN and the *c*-BN are crystal polymorphs with different structures (hexagonal and cubic), i.e., different bonding states. Therefore, their spectral profiles around 182 and 195 eV are different. It can be seen that the spectral profiles are different depending on the containing elements and the crystal structures. In these spectra, there are O K-emission and N K-emission structures, which are higher-order diffraction lines. They are observed because a wavelength-dispersive spectrometer was used.

### 2. Interpretation of the spectral profiles of boron compounds by electronic structure calculations

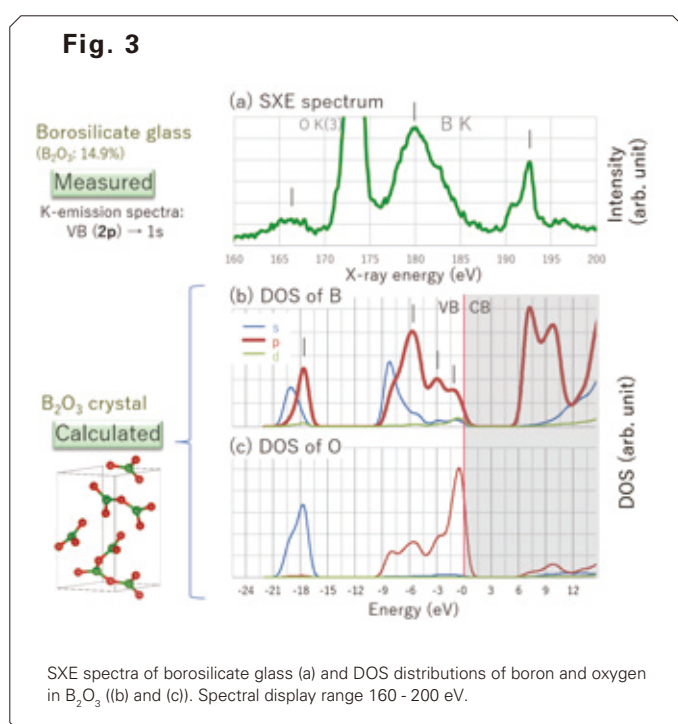
Here, to interpret the experimentally obtained SXE spectra, we performed the electronic structure (DOS distribution) calculation using the WIEN2k program package [3]. This program uses an all-electron calculation method based on the density functional theory, which is widely used to interpret electron energy-loss spectra (EELS) and X-ray spectra, etc. Precisely, the orbital relaxation due to the inner shell vacancies in the excited state must be considered in the X-ray emission. But for simplicity, we calculated the ground state (no vacancies) [7]. The DOS distributions obtained by the following calculations are broadened according to the energy resolution of the spectrometer.

#### 2-1. The case of borosilicate glass

**Figure 3** shows the SXE spectrum obtained from borosilicate glass (a) and the DOS distributions of boron (B) and oxygen



(O) in  $B_2O_3$  ((b) and (c)) obtained by calculation. In the program used in this paper, the calculation cost (required calculation time and computer performance) for the amorphous material is enormous. Therefore, we calculate the  $B_2O_3$  crystal, which is a component of the specimen and can give a comparable spectrum with the obtained one. In the calculation results shown in Figs. 3(b) and 3(c), the vertical axis is the energy. 0 eV means the upper end of the VB. Below 0 eV corresponds to the VB, and above 0 eV corresponds to the conduction band (CB). The vertical axis is the DOS (number of states per unit energy), and s, p, and d indicate the component of each electron orbital (partial DOS; pDOS). The results of the calculations shown in the following sections are presented in the same format. Here, the fine structure of DOS distribution (around -1 to -3 eV in Fig. 3(b)) is not clearly observed in the measured spectra. This is probably due to the fact that the periodic structure of  $B_2O_3$  is not maintained in the measurement area (electron irradiation area)



because the specimen is amorphous.

In the case of K-emission (2p  $\rightarrow$  1s transition), the pDOS distribution of p-orbital electrons in the VB region is compared with the spectral profile derived from the selection rule. It can be seen that the calculation result in Fig. 3(b) reproduces well the peak positions and structures around 180 eV and 167 eV of the SXE spectrum in Fig. 3(a). The peak around 167 eV can be explained by the hybrid orbital of B and O. Because, the calculation results (Figs. 3(b) and 3(c)) indicate the presence of pDOS of B p and O s around -18 eV, this region corresponds to the 167 eV peak of the spectrum.

On the other hand, the structure around 190 - 194 eV is not observed in boron nitride. This structure was a shake-up emission reported by Muramatsu *et al.* [8]. The process can be understood as follows.

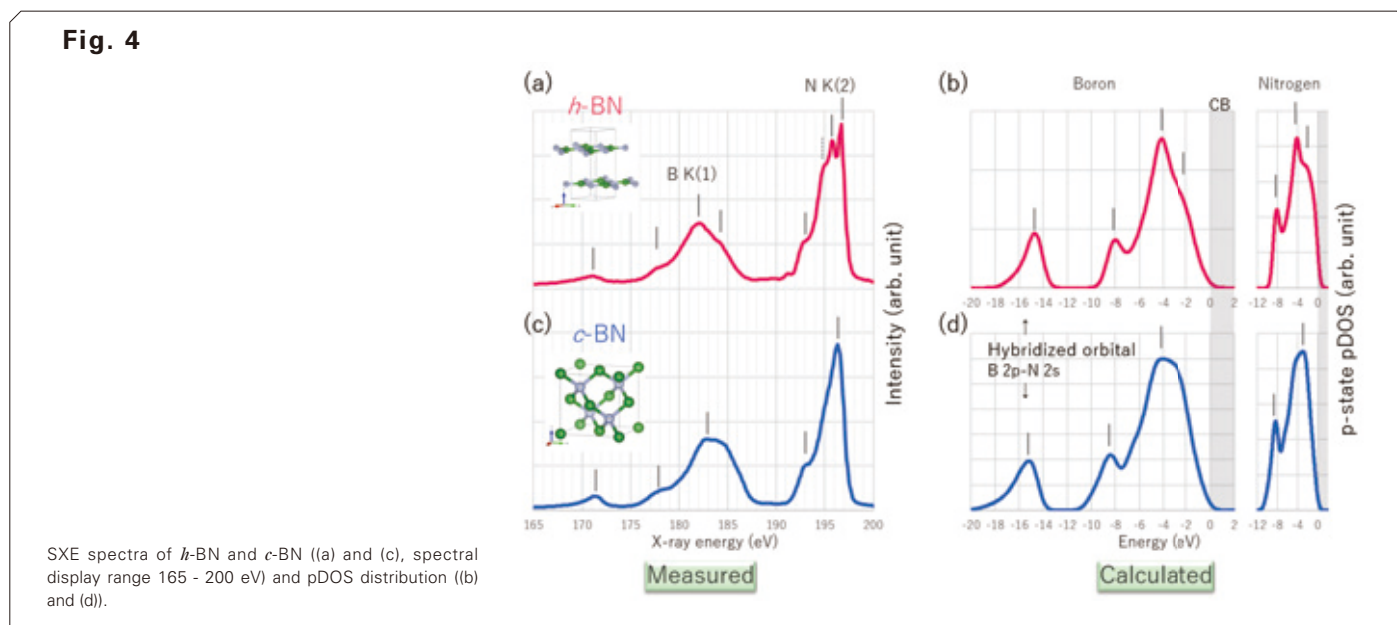
1. When inner-shell electrons are emitted from the specimen, inelastic collisions excite electrons in the VB into the antibonding orbital (conduction band).
2. The excited electron and the vacancy in the inner-shell form an exciton.
3. In the exciton relaxation process, X-rays are emitted when the excited electron transitions to the inner-shell vacancy.

In the calculation results, the antibonding orbitals correspond to the DOS distribution around +6 - +12 eV (CB region) in Fig. 3(b). Since the emission goes through an intermediate state, it is necessary to incorporate the excited state to reproduce this peak shape by calculation. For example, in the core-loss spectra of EELS, the ground state calculations do not match the experimental results. This is due to the presence of vacancies in the inner-shell electron levels at the final state, so the excited state must be considered.

As shown above, we were able to obtain information on the origin of the peak positions and structures of the measured spectra by comparing them with the calculated results. This result shows the effectiveness of using electronic structure calculations for the interpretation of SXE spectra.

## 2-2. The case of boron nitride

Next, we will introduce boron nitride compounds. **Figure 4** shows the SXE spectra of *h*-BN and *c*-BN ((a) and (c)) and the pDOS distributions of the boron (B) and nitrogen (N) p-components ((b) and (d)). The N K-emission spectra (Figs. 4(a) and 4(c))



are the second-order diffraction line and the energy are half of the first-order line. The horizontal axes of N pDOS (Figs. 4(b) and 4(d)) are reduced to match the scale. In the B K-emission spectra, the structure around 184 eV is different between Figs. 4(a) and 4(c) due to its crystal structure. It is attributed to the difference in the electronic structure at the upper end of the VB, as shown in the calculation results. Although the calculation results are not shown here, the structure around 171 eV is a hybrid orbital of B p and N s. The calculation results for N K-emission also reproduce the peak position well. But the profiles of *h*-BN around 196 and 197 eV are different between experiment and calculation. Here, we will discuss this difference.

**Figure 5(a)** shows an anisotropic crystal structure of *h*-BN. The six-membered rings of boron and nitrogen in the *a*-*b* plane are stacked in the *c*-axis direction (lattice direction [0001]). In such a case, it is well known that the X-ray emission intensity also becomes anisotropic [9]. As shown in Fig. 5(b), the orbital components contributing to the emission differ depending on the crystal orientation and the position of the detector (in practice, the detector position is fixed and the specimen is tilted and rotated). Figures 5(d) and 5(f) show the pDOS, where the p component is divided into  $p_x$ ,  $p_y$ , and  $p_z$  orbital components. In this case, the  $p_z$  orbital component contributes to the emission intensity when the *c*-axis is parallel to the detector plane (Fig. 5(b) position<sub>∥c</sub>). On the other hand, the  $p_x$  and  $p_y$  orbital components contribute to the emission intensity when the *c*-axis is perpendicular to the detector plane (Fig. 5(b) position<sub>⊥c</sub>). The spectral intensities in Figs. 5(c) and (e) show that the intensity derived from the  $p_z$  component is strong. Therefore, the *c*-axis of the specimen is nearly parallel to the detector. Furthermore, the crystal orientation of the specimen can be analyzed by using spectrum deconvolution. We do not describe the details of the analysis here, but please refer to the SXES Handbook [2] for a practical example.

### 3. SXE spectra of phosphorus compounds and interpretation by electronic structure calculations

Finally, examples of phosphorus compounds are presented. **Figure 6** shows SXE spectra (a), crystal structure models (b), and electronic structure calculations (c) obtained from various phosphorus compounds (gallium phosphide (GaP), aluminum

phosphate (AlPO<sub>4</sub>), fluorapatite (Ca<sub>5</sub>(PO<sub>4</sub>)<sub>3</sub>F), and black phosphorus (P)).

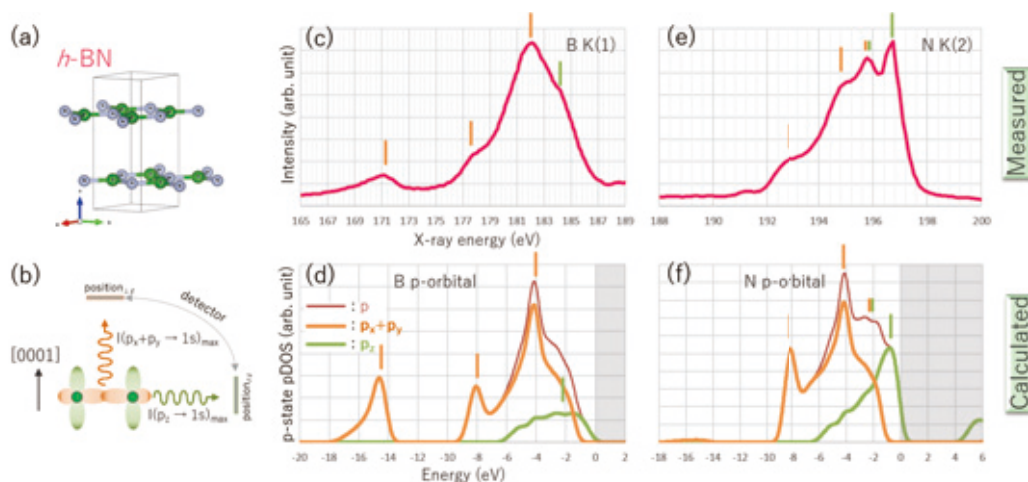
In the SXE spectrum (Fig. 6(a)), the structure between 111 and 130 eV is P L-emission. They are the emissions of the transition from M-shell electron to vacancies in 2p level (L<sub>2,3</sub> shell). From the selection rule, it can be said that electrons in the s and d orbital components of the VB contribute to the L-emission. Thus, the results of the electronic structure calculation (Fig. 6(c)) show the s, d, and s + d pDOS of phosphorus (P). As in the case of boron compounds, the calculated results for all compounds reproduce well the peak positions and structures observed in the SXE spectra.

In isolated atoms, the electronic configuration of phosphorus is K-shell 1s<sup>2</sup>, L-shell 2s<sup>2</sup>, 2p<sup>6</sup>, M-shell 3s<sup>2</sup>, 3p<sup>3</sup>, and the 3d orbital is empty. At first glance, it may seem strange to show the d-orbital component in the calculation results. However, when atoms bond with each other to form a solid, they form a band structure (VB and CB), which results in a different electronic structure from that of isolated atoms. As a result, if we consider that a component with d-orbital symmetry appears among the electrons in the VB, the calculation results can be smoothly accepted. In fact, the structure of AlPO<sub>4</sub> and Ca<sub>5</sub>(PO<sub>4</sub>)<sub>3</sub>F around 126 eV is due to the d-orbital component caused by the hybridization with the p-orbital of the neighboring O. By including this component, the measured spectra can be interpreted. Besides, the crystal structure near the P atom in AlPO<sub>4</sub> and Ca<sub>5</sub>(PO<sub>4</sub>)<sub>3</sub>F has a similar structure as that of PO<sub>4</sub> in Fig. 6 (b). As a result, similar structures are observed in the spectra and calculation results.

## Conclusion

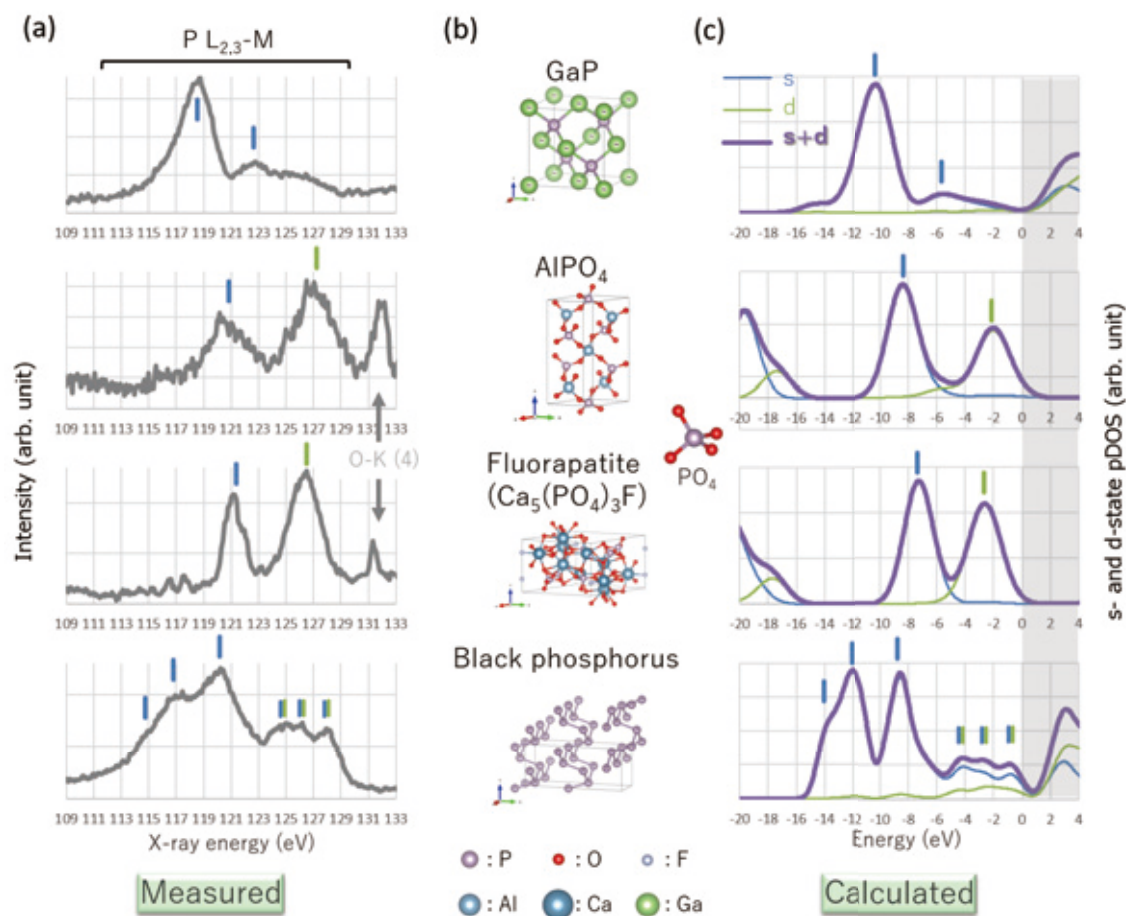
In this paper, we discuss the comparison between measured SXE spectra and theoretical calculations. It is shown that the ground state calculation is sufficient for qualitative comparison and that the electronic structure calculation results reproduce the experimental data well. It should be noted that the calculated results (pDOS in the VB) and the SXE spectra are not identical, since the actual SXE spectra are generated by electronic transitions between two levels. Nevertheless, theoretical calculations are one of the effective means for spectral interpretation.

**Fig. 5**



Crystal structure model of *h*-BN (a) and schematic diagram of anisotropic K-emission (b), SXE spectra (c) and (e), and pDOS distribution of p-component (d) and (f).

Fig. 6



SXE spectra (a) (spectral display range 109 - 133 eV), crystal structure models (b) and pDOS distributions (c) obtained from various phosphorus compounds.

## Acknowledgments

Some of the theoretical calculations presented in this paper were performed in collaboration work with Professor Masami Terauchi at Institute of Multidisciplinary Research for Advanced Materials, Tohoku University. The authors would like to thank him for useful discussion of the calculation results.

## References

- [ 1 ] M. Terauchi, H. Takahashi, N. Handa, T. Murano, M. Koike, T. Kawachi, T. Imazono, M. Koeda, T. Nagano, H. Sasai, Y. Oue, Z. Yonezawa, S. Kuramoto, "Ultrasoft-X-ray emission spectroscopy using a newly designed wavelength-dispersive spectrometer attached to a transmission electron microscope", *J. Electron Microsc.* **61**, 1 (2012). etc.
- [ 2 ] H. Takahashi, T. Murano, M. Takakura, S. Asahina, M. Terauchi, M. Koike, T. Imazono, M. Koeda and T. Nagano, "Development of soft X-ray emission spectrometer for EPMA/SEM and its application", *IOP Conf. Ser.: Mater. Sci. Eng.* **109**, 012017 (2016). etc.
- [ 3 ] M. Terauchi, H. Takahashi, M. Takakura, T. Murano and S. Koshiya, "Handbook of Soft X-ray Emission Spectra Version 6.0 (Sep. 2020)".  
[https://www.jeol.co.jp/download\\_soft\\_x-ray.html](https://www.jeol.co.jp/download_soft_x-ray.html)
- [ 4 ] P. Blaha, K. Schwarz, F. Tran, R. Laskowski, G.K.H. Madsen and L.D. Marks, "WIEN2k: An APW+lo program for calculating the properties of solids", *J. Chem. Phys.* **152**, 074101 (2020).
- [ 5 ] Y. Xu, M. Yamazaki, and P. Villars, "Inorganic Materials Database for Exploring the Nature of Material", *Jpn. J. Appl. Phys.* **50**, 11RH02 (2011).
- [ 6 ] K. Momma and F. Izumi, "VESTA 3 for three-dimensional visualization of crystal, volumetric and morphology data", *J. Appl. Crystallogr.* **44**, 1272 (2011).
- [ 7 ] J. Kawai, I. Tanaka and H. Adachi, "Profile changes of X-ray spectra and their interpretation using the molecular-orbital method", *BUNSEKI KAGAKU* **44**, 251 (1995).
- [ 8 ] Y. Muramatsu, H. Takenaka, T. Oyama, T. Hayashi, Melissa M. Grush and Rupert C. C. Perera, "Valence Band Structure and Decay Process in the Inner-Shell Excitation of Boron Oxide", *X-Ray Spectrom.* **28**, 503 (1999).
- [ 9 ] W. Heitler, "THE QUANTUM THEORY OF RADIATION", (DOVER PUB. INC., New York), 173-181 (1953).

# Chemical State Analysis of Fe in the Matrix of the Allende Meteorite Using an FEG EPMA and SXES

Takaomi D. Yokoyama SA Business Unit, JEOL Ltd.

The combining of a field emission EPMA and a Soft X-ray Emission Spectrometer (SXES) provides a useful method to analyze the chemical states of elements in bulk samples with fine textures ( $\mu$  to sub  $\mu$  scale). In this paper, we will introduce a sequential method that includes electron image observation, determination of the mineral grains to be analyzed, quantitative analysis using WDS and chemical state analysis using the SXES. Determination of the desired analytical positions was conducted by backscattered electron observation and real time EDS mapping overlaid on the electron image. Grains of olivine, and the so named "Ca-rich objects" from the matrix of the Allende meteorite were selected for analysis. Next, quantitative analysis by WDS was performed, and each mineral was classified by its chemical composition. We examined the fitting method for Fe *L*-emission spectra obtained by the SXES-ER to read out quantitative peak position energies and signal intensity ratios. Reproducibility of the acquisitions of the Fe *L*-emission spectra was enough to observe differences of each mineral grain.

## Introduction

An electron probe micro-analyzer (EPMA) is a specialized SEM for X-ray spectroscopy using a focused and; accelerated electron beam, for excitation of the sample. The EPMA provides: qualitative, quantitative, X-ray maps, and line scan analyses for elements in a solid material, on micron to sub-micron scale, along with high resolution SE and BSE imaging. The FEG EPMA has the spatial resolution well into the sub-micron. It is also possible to analyze and map a wide area of several  $\text{cm}^2$ , and it is industrially invaluable tool for evaluation and analysis of material structures by measuring the distribution and diffusion of elements in solid materials. Furthermore, it is widely recognized as a major analytical tool for earth and planetary sciences including mineralogy and petrology. The EPMA has multiple wavelength dispersive X-ray spectrometers (WDS), which can measure elements from beryllium to uranium on the periodic table with a high energy resolution.

Recently, JEOL developed a new type of Soft X-ray Emission Spectrometer (SXES) for a new type of X-ray spectroscopy [1]. The SXES disperses X-rays emitted from sample surface using a fixed position, varied line spacing grating, with detection of low energy (soft) X-rays using a back-illuminated CCD camera. The SXES has a very high energy resolution compared to commonly used energy dispersive X-ray spectrometer (EDS). It is possible to take a stable spectrum in a much shorter time than WDS because no mechanical movement (crystals and counters) of the spectrometer is needed and it collects X-rays from the entire energy range (much like EDS). Hence, SXES measurement simultaneously includes the energy range of multiple elements

with high energy resolution, and the image holds spectral information of each measurement point, allowing hyperspectral mapping. Chemical state analysis using electron excited characteristic X-ray is significantly improved with the SXES.

The Allende meteorite is a CV type carbonaceous chondrite, which is considered to be a carbon-rich asteroid-derived meteorite that has been attracting attention with the sample return mission by Hayabusa 2 in recent years. The matrix (groundmass) of the Allende meteorite is an aggregate of fine-grained minerals about a few  $\mu\text{m}$  to few tens of  $\mu\text{m}$ . Iron (Fe) exists universally in various chemical forms everywhere on the Earth and in the Solar System. The chemical state of Fe in the minerals provides essential information for estimating the change in redox state during formation and the chemical composition of the substance of origin. In this study, we would like to introduce an application example for obtaining information on the Fe chemical states of Fe from fine single particles, like the matrix mineral of meteorites, as a useful technique for earth and planetary sciences. The determination of the Fe oxidation states using Fe *L*-emission spectra obtained with an EPMA has been ongoing since the 1970's [2]. Currently, it is mainly used as a method which can determine the Fe oxidation number of Fe oxide and garnet type minerals. Fe *L*-emission spectra reported to date are indicating that the tendency of a higher peak energy and lower  $L\beta/L\alpha$  ratio are dependent on the abundance ratio of trivalent Fe [3, 4]. In this paper, we report the classification by quantitative analysis of the meteorite matrix minerals using an FEG EPMA with an SXES-ER technique, and show the reproducibility of the Fe *L*-emission spectrum from a single mineral particle and the difference between the minerals.

## Experimental

The Allende meteorite is very fragile. Therefore, polishing with sandpaper or diamond paste may cause structures to get plucked, or removed. A more advanced polishing technique is required to create a flat analytical surface without damaging the sample. In this study, the sample was cut using a low-speed precision cutting machine (Buehler IsoMet) with a width of about 8 mm, a height of about 10 mm and a thickness of about 2 mm. The analytical surface was then prepared by milling with a defocused Ar<sup>+</sup> ion beam using the CROSS SECTION POLISHER™ (JEOL).

The quantitative analysis and Fe chemical state analysis were conducted with an FEG EPMA (JXA-iHP200F integrated Hyper Probe, JEOL), combined with a Soft X-ray Emission Spectrometer-Extended Range (SXES-ER). The JXA-iHP200F is a high spatial resolution EPMA equipped with an “in-lens” Schottky type field emission (FE) electron gun and is suitable to analyze samples with micron to sub-micron structures like the meteorite matrix. This EPMA uses an automatically acquired image, when the sample holder is placed into the airlock, for stage / sample navigation, along with the EDS LiveAnalysis and LiveMap functions that display the elemental analysis with EDS in real time when observing the electron image making it easy to find the mineral structure of interest or determine the analysis field. Currently, there are two types of SXES. The SXES-LR has an energy range of 50-210 eV and SXES-ER has an energy range of 100-2300 eV. In this study, we used the SXES-ER which can measure L-emission spectra of the transition metals. An image of the JXA-iHP200F with a JEOL EDS and an SXES-ER is shown in Fig. 1. The current EPMA (JXA-iSP100 and JXA-iHP200F) can be equipped with up to 5 WDSs, an EDS, a hyperspectral CL and an SXES in a single instrument allowing simultaneous collection of data.

Fig. 1

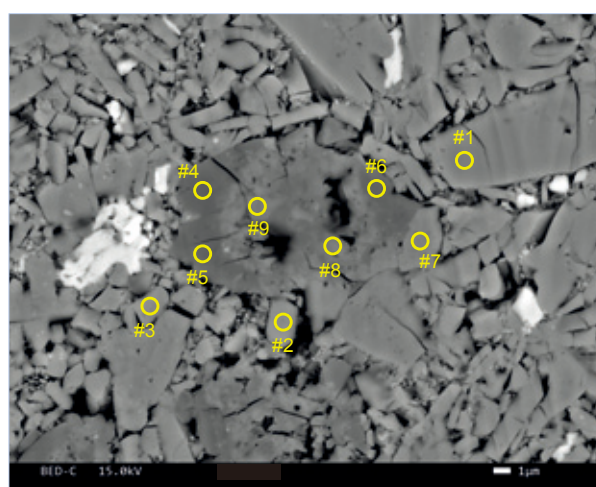


Image of the JXA-iHP200F with: an EDS, 5 WDS, and an SXES-ER.

## Results and Discussion

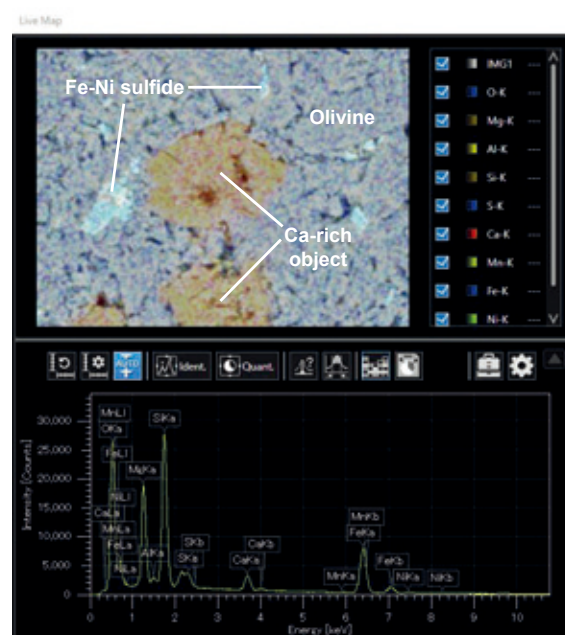
The most abundant mineral in matrix of the Allende meteorite is olivine (Ol), which appears in the form of barred shape of a few μm. It also contains pyroxene, Fe-Ni metal, Fe sulfide, a few graphite, nepheline and sodalite. A backscattered electron (BSE) image of the analyzed area on the Allende matrix is shown in Fig. 2. The bar/rectangular shaped olivine grains indicate a sharply defined grain boundary, and the formless aggregates which have a zoned compositional contrast appear to be surrounded by the olivine grains. The EDS LiveMap function of the JXA-iHP200F superimposes elemental maps collected with EDS in real time, while viewing the sample with the electron image. (Fig. 3). It is obvious from the real time image

Fig. 2



Backscattered electron image of Allende matrix minerals. Numbered markers indicate microanalysis points.

Fig. 3



Analysis example of the Allende matrix minerals using the EDS LiveMap function.

that the formless aggregates include a higher concentration of Si and Ca than the surrounding olivine grains. The formless aggregate was named a “Ca-rich object” by a previous study [5]. The mineralogy of these objects, that were observed inside and around the “dark inclusion”, rich in Ca, were considered to be generated as a result of secondary aqueous alteration on the chondrite parent body. The formation process of Ca-rich objects is speculated through the distribution of Ca, Na, Fe and S in the dark inclusions and in the neighboring Allende matrix.

### Quantitative Analysis using EPMA

**Table 1** shows the quantitative analysis of Allende matrix minerals conducted by EPMA and those results. The chemical compositions of matrix olivines are well consistent with previous studies [5, 7], which are Fe rich (compared to Mg) olivines. The dark and bright minerals in the BSE image of Ca-rich grains exhibit a number of Si cations of about 8 when the O number is 24. This infers that these minerals are pyroxene-type, and not garnet-type minerals (6 Si cations). Dark minerals have a lower Fe content than the bright minerals. In both, the Ca concentrations are approximately 21-22%, consistent with the Ca-rich pyroxene and hedenbergite reported for the Allende meteorite, but in contrast, the fact that Mg and Fe are major elements is not consistent. Inferring from the compositions of the major elements, the constituent minerals of this Ca-rich grains are considered to be solid solution series of diopside (Di:  $\text{CaMgSiO}_3$ ), hedenbergite (Hed:  $\text{CaFe}^{2+}\text{SiO}_3$ ) and augite (Aug:  $(\text{Ca, Mg, Fe})\text{Si}_3\text{O}_6$ ). In this paper, the dark minerals in the BSE image are called “dark Ca-rich pyroxene (D-Cpy)”, and bright minerals are called “light Ca-rich pyroxene (L-Cpy)”.

### Fitting method for the Fe L-emission spectra

Fitting calculations for the Fe L-emission spectra obtained with the SXES were conducted to provide a quantitative read out of peak position and intensity ratio. The calculation method in this study is as follows. As shown in **Fig. 4**, the Fe  $L\alpha$  line is the characteristic X-ray derived from electronic transition from the M4 and M5-shell to the L3-shell. In this study, we used a method of assigning two Pseudo-Voigt functions (addition of the Lorentzian function and the Gaussian function) to the  $L\alpha$  region and one Pseudo-Voigt functions to the  $L\beta$  region. The fitting formulas are described below:

$$I_o = f_A(E) + f_B(E) + f_C(E) + B(E) + \varepsilon(E)$$

$$R = \sum \varepsilon(E)$$

- $f_A(E)$ : Pseudo-Voigt function 1
- $f_B(E)$ : Pseudo-Voigt function 2
- $f_C(E)$ : Pseudo-Voigt function 3
- $B(E)$ : Background (Linear function)
- $\varepsilon(E)$ : Residual error
- $I_o$ : Measured signal intensity
- R: Total residuals

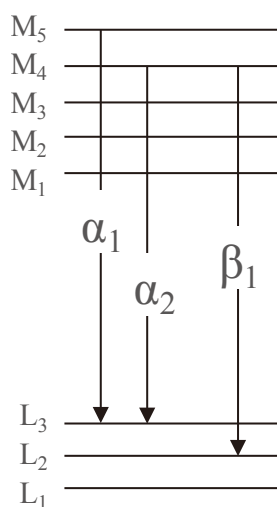
The background was approximated with a linear function, and the least squares method was repeatedly calculated as that the total residuals of the measured signal intensity value and the fitting values were minimized (**Fig. 5a**). Residual errors between the measured value and fitted line are plotted to evaluate the fitted result (**Fig. 5b**). By using this fitting method, the residuals of both the oxides and silicate minerals could be reduced to below the level of a statistical function error. For the peak positions of the  $L\alpha$  and  $L\beta$  lines, and their relative intensities, the maximum values at each peak position are calculated.

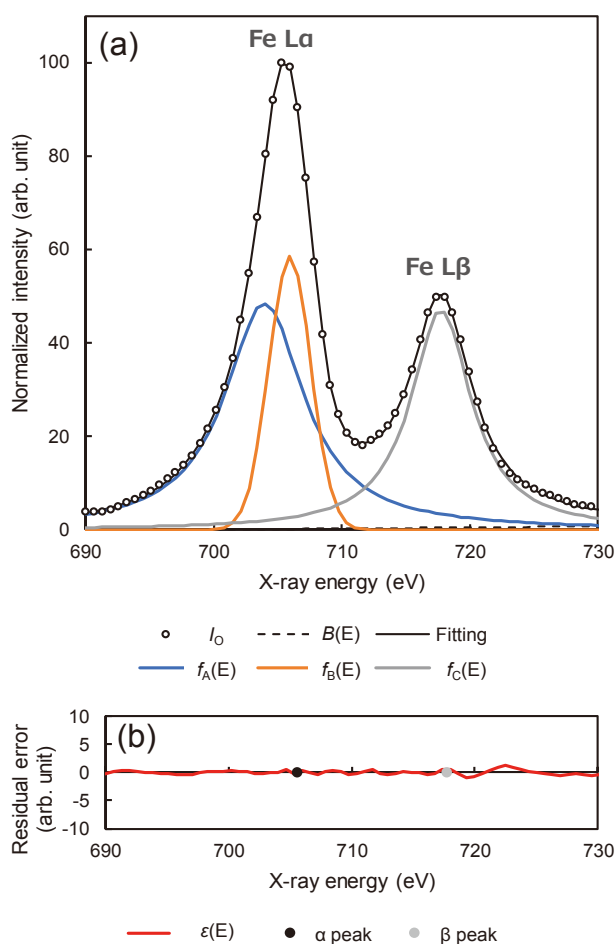
### Comparison of Fe L-emission spectra acquired with the SXES

**Figure 6** shows the Fe L-emission spectra of measured minerals using the SXES. Analytical conditions are: accelerating voltage 7 kV, beam current of 50 nA, with a fully focused beam for the matrix minerals of the Allende sample, and a 30  $\mu\text{m}$  defocused spot for the mineral standards. For each of the minerals in the Allende matrix, spectra with good reproducibility were obtained for each mineral. The positions of the peak energy of the matrix minerals and the  $L\alpha$  and  $L\beta$  ratios were compared with the spectra of the standard samples for each phase (**Table 2**). The spectra of olivine in the Allende matrix are similar to fayalite standard (Fa:  $\text{FeSiO}_4$ , \* an endmember of the olivine solid solution series). These exhibit lower peak energy positions and a higher  $L\beta/L\alpha$  ratio compared to pyroxene-type minerals. Conversely, results of the D-Cpy and L-Cpy show higher peak energy positions and significantly higher  $L\beta/L\alpha$  ratios compared to the matrix olivines. When comparing results of D-Cpy and L-Cpy, the spectral characteristics are clearly separated, and L-Cpys systematically shows higher peak energy positions and lower  $L\beta/L\alpha$  ratios.

**Table 1 Results of quantitative analysis of matrix minerals of the Allende meteorite by WDS analysis.**

Spot	Composition (mass%)											Cation	
	CaO	SO <sub>3</sub>	MnO	Al <sub>2</sub> O <sub>3</sub>	SiO <sub>2</sub>	FeO	NiO	TiO <sub>2</sub>	MgO	Total	Si	Total	
#1 OI_1	0.13	0.19	0.20	0.42	35.11	40.58	0.08	0.04	21.67	98.43	6.10	17.80	
#2 OI_2	0.25	2.53	0.18	0.18	34.62	39.53	1.13	0.00	21.51	99.93	5.86	17.48	
#3 OI_3	0.32	1.04	0.20	0.14	34.35	40.87	0.43	0.08	22.54	99.97	5.96	17.75	
#4 D-Cpy_1	22.32	0.42	0.04	1.03	53.89	7.32	0.16	0.07	13.54	98.78	8.03	15.78	
#5 D-Cpy_2	21.34	0.42	0.01	0.99	53.76	7.03	0.26	0.03	14.63	98.47	8.01	15.80	
#6 D-Cpy_3	21.08	0.30	0.07	2.11	51.80	9.21	0.13	0.06	13.37	98.14	7.78	15.89	
#7 L-Cpy_1	20.74	2.31	0.24	0.95	49.14	16.73	0.93	0.03	8.26	99.34	7.66	15.75	
#8 L-Cpy_2	21.67	0.27	0.42	0.39	50.52	21.06	0.16	0.00	4.85	99.34	8.04	15.86	
#9 L-Cpy_3	21.44	0.28	0.23	0.47	49.05	16.99	0.21	0.02	7.27	95.97	7.96	15.96	

**Fig. 4**

 Electron transition diagram of the  $L\alpha$  and  $L\beta$  emissions.

**Fig. 5**


Fitting example of a magnetite Fe  $L$ -emission spectrum.  
 (a) Observed values (white circles) and fitted line (black solid line).  
 (b) The residual error between the observed value and the fitted line.

Quantitative evaluation is not possible because there are no standard reference materials with known Fe valence information for pyroxene-type minerals. However, Höfer and Brey (2007) reported that the shift of peak energy to the high energy side and low  $L\beta/L\alpha$  ratios correlate with the composition of trivalent Fe [4]. These results indicate that the oxidation number of Fe in L-Cpy has a higher proportion of trivalent Fe than in D-Cpy.

## Conclusions

In this paper, mineral identification and the results of Fe  $L$ -emission spectra from a single mineral grain in the matrix of Allende meteorite using an FEG EPMA with an SXES is introduced. Analytical regions including olivine grains and Ca-rich grains, which are a secondary product in the Allende matrix were analyzed using the EDS LiveMap function of JXA-iHP200F. The result of quantitative analysis shows that the chemical compositions of matrix olivines are consistent with previous studies, and that the pyroxene-type minerals with light and dark contrast in the BSE image can be easily classified into two types. The Fe  $L$ -emission spectra of each mineral in the Allende matrix exhibits obvious characteristic differences. Among the two types of pyroxene-type minerals, the Ca-rich grain, (L-Cpy) was shown to have a higher proportion of trivalent Fe than D-Cpy.

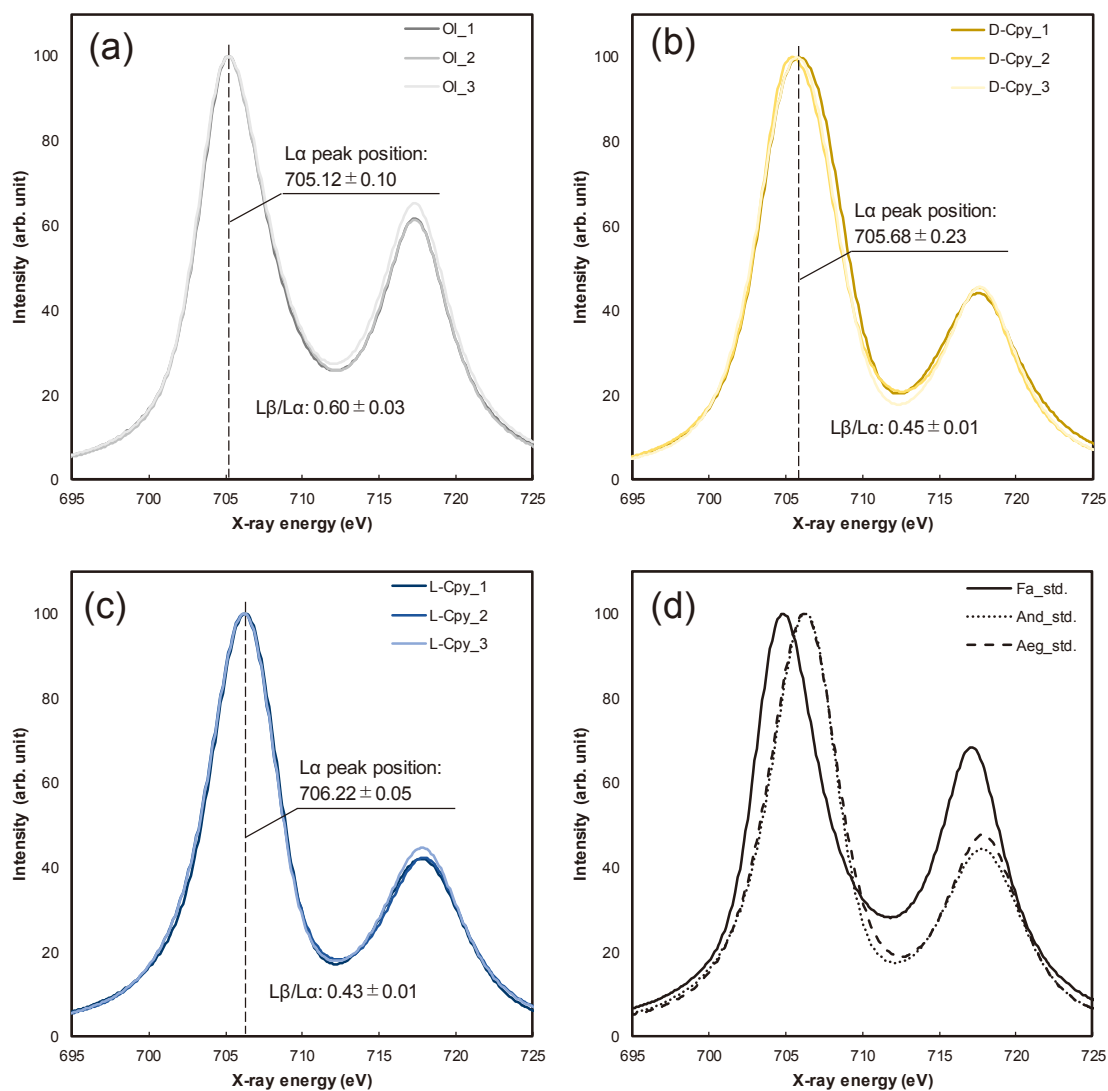
## Acknowledgments

I am very grateful to Dr. Yoshiaki Kon (National Institute of Advanced Industrial Science and Technology; Geological Survey of Japan) and Dr. Terumi Ejima (Department of Science, Shinshu University) for discussions and giving me advice for the calculation methods and interpretation of the results.

## References

- [ 1 ] H. Takahashi, T. Murano, M. Takakura, S. Asahina, M. Terauchi, M. Koike, T. Imazono, M. Koeda and T. Nagano, "Development of soft X-ray emission spectrometer for EPMA/SEM and its application", *IOP Conf. Ser.: Mater. Sci. Eng.* **109**, 012017 (2016) etc.
- [ 2 ] A. L. Albee and A. A. Chodos, "Semiquantitative electron microprobe determination of  $Fe^{2+}/Fe^{3+}$  and  $Mn^{2+}/Mn^{3+}$  in oxides and silicates and its application to petrologic problems", *The American Mineralogist*, **55**, 491-501 (1970).
- [ 3 ] H. E. Höfer, G. P. Brey, B. Schulz-Dobrick and R. Oberhänsli, "The determination of the oxidation state of iron by the electron microprobe", *Eur. J. Mineral.* **6**, 407-418 (1994).
- [ 4 ] H. E. Höfer, G. P. Brey, "The iron oxidation state of garnet by electron microprobe: Its determination with the  $\beta$  flank method combined with major-element analysis", *American Mineralogist*, **92**, 873-885 (2007).
- [ 5 ] A. N. Krot, M. I. Petaev, A. Meibom and K. Keil, "In situ growth of Ca-rich rims around Allende dark inclusions", *Geochemistry International*, **38**, 351-368 (2000).
- [ 6 ] P. Cuivillier, H. Leroux, D. Jacob and P. Hirel, "Fe-Mg interdiffusion profiles in rimmed forsterite grains in the Allende matrix: Time-temperature constraints for the parent body metamorphism", *Meteoritics & Planetary Science*, **50(9)**, 1529-1545 (2015).
- [ 7 ] M. Kimura and Y. Ikeda, "Anhydrous alteration of Allende chondrules in the solar nebula II: Alkali-Ca exchange reactions and formation of nepheline, sodalite and Ca-rich phases in chondrules", *Proc. NIRP Symp. Antarct. Meteorites*, **8**, 123-138 (1995).

**Fig. 6**



Fe L-emission spectra of minerals in the Allende matrix and Fe mineral standards.

(a) olivine, (b) dark Ca-rich pyroxene, (c) light Ca-rich pyroxene, (d) Fe mineral standards (Fa: fayalite, And: Andradite, Aeg: Aegirine).

**Table 2 Results of Fe L-emission spectral analysis of Allende matrix minerals and Fe mineral standards.**

Olivine	Ol_1	Ol_2	Ol_3	Total	$\sigma$
L $\alpha$ peak (eV)	705.20	705.15	705.01	<b>705.12</b>	<b>0.10</b>
L $\beta$ peak (eV)	717.32	717.30	717.24	<b>717.29</b>	<b>0.04</b>
L $\beta$ /L $\alpha$	0.62	0.61	0.57	<b>0.60</b>	<b>0.03</b>
Dark-Cpy	D-Cpy_1	D-Cpy_2	D-Cpy_3	Total	$\sigma$
L $\alpha$ peak (eV)	705.87	705.43	705.75	<b>705.68</b>	<b>0.23</b>
L $\beta$ peak (eV)	717.55	717.63	717.68	<b>717.62</b>	<b>0.06</b>
L $\beta$ /L $\alpha$	0.44	0.46	0.46	<b>0.45</b>	<b>0.01</b>
Light-Cpy	L-Cpy_1	L-Cpy_2	L-Cpy_3	Total	$\sigma$
L $\alpha$ peak (eV)	706.27	706.18	706.21	<b>706.22</b>	<b>0.05</b>
L $\beta$ peak (eV)	717.75	717.90	717.79	<b>717.81</b>	<b>0.08</b>
L $\beta$ /L $\alpha$	0.42	0.42	0.45	<b>0.43</b>	<b>0.01</b>
Standards	Fa	Aeg	And		
L $\alpha$ peak (eV)	<b>704.78</b>	<b>706.16</b>	<b>706.27</b>		
L $\beta$ peak (eV)	<b>717.09</b>	<b>717.74</b>	<b>717.75</b>		
L $\beta$ /L $\alpha$	<b>0.68</b>	<b>0.49</b>	<b>0.44</b>		

# MultiAnalyzer – Unknown Compounds Analysis System

## New Gas Chromatograph Time-of-Flight Mass Spectrometer

### JMS-T2000GC “AccuTOF™ GC-Alpha”

Masaaki Ubukata MS Business Unit, JEOL Ltd.

The JMS-T2000GC AccuTOF™ GC-Alpha is the 6th generation JEOL GC-TOFMS and has an improved ion optics system to achieve ultra-high resolution. The AccuTOF™ GC-Alpha is an orthogonal-acceleration time-of-flight mass spectrometer (oaTOFMS) with dual stage reflectron. It employs an ideal ion optical system realizing both high ion transmission (=sensitivity) and ultra-high resolution. The dedicated qualitative software msFineAnalysis makes full use of the high-quality data obtained by the JMS-T2000GC AccuTOF™ GC-Alpha, thus providing a new approach to qualitative analysis for identification of unknown compounds. JEOL can offer real unknown compounds analysis solution with the powerful combination with JMS-T2000GC AccuTOF™ GC-Alpha and msFineAnalysis.

## Introduction

Modern mass spectrometers (MS) are used for a variety of applications and scientific fields. Among these MS systems, the gas chromatograph-mass spectrometer (GC-MS) is suitable for both qualitative and quantitative analyses of volatile compounds and plays a crucial role in the analysis of materials, forensics, foods, environmental contaminants, etc. For qualitative analysis, GC-MS analysis typically involves collecting electron ionization (EI) mass spectra and then using these spectra for library database searches to identify each analyte. While this technique is effective for compounds found within these libraries, there are still many compounds that are not registered in the databases. As a result, additional tools are necessary to perform non-targeted analysis of unregistered components that can often appear during the analysis of materials and environmental samples. To address this situation, JEOL has continuously enhanced and improved upon our GC-MS products to include a variety of advanced capabilities, as shown in **Fig. 1**. The features improved upon include:

- 1) A Time-of-Flight Mass Spectrometer (TOFMS) that can acquire mass spectra with high resolution (HR) and high mass accuracy
- 2) Soft ionization techniques that are essential for determining the molecular weight and molecular formula of unknown substances
- 3) User-friendly software that automatically performs accurate mass analysis for the measured data

Our 6<sup>th</sup> generation GC-TOFMS, the JMS-T2000GC “AccuTOF™ GC-Alpha,” was introduced into the market this year with significantly enhanced capabilities for higher mass resolution and higher mass accuracy. In this report,

we will provide an overview of the AccuTOF™ GC-Alpha instrumentation as well as its basic performance capabilities.

## Overview of the Instrument

The new AccuTOF™ GC-Alpha system is shown in **Fig. 2** and represents a significant design change from the previous models shown in **Fig. 1**. Specifically, the orthogonal acceleration (oa)-TOFMS ion trajectory was changed from the conventional “V”-like trajectory to a new “A”-like trajectory in order to extend the ion flight distance from 2 m to 4 m as shown in **Fig. 3**. Additionally, the oa-TOFMS was equipped with an improved ion acceleration system that spatially focuses the ion beam and an improved reflectron system that temporally focuses the ion beam. Because the system is a HRTOF-MS, the instrument is always operating in high resolution mode. Furthermore, by optimizing these components (along with the longer flight path), the AccuTOF™ GC-Alpha represents a significant improvement in both mass resolving power and mass accuracy. The AccuTOF™ GC-Alpha provides 6 times higher resolution than our 1<sup>st</sup> generation “AccuTOF™ GC”.

## Basic High-Performance System for Non-Targeted Analysis

The basic performance of the AccuTOF™ GC-Alpha are as follows:

- Sensitivity: OFN 1 pg, S/N > 300
- Mass Resolving Power: > 30,000 (FWHM,  $m/z$  614)
- Mass Accuracy: < 1 ppm (RMS, EI standard ion source)
- Mass Range:  $m/z$  4 – 6,000
- Spectrum Recording Speed: Up to 50 spectra/sec
- Ionization Methods: EI, CI, PI, FI, DEI, DCI, and FD

**Fig. 1 History of JEOL GC-HR-TOFMS**



**Fig. 2 JMS-T2000GC "AccuTOF™ GC-Alpha"**



**Fig. 3 Schematics of ion optical system**



### High Sensitivity

The new AccuTOF™ GC-Alpha has maintained the same sensitivity specifications as the previous generation system, despite the longer flight path and completely redesigned hardware. **Fig. 4a** shows the  $m/z$  271.9867 extracted ion chromatogram (EIC) for 1 pg of octafluoronaphtalene (OFN) in which the GC-Alpha was able to easily achieve a  $S/N > 300$ . **Fig. 4b** shows the OFN EICs for the instrument detection limit (IDL) measurements in which 100 fg of OFN was injected 8-times. Additionally, **Fig. 4b** includes a table of peak areas, the calculated relative standard deviation (RSD) for these peak areas of 6.2%, and the calculated IDL of 18.7 fg. These results clearly demonstrate that the AccuTOF™ GC-Alpha provides both high sensitivity and high stability even for trace components analysis.

### High Mass-Resolving Power

The AccuTOF™ GC-Alpha has a much higher mass-resolving power than the previous generations of the instrument. To demonstrate this new resolution capability, **Fig. 5a** shows the EI mass spectrum for PFTBA in which the  $m/z$  614 peak was enlarged to clearly display the FWHM resolution of  $>30,000$ , which is the new resolution specification. To further highlight how this improved resolving power can enhance sample analysis, **Fig. 5b** shows the baseline separation of  $CO^+$  ( $m/z$  27.9949) and  $N_2^+$  ( $m/z$  28.0061) which was not possible with the previous generation instruments. These results clearly demonstrate that the high mass-resolution of the AccuTOF™ GC-Alpha can easily separate closely related ions (same nominal mass) and thus can be a powerful tool for a wide range of analyses and applications involving analytes with the same nominal mass but different elemental compositions.

**Fig. 4 OFN 1 pg sensitivity and IDL for OFN 100 fg measurement**

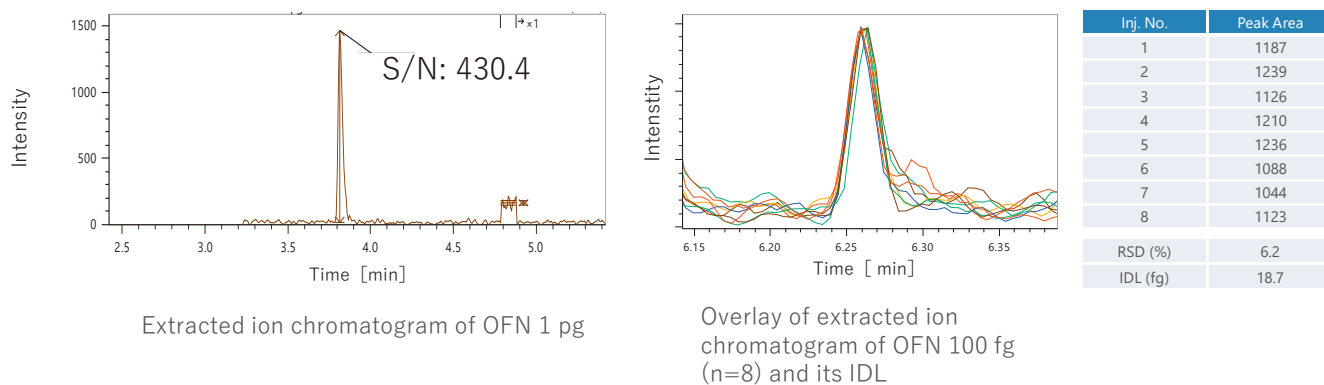
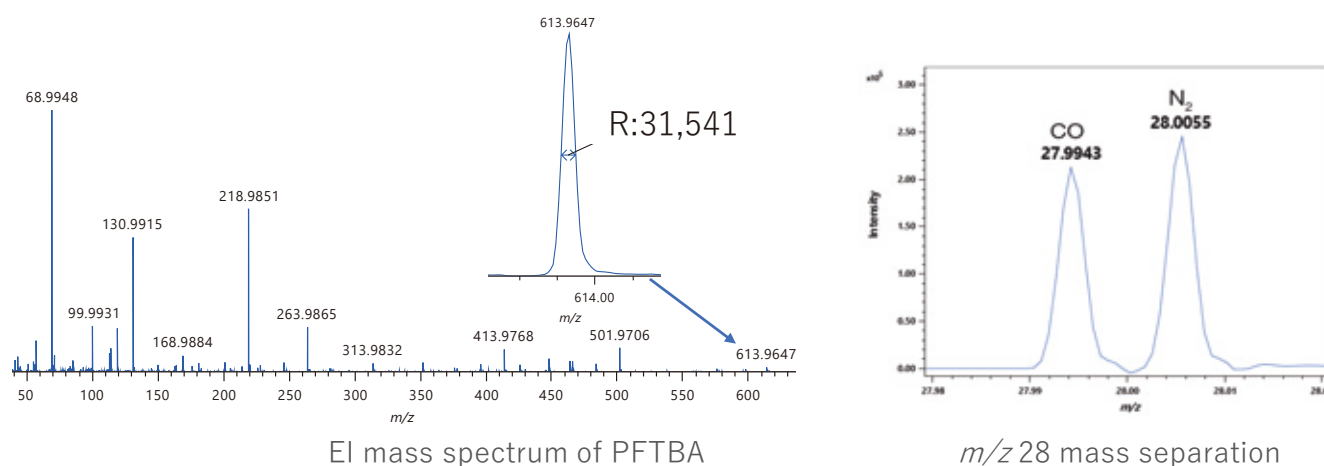


**Fig. 5 EI mass spectrum of PFTBA and  $m/z$  28 mass separation**



## High Mass-Accuracy

Along with higher mass resolving power, the AccuTOF™ GC-Alpha also has higher mass accuracy with a new specification of less than 1 ppm. An EI mass spectrum of methyl stearate along with the accurate mass analysis results for all observed ions are shown in Fig. 6. These results demonstrate that high mass accuracy is maintained over the entire mass range (from  $m/z$  43 corresponding to the lowest mass fragment ion up to  $m/z$  298 corresponding to the molecular ion), thus simplifying the determination of each compositional formula. Furthermore, the average mass error for these 10 ions was only 0.05 mDa / 0.45 ppm.

Also, worth noting here, the AccuTOF™ GC-Alpha produces high mass-accuracy mass spectra independent of the ionization method used for the measurements. This is important because the new system also offers all of the same ionization options that were available with the previous models - electron ionization (EI), chemical ionization (CI), photo ionization (PI), field ionization (FI) for GC-MS and desorption electron ionization (DEI), desorption chemical ionization (DCI), and field desorption (FD) methods for direct probe sample introduction. Therefore, the high mass accuracy of the AccuTOF™ GC-Alpha can be used with hard ionization (EI) for library searches / fragment ion formula determination and with soft ionization (CI, PI, FI) for molecular formula determination for the observed molecular ion / molecular ion adduct. This combination of mass accuracy and hard / soft ionization is a powerful tool for qualitative analysis of unknown compounds.

### Powerful Capabilities for GC-MS Qualitative Analysis

- The AccuTOF™ GC-Alpha simultaneously achieves high sensitivity, high mass resolution and high mass accuracy.
- The AccuTOF™ GC-Alpha is suitable for not only target analysis but also non-targeted analysis of samples, even at trace levels.

### Wide Mass Range

The AccuTOF™ GC-Alpha maintains the wide mass range ( $m/z$  4-6000) of the previous generation systems. While GC-

MS analysis is typically limited to analytes under  $m/z$  1000, this increased mass range unlocks the analyst's ability to directly analyze samples like polymers and organometallics by using direct probe MS in which the sample is directly introduced into the ion source (not through the GC). The AccuTOF™ GC-Alpha accommodates two direct sample introduction probes (Direct Exposure Probe and Direct Insertion Probe) for direct EI measurement and direct CI measurement. Additionally, the optional FD probe allows the analyst to use a soft ionization direct probe method that is easy to use for the analysis of materials like polymers and higher molecular weight petrochemicals. Most commercial GC-MS instruments are dedicated only to GC-MS measurement, but the AccuTOF™ GC-Alpha can also be used as a direct MS instrument.

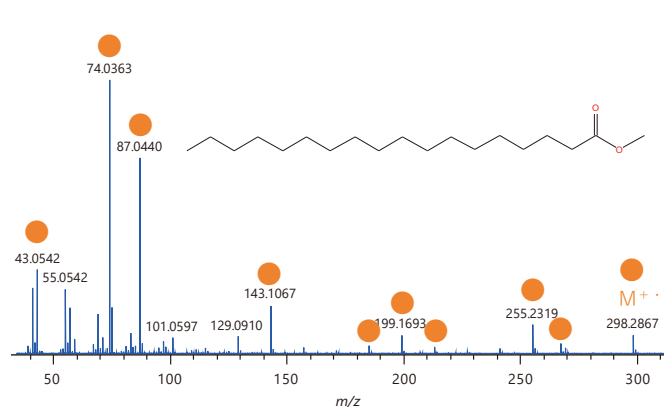
### High-Speed Data Acquisition

The AccuTOF™ GC-Alpha maintains the high-speed data acquisition rate (up to 50 spectra/sec) of the previous generation systems as well. This capability is critical for doing Fast GC and GCxGC measurements which both require fast spectrum recording intervals. In particular, the AccuTOF™ GC-Alpha allows the user to bring together GCxGC separation, high resolution MS, high mass accuracy, EI, and soft ionization (CI, PI, FI) to analyze samples that are typically too complex for standard GC-MS separations.

### Combined EI Method and Soft Ionization Methods – two combination ion sources –

As mentioned previously, library database searches are typically used for GC-MS qualitative analysis. However, for unknown compounds that are not registered in the MS databases, it can be difficult to identify these unknowns by using EI data alone. EI is a hard ionization method that typically produces many fragment ions as well as molecular ions. With that said, it is not uncommon for EI to produce minimal or no molecular ion signal in the mass spectrum. Consequently, the analyst can have difficulty deciding if

Fig. 6 EI mass spectrum of methyl stearate and the mass accuracy



EI mass spectrum of methyl stearate

Obs. $m/z$	Formula	Calc. $m/z$	Error	
			[mDa]	[ppm]
43.0542	C3 H7	43.0542	-0.06	-1.42
74.0363	C3 H6 O2	74.0362	0.10	1.40
87.0440	C4 H7 O2	87.0441	-0.01	-0.16
143.1067	C8 H15 O2	143.1067	0.03	0.22
185.1537	C11 H21 O2	185.1536	0.05	0.26
199.1693	C12 H23 O2	199.1693	0.04	0.19
213.1850	C13 H25 O2	213.1849	0.08	0.39
255.2319	C16 H31 O2	255.2319	0.03	0.11
267.2683	C18 H35 O	267.2682	0.05	0.18
298.2867	C19 H38 O2	298.2866	0.06	0.20
Averaged mass error (Abs.)			0.05	0.45

there is a molecular ion present in the EI spectrum, thus complicating the data analysis. To overcome this problem, it can be very effective to use soft ionization methods to confirm the molecular ion / molecular adduct ion. The AccuTOF™ GC-Alpha has two optionally available combination ion sources that can be used to switch between EI and a soft ionization method (**Fig. 7**).

The EI/FI/FD combination ion source offers the combination of EI (hard ionization) and FI (soft ionization) for GC-MS measurements and FD (soft ionization) for direct probe MS measurements of heavier materials that do not go through the GC. Basically, this combination ion source allows the analyst to do GC/EI, GC/FI and FD measurements without breaking vacuum. All that is required to switch between ionization modes is the exchanging of the EI repeller probe with the FI/FD probe through a vacuum interlock that goes directly into the ion source. FI is the softest ionization method available (\*Note) and will even produce molecular ions for saturated hydrocarbons.

The EI/PI combination ion source allows the AccuTOF™ GC-Alpha to be switched from GC/EI (hard ionization) to GC/PI (soft ionization) measurements without breaking vacuum. In this case, the ion source only requires switching between ON/OFF for the EI filament and ON/OFF for the PI ultraviolet-light lamp when switching between each ionization method. PI is particularly effective and sensitive for producing molecular ions for substances that can absorb ultraviolet light (e. g. aromatic compounds).

These unique combination ion sources are options only available with the AccuTOF™ GC-Alpha (see Fig. 1). They are extraordinarily powerful in that these sources allow the user to switch between GC/EI and GC/soft ionization without breaking vacuum while also capitalizing on the high mass resolution and high mass accuracy provided by the TOFMS. Thus, the AccuTOF™ GC-Alpha used with these combination ion sources simplifies the process of doing non-targeted,

qualitative analysis of unknown compounds.

\*Note: This case is applicable for ionization methods available with the AccuTOF™ GC-Alpha.

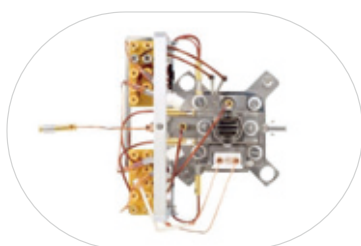
## Automatic Qualitative Analysis Software “msFineAnalysis”

Originally released in 2018 as an option for the previous generation JMS-T200GC Series, the latest version of the “msFineAnalysis” software is now included with the basic AccuTOF™ GC-Alpha system. This software was designed to automatically identify compounds in a sample measured by GC-MS. More specifically, msFineAnalysis uses a new workflow that integrates GC/EI (hard ionization) high resolution data with GC/soft ionization (FI, PI, CI) high resolution data to automatically generate a color-coded qualitative analysis report for a measured sample. **Fig. 8** shows the integrated workflow used by the software in which five different analysis steps are automatically combined to produce fast, high-accuracy qualitative analysis results. The msFineAnalysis software is already widely acknowledged as a powerful tool for non-targeted analysis.

The latest version of msFineAnalysis (Version 3) streamlines the software operation and adds a new function in which two similar samples can be directly compared in order to identify sample differences. This feature can be particularly useful for comparing complex materials that have subtle differences. Identifying these differences can be critically important for addressing changes in material synthesis or manufacturing processes in which product quality is critically important.

As a starting point, the difference analysis function uses multiple GC/EI data to determine the components observed within the two samples (here referred to as A and B). Then, a t-test statistical analysis is done to extract the components that are different. Afterwards, a full integrated analysis (Fig. 8) is performed using the GC/EI data and GC/SI data. If a characteristic component in A or B is not registered in the library database, the

**Fig. 7 Two combination ion sources**



### EI/FI/FD combination ion source

- EI and FI are switchable **without breaking a vacuum**.
- Replacement of the EI repeller probe and the FI emitter probe is needed.
- **FD (direct MS) measurement** is also possible.



### EI/PI combination ion source

- EI and PI are switchable **without breaking a vacuum**.
- Replacement of the hardware is not required.
- PI ionization energy is about 10.3 eV.

integrated analysis will still determine an elemental composition for the unknown component. **Fig. 9** shows the difference analysis window which includes a volcano plot, classification section (A only, B only, A>B, A<B and A=B), intensity ratio (Log2(B/A), p value, etc. For each class, the components and analysis results are color coded to distinguish them from each other in order to enable a quick visual understanding of the different components.

As an example of difference analysis using msFineAnalysis Version 3, the evolved gas analysis results of two epoxy types of adhesives are shown in **Fig. 10**. A headspace GC-MS method was used for this analysis. The difference analysis parameters were as follows: Acquisition numbers were 5 for each GC/EI measurements, the significance level was 5%, and the threshold for intensity difference was set to 2. The upper section of Fig. 10 shows the TIC chromatograms (solid lines) as well as the detected peaks from chromatographic deconvolution. Each peak is color coded with blue indicating a characteristic component for adhesive A, red indicating a characteristic component for adhesive B, and yellow indicating a component that is observed in both A and B (no difference). The blue and red color scheme is also applied to the integrated analysis report in the lower section of the window, but white is used in this case to identify the components observed in both A and B (no difference). The difference analysis results for this example showed:

- Toluene was observed in both adhesives.
- Adhesive A had a high intensity peak for butanol that was not observed from adhesive B.

- Adhesive B had several aromatic compounds such as ethylbenzene and xylene.
- Adhesive B had cyclic siloxanes.

For conventional GC-MS difference analysis, if the extracted characteristic component is not registered in the library database, then it can be difficult to identify this unknown component. However, using msFineAnalysis Version 3 makes it possible to automatically identify these components using the integrated analysis workflow that is subsequently performed after the difference analysis. This innovative 2-sample comparison solutions can be broadly applied to not only the materials field but also to a variety of other research and application fields.

## Conclusions

The new JMS-T2000GC “AccuTOF™ GC-Alpha” is a new high-resolution GC-TOFMS that represents a significant improvement over the previous generation instruments. The hardware was completely redesigned for improved resolving power, mass accuracy, sensitivity and stability. Along with the improved hardware of the AccuTOF™ GC-Alpha, the automatic qualitative analysis software “msFineAnalysis” was also upgraded to incorporate difference analysis between two-samples while also continuing to capitalize on the integrated analysis workflow that this software is known for. The combination of AccuTOF™ GC-Alpha and msFineAnalysis is a truly powerful solution for GC-MS qualitative analysis.

**Fig. 8 msFineAnalysis: Integrated analysis workflow**

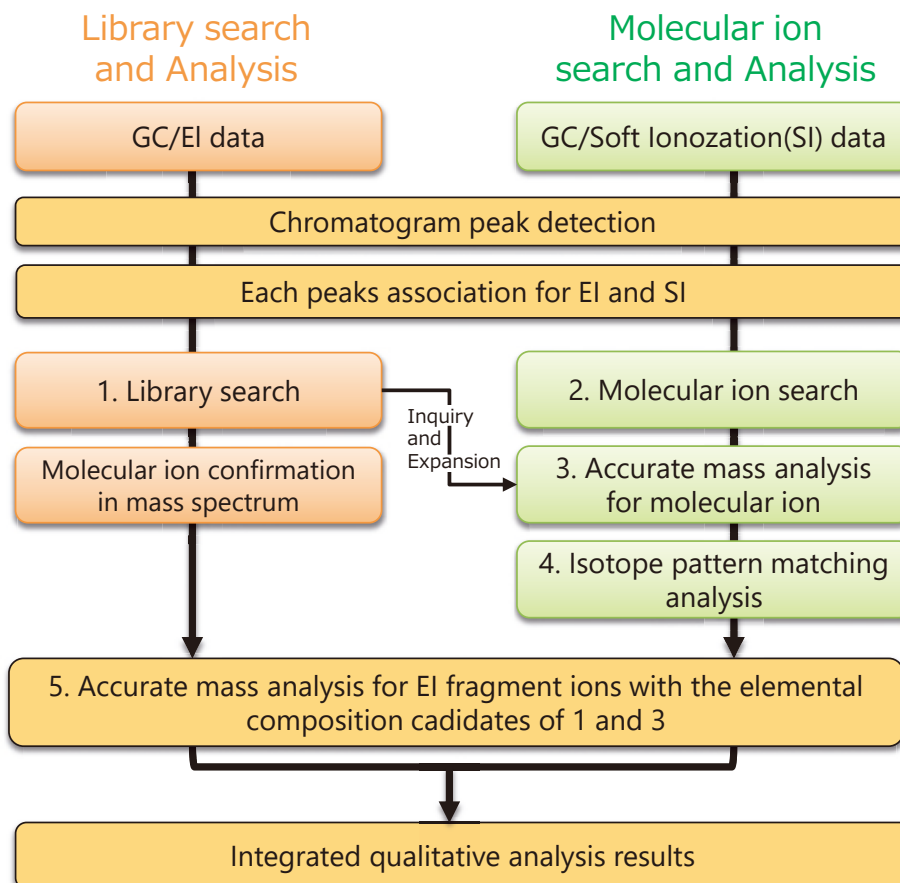


**Fig. 9 msFineAnalysis Ver.3: 2-samples comparison GUI**



**Volcano plot**

- Difference of 2 samples and reproducibility
- Easy to view characteristic components

**Classification**

- Distribution of each class
- A or B only, A>B, A<B, A=B



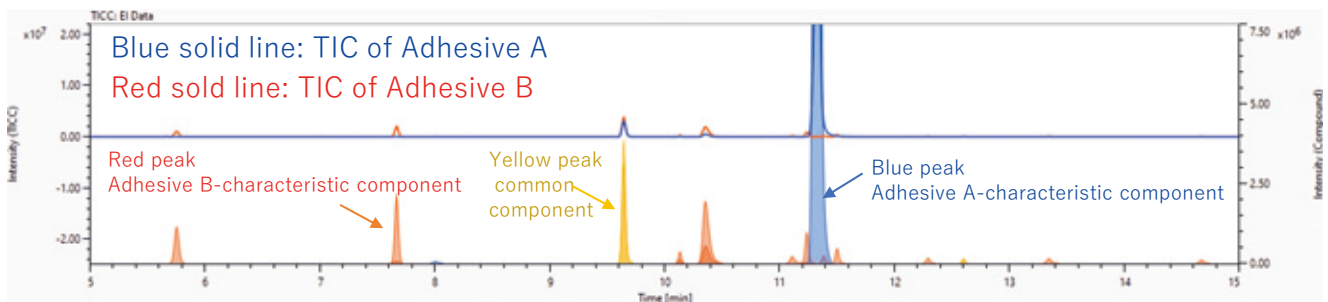
Possible to rapidly find characteristic or common components to each component

EI/SI integrated analysis result

Difference analysis result

- For all the data ad detected components, identification judgement is conducted, and then, difference analysis that takes account of statistical reproducibility is performed.
- Difference analysis result: Classification, Intensity ratio (Log2(B/A)), p value, Number of emergence, Volcano plot
- After difference analysis, the EI/SI integrated analysis of all the components is conducted.

**Fig. 10 Evolved-gas difference analysis of material components using HS-GC-TOFMS**



**Difference analysis + Integrated analysis result**

クロマトグラム/IM情報				差異分析結果				総合解析結果										
ID	RT [min]	幅 [s]	高さ [m/z]	リンク	IM m/z	種別	Log2(B/A)	-Log10(p-value)	出現数 (A)	出現数 (B)	化合物名	類似度	組成式	付加/脱離	m/z (計算)	質量誤差 [mDa]	同位体 マッチング	フラグメント カバ-率
001	5.75	8.00	1139828	2.54	222.05689	B Only	4.00	4.68	0	5	Cyclotrisiloxane, hexamethyl-	957	C6 H18 O3 Si3	無し	222.05583	1.06	N/A	100
002	7.66	6.00	2129025	4.73	281.05042	A + B	4.00	4.42	5	5	Cyclotrisiloxane, octamethyl-	902	C7 H21 O4 Si4	-CH3	281.05114	-0.72	0.89	100
003	8.00	6.80	597118	0.13	130.13524	A Only	-4.00	5.00	5	0	n-Butyl ether	867	C8 H18 O	無し	130.13522	0.03	N/A	100
004	9.64	7.60	3812139	8.50	92.06221	A + B	0.12	1.28	5	5	Toluene	960	C7 H8	無し	92.06205	0.15	0.97	100
005	10.12	4.80	361148	0.81	355.06898	A + B	1.76	5.00	5	5	Cyclopentasiloxane, decamethyl-	933	C9 H27 O5 Si5	-CH3	355.06993	-0.95	0.66	100
006	10.36	12.80	1936628	4.32	74.07312	A + B	1.70	4.83	5	5	1-Propanol, 2-methyl-	819	C4 H10 O	無し	74.07262	0.51	0.69	100
007	11.11	11.60	208814	0.47	90.06757	B Only	4.00	5.00	0	5	2-Propanol, 1-methoxy-	824	C4 H10 O2	無し	90.06753	0.03	0.39	100
008	11.24	6.80	960683	2.14	106.07748	B Only	4.00	5.00	0	5	Ethylbenzene	963	C8 H10	無し	106.07770	-0.22	0.79	100
009	11.33	12.40	44842834	100.00	74.07291	A Only	-4.00	5.00	5	0	1-Butanol	801	C4 H10 O	無し	74.07262	0.29	N/A	100
010	11.38	5.60	233859	0.52	106.07764	B Only	4.00	5.00	0	5	p-Xylene	952	C8 H10	無し	106.07770	-0.07	N/A	100
011	11.50	6.80	461857	1.03	106.07784	B Only	4.00	5.00	0	5	Benzene, 1,3-dimethyl-	967	C8 H10	無し	106.07770	0.13	0.95	100
012	12.29	6.80	159354	0.36	106.07822	B Only	4.00	5.00	0	5	p-Xylene	954	C8 H10	無し	106.07770	0.51	0.93	100
013	12.60	4.80	153832	0.34	429.08815	A + B	0.34	3.19	5	5	Cyclohexasiloxane, dodecamethyl-	932	C11 H33 O6 Si6	-CH3	429.08872	-0.57	0.65	100
014	13.34	8.40	148724	0.33	119.10627	B Only	4.00	5.00	0	5	Ethanol, 2-(1,1-dimethylethoxy)-	872	C6 H15 O2	+H	119.10666	-0.39	N/A	100
015	14.67	7.20	103236	0.23	73.05243	B Only	4.00	5.00	0	5	Formamide, N,N-dimethyl-	863	C3 H7 N O	無し	73.05222	0.21	0.69	100

Blue line: Adhesive A-characteristic component

Red line: Adhesive B-characteristic component

White line: Common component

# Introduction of JEOL Products

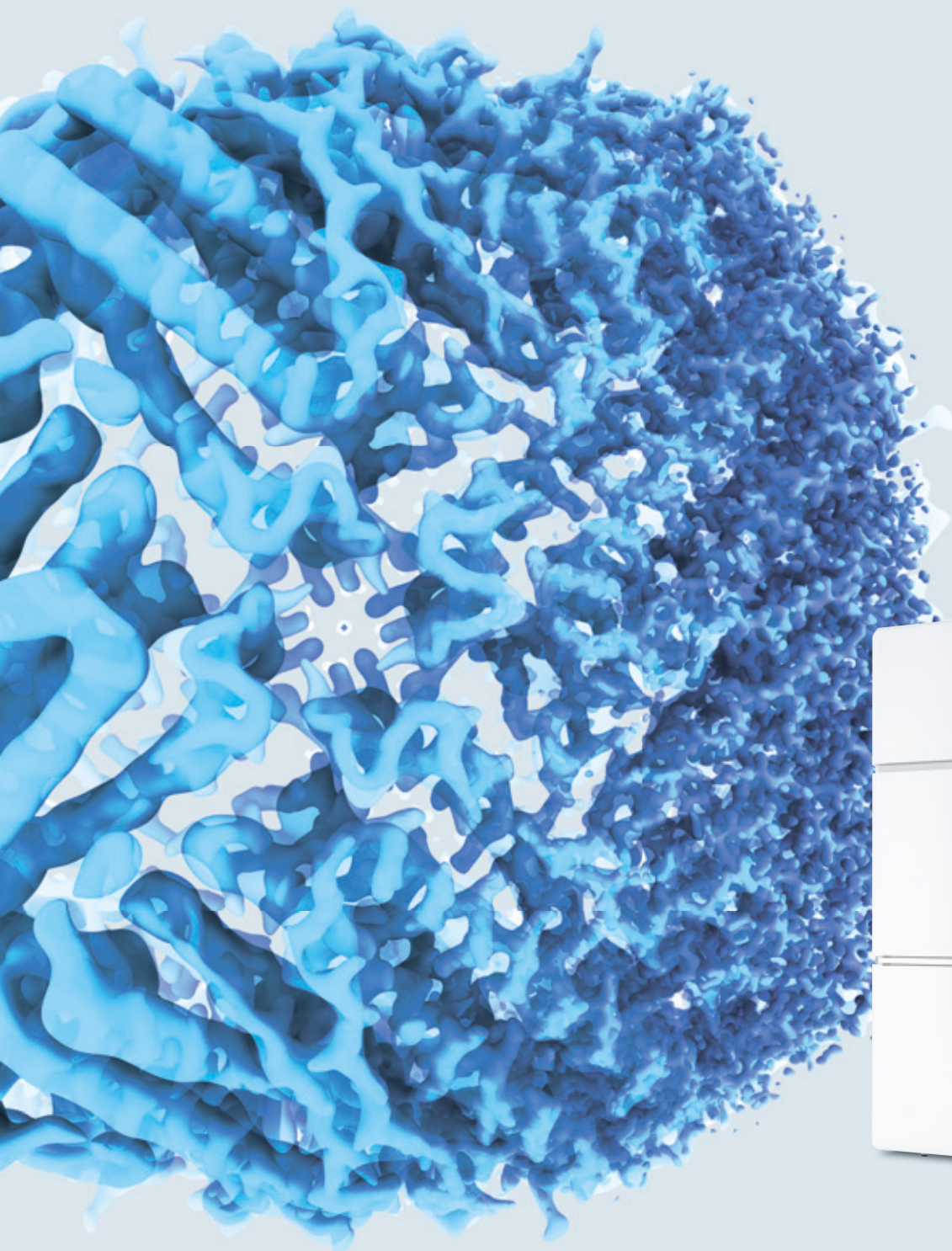
Field Emission Cryo-Electron Microscope

JEM-3300

## **CRYO ARM™ 300 II**

The next stage of CRYO ARM™ 300

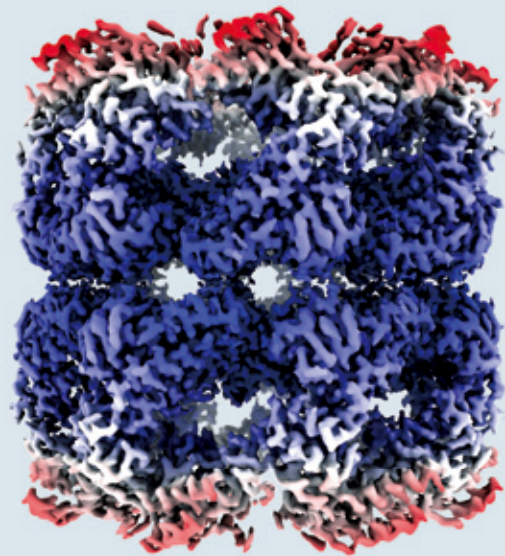
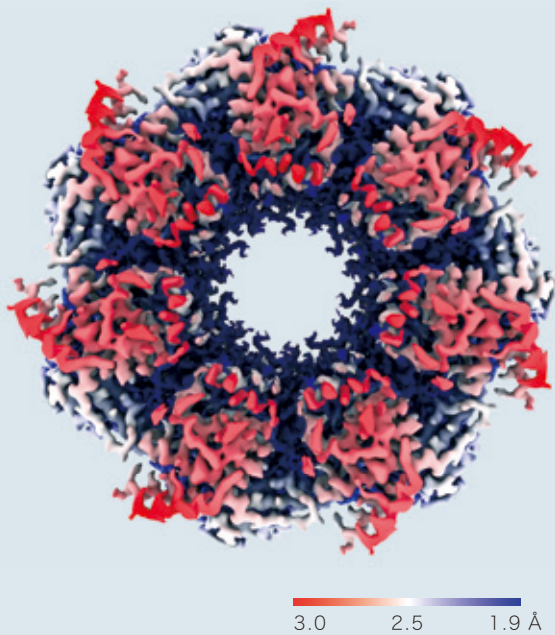
- High-throughput, High-resolution and High-stability -



## Applications

### GroEL

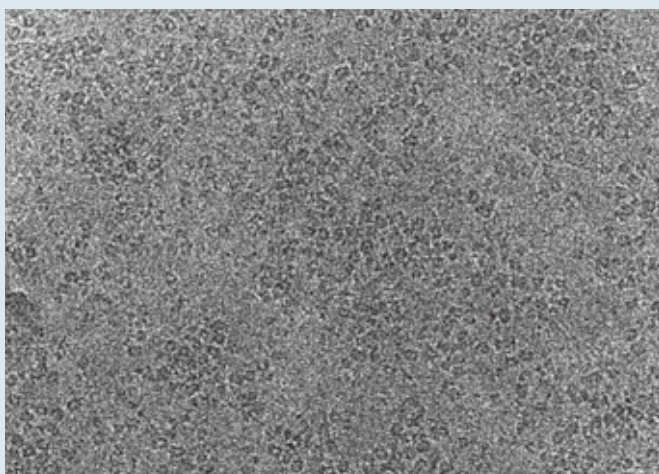
GroEL structure at 1.98 Å resolution achieved by only 504 micrographs, a dramatic improvement from 3.1 Å resolution from 1,883 micrographs in a previous study. (as of Oct. 26, 2020 at EMDB)



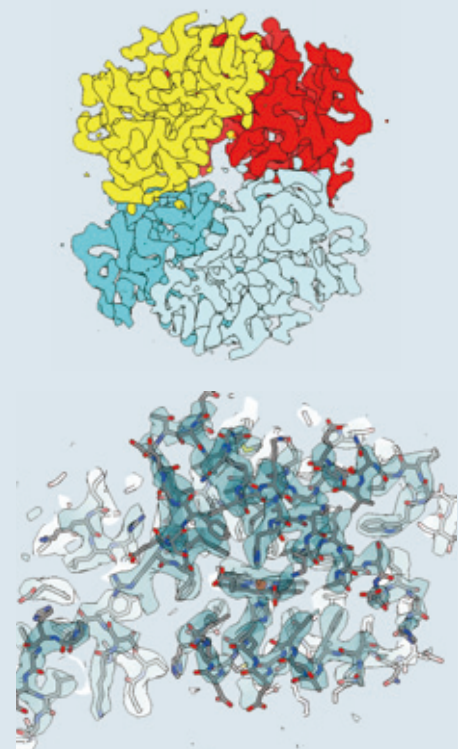
Data courtesy of **Dr. Junso Fujita** at Osaka University

### Hemoglobin

Cryo-electron micrograph (left), 3D density map (upper right) and fitted atomic model (lower right) of human hemoglobin obtained by high speed data collection, 850 movies per hour.



Specimen courtesy of **Dr. Miki Kinoshita** at Osaka University



Certain products in this brochure are controlled under the "Foreign Exchange and Foreign Trade Law" of Japan in compliance with international security export control, JEOL Ltd. must provide the Japanese Government with "End-user's Statement of Assurance" and "End-use Certificate" in order to obtain the export license needed for export from Japan. If the product to be exported is in this category, the end user will be asked to fill in these certificate forms.

**ARGENTINA**  
COASIN S.A.C.I.F.  
Virrey del Pino 4071,  
C14300AH-Buenos Aires  
Argentina  
Tel. 54-11-4552-3185  
Fax. 54-11-4555-3321

**AUSTRALIA & NEW ZEALAND**  
JEOL (AUSTRALASIA) Pty.Ltd.  
Suite 1, L2 18 Aquatic Drive  
- Frenchs Forest NSW 2086  
Australia  
Tel. 61-2-9451-3855  
Fax. 61-2-9451-3822

**AUSTRIA**  
JEOL (GERMANY) GmbH  
Gute Aenger 30  
83306 Freising, Germany  
Tel. 49-8161-9845-0  
Fax. 49-8161-9845-100

**BANGLADESH**  
A.O. CHOWDHURY SCIENCE & SYNERGY PVT. LTD.  
87, Suhrawardy Avenue, Floor 2  
Bardhara, Dhaka1212  
Bangladesh  
Tel. 88-02-222262272  
Fax. 88-02-222264228

**BELGIUM**  
JEOL (EUROPE) B.V.  
Planet II, Gebouw B  
Leuvensesteenweg 542,  
B-1930 Zaventem  
Belgium  
Tel. 32-2-720-0560  
Fax. 32-2-720-6134

**BRAZIL**  
JEOL Brasil Instrumentos Cientificos Ltda.  
Av. Jabaquara, 2958 5º andar conjunto 52  
04046-500 Sao Paulo, SP  
Brazil  
Tel. 55-11-5070 4000  
Fax. 55-11-5070 4010

**CANADA**  
JEOL CANADA, INC.  
3275 Tere Rue, Local #8  
St-Hubert, QC J3Y4Y6, Canada  
Tel. 1-450-676-8776  
Fax. 1-450-676-8694

**CHINA**  
JEOL (BEIJING) CO., LTD.  
Zhongkeziyuan Building South Tower 2F  
Zhongguancun Nanshanjie Street No. 6,  
Haidian District, Beijing, P.R.China  
Tel. 86-10-6804-6321  
Fax. 86-10-6804-6324

**JEOL (BEIJING) CO., LTD., SHANGHAI BRANCH**  
2F-3C Room, Building A, Mingji Business Plaza,  
No.207 Songhong Road, Changning District,  
Shanghai 200335, P.R.China  
Tel. 86-21-6249-4987  
Tel. 86-21-5836-6350  
Fax. 86-21-5836-3668

**JEOL (BEIJING) CO., LTD., GUANGZHOU BRANCH**  
Rm.3501, OnelinkCenter, 230 Tianhe Road, Tianhe District,  
Guangzhou, Guangdong Prov., 510620, China  
Tel. 86-20-8778-7849  
Fax. 86-20-8778-4268

**JEOL (BEIJING) CO., LTD., WUHAN BRANCH**  
Room A2118, Zhongshang Plaza Office Bldg.,  
No. 7 Zhongnan Road, Wuhan,  
Hubei, 430070, P.R.China  
Tel. 86-27-8713-2567  
Fax. 86-27-8713-2567

**JEOL LTD. (BEIJING) CO., LTD., CHENGDU BRANCH**  
1807A Zongfu Building,  
NO. 35 Zhongfu Road, Chengdu, Sichuan, 610016  
P.R. China  
Tel. 86-28-86622554  
Fax. 86-28-86622564

**EGYPT**  
JEOL SERVICE BUREAU  
3rd Fl. Nile Center Bldg., Nawal Street,  
Dokki, Cairo, Egypt  
Tel. 20-2-3335-7220  
Fax. 20-2-3338-4186

**FRANCE**  
JEOL (EUROPE) SAS  
Espace Claude Monet, 1 Allée de Giverny  
78290, Croissy-sur-Seine, France  
Tel. 33-1-9015-9737  
Fax. 33-1-9015-3747

**GERMANY**  
JEOL (GERMANY) GmbH  
Gute Aenger 30  
83306 Freising, Germany  
Tel. 49-8161-9845-0  
Fax. 49-8161-9845-100

**GREAT BRITAIN & IRELAND**  
JEOL (U.K.) LTD.  
JEOL House, Silver Court, Watchmead,  
Welwyn Garden City, Herts AL7 1LT, U.K.  
Tel. 44-1707-377117  
Fax. 44-1707-373254

**GREECE**  
N. ASTERIAS S.A.  
56-58 S. Tikoupi Str. P.O. Box 26140  
GR-1022, Athens, Greece  
Tel. 30-1-823-3383  
Fax. 30-1-823-9567

**HONG KONG**  
FARMING LTD.  
Unit No. 1009, 10/F, Prosperity  
683 King's Road, North Point, Hong Kong  
Tel. 852-2815-7239  
Fax. 852-2581-4635

**INDIA**  
JEOL INDIA PVT. LTD.  
Unit No.305, 3rd Floor,  
ABW Elegance Tower,  
Jasola District Centre,  
New Delhi 110 025, India  
Tel. 91-11-4595-8000  
Tel. 91-11-4595-8005  
Tel. 91-11-4595-8017

**JEOL INDIA PVT. LTD. Mumbai Office**  
214 E Square, Subhash Road,  
Vile Park (EAST),  
Mumbai 400 057, India  
Tel. 91-22-2612-9387

**JEOL INDIA PVT. LTD. Bangalore Office**  
125, Brigade Road,  
Unit No.402, Level 4, Palm Square,  
Bangalore-560025, India  
Tel. 91-80-4375-9351

**JEOL INDIA PVT. LTD. Kolkata Office**  
Regus, The Legacy, 25 / A,  
Shakaspore Sarani,  
Kolkata - 700017, India  
Tel. 91-98-3023-0484

**JEOL INDIA PVT. LTD. Hyderabad Office**  
422, Regus Solitaire Business centre,  
1-10-39 to 44, level 4, Gumidelli Towers, Old Airport Road,  
Begumpet, Hyderabad - 500016, India  
Tel. 91-40-6704-3708

**INDONESIA**  
PT. TEKNO LABINDO Penta Perkasa  
Komplek Gading Bukit Indah Blok I/11  
Jl. Bukit Gading Raya Kelapa Gading Permai,  
Jakarta 14240, Indonesia  
Tel. 62-21-46847057/58  
Fax. 62-21-45842729

**ITALY**  
JEOL (ITALIA) S.p.A.  
Palazzo Pechinotti - Milano 3 City,  
Via Ludovico Il Moro, 5/A  
20079 Basiglio(MI) Italy  
Tel. 39-02-9041431  
Fax. 39-02-90414343

**KOREA**  
JEOL KOREA LTD.  
Dongwoo Bldg. 7F, 1443, Yangjae Daero,  
Gangdong-gu, Seoul, 05355, Korea  
Tel. 82-2-511-8501  
Fax. 82-2-511-2635

**KUWAIT**  
Ashraf & CO., Ltd.  
P.O.Box 3555 Safat, 13036, Kuwait  
Tel. 965-2435151  
Fax. 965-2433373

**MALAYSIA**  
JEOL (MALAYSIA) SDN.BHD.  
508, Block A, Level 5,  
Kollans Business Center,  
97, Jalan SS 7/2, Kelana Jaya,  
47301 Petaling Jaya, Selangor, Malaysia  
Tel. 60-3-7492-7722  
Fax. 60-3-7492-7723

**MEXICO**  
JEOL DE MEXICO S.A. DE C.V.  
Arkasana 11 Piso 2  
Colonia Naples  
Delegacion Benito Juarez, C.P. 03810  
Mexico D.F., Mexico  
Tel. 52-5-55-211-4511  
Fax. 52-5-55-211-0720

**Middle East**  
JEOL GULF FZCO  
P.O. Box No. 971107  
Dubai Airport Free Trade Zone West Wing 5WA No, G12,  
Dubai, UAE  
Tel. 971-4-609-1497  
Fax. 971-4-609-1498

**PAKISTAN (Karachi)**  
ANALYTICAL MEASURING SYSTEM (PVT) LTD. (AMS LTD.)  
14-C Main Sehar Commercial Avenue Lane 4,  
Khayaban-e-Sehar,  
D.H.A.VIII, Karachi-75500, Pakistan  
Tel. 92-21-35345581/35340747  
Fax. 92-21-35345582

**PANAMA**  
PROMED S.A.  
Parque Industrial Costa del Este  
Urbanizacion Costa del Este  
Apartado 0316-01765, Panama, Panama  
Tel. 507-303-3100  
Fax. 507-303-3115

**PHILIPPINES**  
JATECO Philippines Corporation  
28 Floor, The Enterprise Center Tower 2,  
Ayala Avenue corner Paseo de Roxas,  
Brno, San Lorenzo, Makati City, 1226 Philippines  
Tel. (632) 849 3904

**PORTUGAL**  
Izasa Portugal Lda.,  
R. do Proletariado, 1  
2780-193 CARNAXIDE, Portugal  
Tel. 351-21-424-73-00  
Fax. 351-21-418-60-20

**QATAR**  
Marnal Trading Company W.L.L.  
AlI Ennadi Complex,  
Salwa Road P.O.Box 76, Doha, Qatar  
Tel. +974 4455-8216  
Fax. +974 4455-8214

**RUSSIA**  
JEOL (RUS) LLC  
Office 351, floor 3, 23,  
Novoslobodskaya St,  
Moscow 127059, Russia  
Tel. 7-495-748-7791/7792  
Fax. 7-495-748-7793

**SAUDI ARABIA**  
ABDULREHMAN ALGOSAIBI G.T.C. (Riyadh)  
Algosabi Building-Old Airport Road  
P.O. Box 213, Riyadh-11411, Saudi Arabia  
Tel. 966-1-477-7592

**SCANDINAVIA**  
SWEDEN  
JEOL (Nordic) AB  
Hammarbacken 6A, Box 716, 191 27 Sollentuna  
Sweden  
Tel. 46-8-298-2800  
Fax. 46-8-298-1647

**SINGAPORE**  
JEOL ASIA PTE.LTD.  
2 Corporation Road  
#01-12 Corporation Place  
Singapore 618494  
Tel. 65-6565-9369  
Fax. 65-6565-7552

**SOUTH AFRICA**  
AD Scientific (Pty) Ltd.  
370 Angus Crescent,  
Northlands Business Park, 29 Newmarket Road  
Northridge, Randburg, Republic of South Africa  
Tel. 27-11-462-1363  
Fax. 27-11-462-1466

**SPAIN**  
IZASA Scientific SLU.  
Argoneses, 13, 28108 Alcobendas,  
Madrid, Spain  
Tel. 34 902 20 30 80  
Fax. 49-8165-77246

**SWITZERLAND**  
JEOL (GERMANY) GmbH  
Gute Aenger 30  
83306 Freising, Germany  
Tel. 49-8165-77246  
Fax. 49-8165-77512

**TAIWAN**  
JIE DONG CO., LTD.  
7F, 112, Chung Hsiao East Road,  
Section 1, Taipei, Taiwan 10023 (R.O.C.)  
Tel. 886-2-2935-2978  
Fax. 886-2-2922-4665

For NMR & Mass Spectrometer Products:  
TechMax Technical Co., Ltd.  
5F, No.11, Wuqian 2nd Rd., Wugu Dist.,  
New Taipei City 248, Taiwan (R.O.C.)  
Tel. 886-2-8980-1779  
Fax. 886-2-8990-2559

For Semiconductor Products:  
JEOL TAIWAN SEMICONDUCTORS LTD.  
2F-2, No. 192, Dongguang Rd.  
East Dist., Hsinchu City 30069,  
Taiwan (R.O.C.)  
Tel. 886-3-571-5656  
Fax. 886-3-571-5151

**THAILAND**  
BECTHAI BANGKOK EQUIPMENT & CHEMICAL CO., Ltd.  
300 Phaholyothin Rd. Phayathai, Bangkok 10400,  
Thailand  
Tel. 66-2-615-2929  
Fax. 66-2-615-2350/2351

**JEOL ASEAN TECHNICAL CENTER (JATC)**  
MTEC building room 533  
114 Moo9, Thailand Science Park  
Paholyothin Rd., Klong 1, Klong Luang,  
Pathumthani 12120  
THAILAND  
Tel. 66-2-564-7738  
Fax. 66-2-564-7739

**THE NETHERLANDS**  
JEOL (EUROPE) B.V.  
Lureweg 4, NL-2153 PH Nieuw-Vennep,  
The Netherlands  
Tel. 31-252-623500  
Fax. 31-252-623501

**TURKEY**  
Tekser A.S.  
Kartal Cad. No: 55/3 Inonu Wah.,  
Atasehr 34755, Istanbul, Turkey  
Tel. 90-216-5733470  
Fax. 90-216-5736475

**USA**  
JEOL USA, INC.  
11 Dearborn Road, Peabody, MA 01960, U.S.A.  
Tel. 1-978-535-5900  
Fax. 1-978-536-2205/2206

**JEOL USA, INC. WEST OFFICE**  
5653 Stoneridge Drive Suite #110  
Pleasanton, CA 94588, U.S.A.  
Tel. 1-925-737-1740  
Fax. 1-925-737-1749

**VENEZUELA**  
GOMSA Service and Supply C.A.  
Urbanizacion Montalban III  
- Residencias Don Andres - Piso 7 - Apartamento 74  
Avenida 3, entre calles 7 y 8  
Montalban, Caracas, Venezuela  
Tel. 58-212-443-4342  
Fax. 58-212-443-4342

**VIETNAM**  
TECHNICAL MATERIALS AND RESOURCES  
IMPORT-EXPORT JOINT STOCK COMPANY (REXCO)  
Hanoi Branch  
SALES & SERVICE  
155-157 Lang Ha Street, Dong Da District, Hanoi, Vietnam  
Tel. +84 (43) 582 0516  
Fax. +84 (43) 853 2511